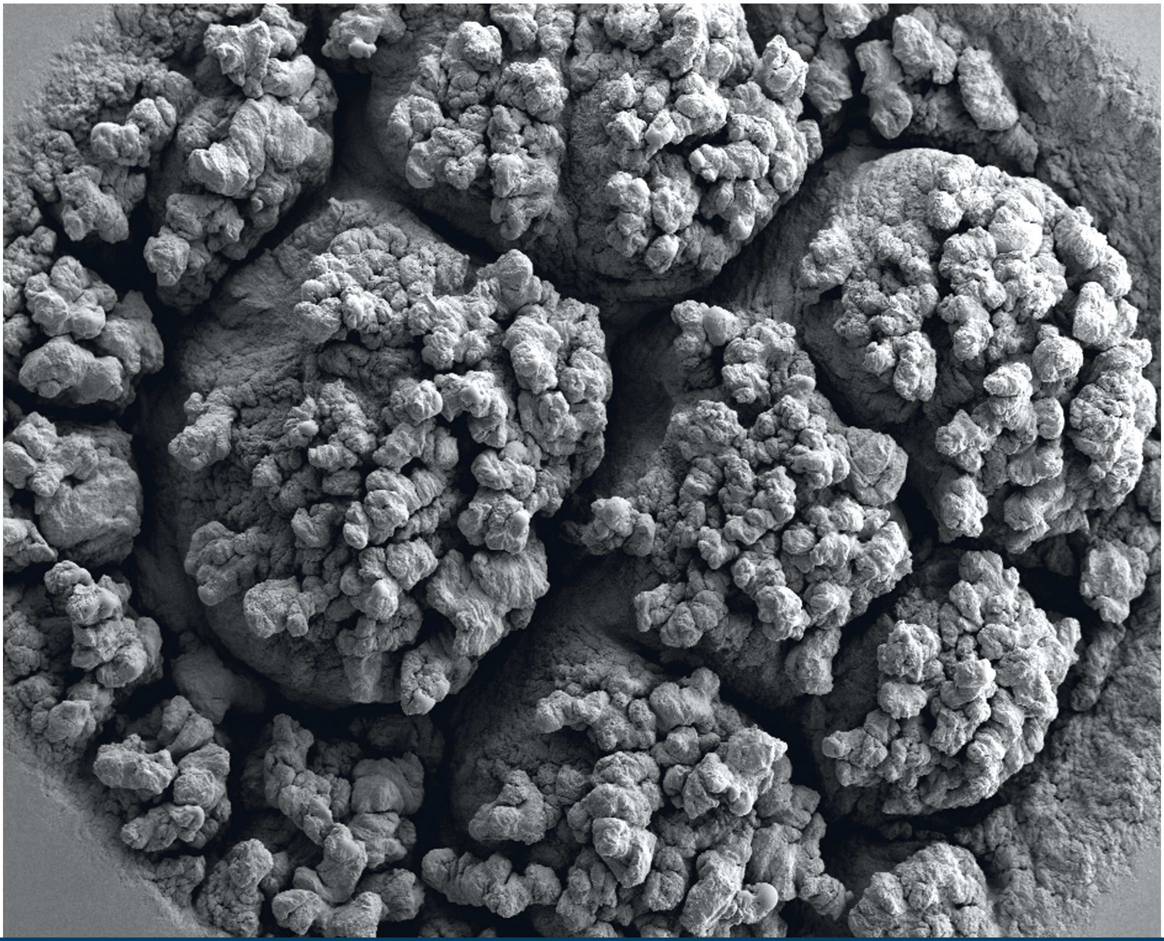

Behavior/performance of tungsten as a wall material for fusion reactors

Mauricio Gago

Energie & Umwelt / Energy & Environment
Band / Volume 612
ISBN 978-3-95806-707-3

Mitglied der Helmholtz-Gemeinschaft

JÜLICH
Forschungszentrum

Schriften des Forschungszentrums Jülich
Reihe Energie & Umwelt / Energy & Environment Band / Volume 612

Forschungszentrum Jülich GmbH
Institut für Energie- und Klimaforschung (IEK)
Plasmaphysik (IEK-4)

Behavior/performance of tungsten as a wall material for fusion reactors

Mauricio Gago

Schriften des Forschungszentrums Jülich
Reihe Energie & Umwelt / Energy & Environment Band / Volume 612

ISSN 1866-1793 ISBN 978-3-95806-707-3

Bibliografische Information der Deutschen Nationalbibliothek.
Die Deutsche Nationalbibliothek verzeichnet diese Publikation in der
Deutschen Nationalbibliografie; detaillierte Bibliografische Daten
sind im Internet über http://dnb.d-nb.de abrufbar.

Herausgeber und Vertrieb: Forschungszentrum Jülich GmbH
Zentralbibliothek, Verlag
52425 Jülich
Tel.: +49 2461 61-5368
Fax: +49 2461 61-6103
zb-publikation@fz-juelich.de
www.fz-juelich.de/zb

Umschlaggestaltung: Grafische Medien, Forschungszentrum Jülich GmbH

Druck: Grafische Medien, Forschungszentrum Jülich GmbH

Schriften des Forschungszentrums Jülich
Reihe Energie & Umwelt / Energy & Environment, Band / Volume 612

D 82 (Diss. RWTH Aachen University, 2023)

ISSN 1866-1793
ISBN 978-3-95806-707-3

List of symbols and abbreviations

Symbols

A	Projected area of contact	[m^{-2}]
c	Speed of light	[ms^{-1}]
d_0	Unstrained lattice spacing	[Å]
d_{hkl}	Lattice spacing	[Å]
E	Young's Modulus	[Pa]
E_{IT}	Indentation modulus	[Pa]
F_{HF}	Heat-flux factor	[MW^{-2}s^{½}]
H	Meyer hardness	[MPa]
hkl	Lattice orientation	[-]
I	Current	[A]
$\vec{L}$	Laboratory coordinates	[-]
L_0	Incident beam	[-]
L_{D}	Diffracted beam	[-]
m	Mass (atomic mass)	[kg (amu)]
P	Power	[W]
P	Applied load	[N]
P_{abs}	Absorbed power density	[Wm^{-2}]
Q	Energy gain factor	[-]
R_{a}	Arithmetic mean roughness	[µm]
$\vec{S}$	Surface coordinates	[-]
T	Temperature	[K or °C]
t	Time	[Wm^{-2}]
T_{e}	Electron energy	[eV]
T_{i}	Ion energy	[eV]
V	Voltage/potential	[V]
V_{p}	Variable potential	[V]
Z	Atomic number	[protons]
ΔT	Temperature change	[K or °C]
θ_{B}	Bragg angle	[°]
λ	Wavelength	[nm]

ν	Frequency	[Hz]
ν	Poisson's ratio	[-]
σ	Nuclear cross section	[barn]
σ	Stress	[Pa]

Abbreviations

BSE	Backscattered Electrons
CFC	Carbon-fiber Components
DBTT	Ductile-Brittle Transition Temperature
DEMO	DEMOnstration power plant
DIFFER	Dutch Institute for Fundamental Energy Research
dpa	Displacement per Atom
EBSD	Electron backscatter diffraction
EDM	Electric Discharge Machining
ELM	Edge Localized Mode
FGM	Functionally graded materials
FIB	Focused Ion Beam
ILW	ITER-like Wall
ITER	Latin for „the way“
IVT	Inner Vertical Target
JET	Joint European Torus
JUDITH	Jülicher Divertor Facility in Hot Cells
LM	Light Microscopy
LOCA	Loss of coolant accident
MHD	Magnetohydrodynamics
MHD	Magnetohydrodynamics
NRA	Nuclear Reaction Analysis
OECD	Organization for Economic Cooperation and Development
OVT	Outer Vertical Target
PFC	Plasma Facing Component
PFM	Plasma Facing Material
PFU	Plasma Facing Unit
PSI	Plasma-surface Interaction

RT	Room Temperature
SE	Secondary Electrons
SEM	Scanning Electron Microscopy
SOL	Scrape-Off Layer
SOL	Scrape-off Layer
Tokamak	Toroidal chamber with magnetic coils
VDE	Vertical Displacement Event
XRD	X-ray Diffraction

List of Publications

Part of the results presented in this work have been published in the following articles:

M. Gago, A. Kreter, B. Unterberg, M. Wirtz, Synergistic and separate effects of plasma and transient heat loads on the microstructure and physical properties of ITER-grade tungsten, *Phys. Scr.* **96** (2021) 124052. https://doi.org/10.1088/1402-4896/ac326c

M. Gago, A. Kreter, B. Unterberg, M. Wirtz, Synergistic effects of particle and transient heat loads on ITER-grade tungsten, *Phys. Scr.* **T171** (2020) 14007. https://doi.org/10.1088/1402-4896/ab3bd9.

A. Terra, G. Sergienko, M. Tokar, D. Borodin, T. Dittmar, A. Huber, A. Kreter, Y. Martynova, S. Möller, M. Rasiński, M. Wirtz, T. Loewenhoff, D. Dorow-Gerspach, Y. Yuan, S. Brezinsek, B. Unterberg, C. Linsmeier, Micro-structured tungsten: an advanced plasma-facing material, *Nuclear Materials and Energy* **19** (2019) 7–12. https://doi.org/10.1016/j.nme.2019.02.007.

Kurzfassung

Kernfusion ist die häufigste Energiequelle im Universum. Im Inneren der Sterne werden durch Kernfusion Wärme und Licht freigesetzt. Seit den 1940er Jahren arbeitet man daran, die Kraft der Fusionsenergie nutzbar zu machen, doch ist dies noch nicht auf kommerziell vertretbare Weise gelungen. Der bisher größte Kernfusionsreaktor wird derzeit in Frankreich gebaut und soll 2025 sein erstes Plasma erzeugen. ITER (lateinisch "der Weg") soll der erste Fusionsreaktor der Welt sein, der mehr Energie freisetzt als er zur Plasmaheizung benötigt, und er soll – daher der Name – den Weg zur kommerziellen Nutzung der Fusionsenergie ebnen.

Eine der größten Herausforderungen für ITER wird die Abfuhr der freigesetzten Leistung sein. Der Divertor in ITER wird der Bereich sein, der im Reaktor den höchsten Belastungen ausgesetzt ist. Wolfram wurde aufgrund seiner thermischen und mechanischen Eigenschaften, wie hoher Schmelzpunkt, hohe Wärmeleitfähigkeit und niedrige Erosionsrate, als geeignetster Kandidat für das Plasma-Wand-Material (PFM) im Divertor ausgewählt.

Die vorliegende Arbeit konzentriert sich auf die Analyse des Verhaltens von Wolfram unter ITER-relevanten stationären Plasma- und transienten Wärmebelastungen, um die Auswirkungen der Bedingungen im ITER-Divertor auf das PFM zu erfassen. Zu diesem Zweck wurden Wolframproben in der linearen Plasmaanlage PSI-2 getestet. Es wurden zwei Arten von Proben verwendet, eine mit nadelartigen Körnern senkrecht zur Probenoberfläche (transversale Proben), was die bevorzugte Mikrostruktur für den ITER-Divertor ist, die andere mit größeren, isotropen Körnern, die man durch Rekristallisation transversaler Proben erhält (durch Wärmebehandlung bei 1600 °C für eine Stunde, rekristallisierte Proben). Die Proben wurden jeder Art von Belastung einzeln, nacheinander, sowie gleichzeitig ausgesetzt, um die Auswirkungen sowohl unabhängig voneinander als auch in möglicher Synergie zu untersuchen.

Bei der Beaufschlagung der Proben mit Plasmalasten wurde die Bildung von Nanostrukturen auf der Oberfläche, dem so genannten „fuzz“ (engl. Flaum, Fussel), beobachtet, ohne dass es Anzeichen für eine weitere Oberflächenveränderung oder -schädigung gab. Der Einfluss der transienten Wärmebelastung wurde danach untersucht und es konnte gezeigt werden, dass die durch die Laserpulse verursachte ermüdende mechanische Wechselspannung einen größeren Einfluss auf die beobachteten Schäden hat als die Plasmapartikel. 10^5 Laserpulse mit 0,2 $\mathrm{GWm^{-2}}$ verursachten keine erkennbare Rissbildung in transversalen Proben und nur sehr geringe Rissbildung in rekristallisierten Proben. Bei dieser Leistungsdichte bildeten

sich vollständige Rissnetzwerke erst nach 10^6 Pulsen aus, während dies bei 0,4 und 0,8 GWm^{-2} bereits nach 10^5 Pulsen zu beobachten ist.

Anschließend wurde der Einfluss der gleichzeitigen Einwirkung beider Belastungen untersucht. In allen Fällen wurde die beobachtete Rissbildung durch die Synergie der Belastungen verstärkt, was durch Wasserstoffversprödung und die Bildung von Heliumblasen erklärt werden kann.

Die Bildung von Heliumblasen im Material kann für das Materialverhalten der PFM von besonderer Bedeutung sein. Pulse von 0,8 GWm^{-2}, so wie die Erhöhung der Plasmafluenz beschleunigten das Wachstum oberflächennaher Blasen erheblich. Bei der Untersuchung der Härte des Materials mittels Nanoindentierung zeigte sich in dem Bereich des Materials, der beiden Belastungsarten ausgesetzt war, eine Zunahme der Härte. Dieser Effekt nahm mit der Tiefe ab und wurde in Bereichen, die ausschließlich der Plasmabelastung ausgesetzt wurden, nicht beobachtet.

Bei der Analyse der Eigenspannungen der Proben mit Hilfe der $\sin^2\Psi$-Methode wurde festgestellt, dass die transversalen Proben im Neuzustand erhebliche Druckspannungen in der Oberfläche aufwiesen. Dies erklärt die höhere Schadensschwelle, die das transversale Material im Vergleich zu rekristallisierten Proben aufweist. Eigenspannungen wurden nach der Einwirkung von Wärme- und Plasmabelastungen abgebaut.

Diese Tests haben gezeigt, dass trotz der Bevorzugung einer transversalen Mikrostruktur für die Wolfram-PFM im Divertor kein signifikanter Unterschied im Materialverhalten bei höheren Belastungen besteht. In Bereichen des Divertors, in denen die Belastungen gering sind, bleibt die transversale Mikrostruktur erhalten. Wo jedoch die höchsten Belastungen zu erwarten sind, könnte sich die ursprüngliche Mikrostruktur als irrelevant erweisen, da eine weitgehende Rekristallisation zu erwarten ist.

Die in dieser Arbeit vorgestellten Ergebnisse haben bestätigt, wie wichtig die Kontrolle (Verringerung der Intensität oder Unterdrückung) von transienten Wärmelasten in Bezug auf die Lebensdauer der Reaktorwand ist. Die hier untersuchten Pulszahlen sind geringer als die Anzahl, die während der Lebensdauer von ITER erwartet wird, und dennoch wurde bereits eine weit verbreitete Rissbildung beobachtet. Dies stellt an sich noch kein Problem für den Betrieb dar, kann aber zu anderen Problemen führen, z. B. zu einer verstärkten Erosion von Wolfram. Risse senkrecht zum Wärmefluss wirken zudem als thermische Barrieren für die Wärmeableitung, so dass höhere Temperaturen an der Oberfläche die Materialschäden verschlimmern und schließlich zu einem katastrophalen Versagen des Materials führen können.

Abstract

Nuclear fusion is the most common source of energy in the universe. Heat and light are generated inside stars through nuclear fusion. Since the 1940s, many attempts have been made to harness the power of fusion energy, but this has not yet been achieved in a commercially viable manner. The largest-ever nuclear fusion reactor is now being built in Cadarache, southern France, and it is expected to achieve its first plasma in 2025. ITER, or "*the way*" in Latin, is expected to be the first fusion reactor in the world to produce more energy than it consumes, and it will, as its name suggests, pave the way towards commercial fusion energy in the future.

One of the main issues expected in ITER is that of power exhaust. Enormous quantities of energy will be produced which need to be extracted. The divertor region in ITER will be mostly responsible for this task and will, thus, be the region exposed to the highest loads in the reactor. Due to its favorable thermal and mechanical properties, such as a high melting point, high thermal conductivity and low erosion rate, tungsten has been chosen as the best candidate for plasma facing material (PFM) in the ITER divertor. This work focuses on the analysis of the behavior of tungsten under ITER-relevant steady plasma and transient heat loads in order to understand and predict the effects the conditions in the ITER divertor will have on the PFMs. To achieve this, the tungsten samples were tested in the linear plasma device PSI-2. Two kinds of samples were utilized, one with needle-like grains transversal to the sample surface, which is the preferred microstructure for the ITER divertor, the other with larger, isotropic grains obtained after recrystallization of transversal samples at 1600 °C for 1 h. Moreover, samples were first exposed to each kind of load separately to study the effects independently of each other. Samples were then exposed to both loads simultaneously to analyze the possible synergistic effects of such loads.

By exposing the samples to plasma loads the formation of nanotendrils on the surface, what is known as tungsten fuzz, was observed, without any indication of further surface modification or damage. The influence of only the transient heat loads was then investigated. It was observed that the fatigue stress caused by the laser pulses has a larger effect on the damage observed than the plasma particles. 10^5 laser pulses of 0.2 GWm^{-2} caused no observable cracking in transversal samples, and very slight cracking in recrystallized ones. At this power density, crack networks formed only after applying 10^6 pulses to the samples. With higher P_{abs}, of 0.4 and 0.8 GWm^{-2}, a crack network already starts forming after exposure to 10^5 pulses.

Once the effects of the separate loads were determined, the influence of the simultaneous exposure to both loads was investigated. In all cases, the cracking observed was exacerbated by the synergy between both loads. Hydrogen

embrittlement and the formation of helium bubbles deteriorate the material properties, which cause the increased cracking and plastic deformation of the material.

The formation of bubbles in the material can be of particular importance for the material behavior in PFMs. It was observed that applying pulses of 0.8 GWm^{-2} substantially accelerates the growth of helium bubbles near the surface of the material. A further increase in bubble size was observed by increasing the plasma fluence applied. Additionally, the hardness of the material was analyzed via nanoindentation. An increase in hardness was observed in the area of the material affected by both kinds of loads. This effect decreases with depth and is not observed in areas affected only by plasma.

Furthermore, by analyzing the residual stresses of the samples via the $\sin^2\Psi$ it was observed that as-received transversal samples have significant compressive stresses in the surface. This explains the higher damage threshold displayed by the transversal material compared to recrystallized samples. Residual stresses are relaxed after exposure to heat and plasma loads.

These tests have revealed that despite a transversal microstructure is preferred for the tungsten PFMs in the ITER divertor, there is no significant difference in the material behavior at higher loads. This suggests that in areas of the ITER divertor where loads are lower, the transversal microstructure might be conserved and have superior performance to other microstructures. However, where the highest loads are expected, such as at the strike points, the initial microstructure might prove to be irrelevant, as widespread recrystallization should be expected.

The results presented in this work have, furthermore, corroborated how vital ELM mitigation and control is for the success of ITER. A much lower number of ELM-like events was tested than what is expected in the lifetime of ITER, and widespread cracking was already observed. Cracking is not, in and of itself an issue for the functioning of ITER, but it might lead to other problems, such as the increased erosion of tungsten, which would, in turn, cause a cool down of the plasma. It also creates thermal barriers for heat dissipation, which might lead to local high temperature areas, which can exacerbate the material damage, eventually leading to a catastrophic failure of the material.

Contents

1. Introduction

Since the industrial revolution, there has been a steady increase in the world's energy demand. With the current population growth and the industrialization of developing countries, this trend is expected to continue. Total energy consumption is expected to grow by 28% from 2015 to 2040; however, the energy consumption of OECD (Organization for Economic Cooperation and Development) countries will only grow 9%, in contrast with a growth of 41% for non-OECD countries. [1] And despite fossil fuels and current renewable energy technologies being able to cover this demand in the short term; fossil fuel reserves are dwindling, and public concern for climate change, pollution, and accidents at nuclear fission power plants present a serious challenge for the long-term energy supply.

Nuclear fusion presents itself as the ultimate source of sustainable and dependable energy. It is the most common source of energy in the universe, being what powers our Sun and all other stars in the firmament. Nonetheless, conditions on Earth are not those inside stars, no commercial fusion reactors have been built yet, and the plans to build one are still decades in the future.

There are, however, several experimental reactors worldwide. The largest and most ambitious one of all is ITER, which is being built in Cadarache, southern France (Figure 1.1). ITER is an international collaboration which aims to be the first reactor to "break even" – that is, to release more energy than is needed to maintain the fusion reaction going. It will test several different concepts and technologies which could be later applied to a commercial reactor.

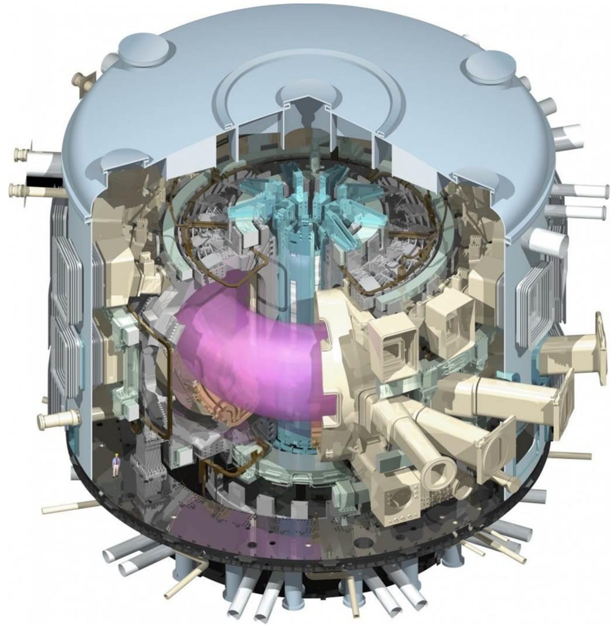

Figure 1.1: ITER, the world's largest fusion reactor, currently being built in Cadarache, southern France [2].

Inside the vacuum chamber in ITER, materials will have to withstand extreme conditions. Tungsten, being one of the chosen materials to be used as a plasma-facing material in the divertor, the component exposed to the highest loads, is of the utmost importance. This work seeks to broaden the available knowledge about tungsten and its behavior under fusion relevant loads, in order to have a clear picture of how the material will behave and how much damage is to be expected once ITER starts its operation. It will show how these loads affect the physical properties and microstructure of tungsten, and how changing the conditions impact the effects observed.

2. Literature review

2.1. Nuclear fusion

The idea that energy could be released by fusing two atomic nuclei started with Arthur Eddington in the 1920s, when he proposed a possible explanation of how the Sun produces its energy. He based his theory on Albert Einstein's famous deduction that mass could be transformed into energy ($E = mc^2$), and Francis Aston's weighing of atomic masses, in which he showed how four hydrogen atoms weigh slightly more than a helium atom. This was debated at first, as classical physics did not consider the temperature of the Sun to be high enough to break the potential barrier and to allow the hydrogen atoms to fuse [3].

The most basic nuclear fusion reaction, that of two hydrogen atoms joining together to form a deuteron, a positron (e^+) and an electron-neutrino (ν_e):

$$2\,{}^{1}_{1}\mathrm{H} \rightarrow {}^{2}_{1}\mathrm{H} + e^{+} + \nu_{e} + 1.44\ \mathrm{MeV} \qquad (1.1)$$

requires 600 keV to take place according to classical physics. The Sun, having a temperature in its core of about 15.5 million Kelvin, or 1.335 keV, would not have enough energy for the reaction to occur. This problem was solved years later by Friedrich Hund and George Gamow with the advent of quantum mechanics and the theory of quantum tunneling, which allowed the fusion of atoms at much lower temperatures than with classical physics. Quantum theory states that subatomic particles act like spread-out waves with no defined position. This was first used by Gamow to explain how subatomic particles can escape the nucleus, but it can also explain how they can fuse together at much lower kinetic energies than classical physics suggests. The same can be used to explain the opposite case. At high enough kinetic energies, part of the probability wave of particles can be located on the opposite side of the potential barrier, allowing them to "tunnel" through and fuse together [4,5].

With the discovery of deuterium (D), neutrons, helium-3 and then tritium (T) in the early 30s, the way was set for the science of nuclear fusion. Shortly thereafter, in 1932, the first fusion reactions between light nuclei were performed by Mark Oliphant by bombarding deuterium with deuterium [6].

As mass spectroscopy advanced and became more accurate, it was found that many isotopes of elements were lighter than the simple addition of the masses of their individual components. This means that when protons and neutrons are put together in a nucleus, they lose mass. A similar effect had been observed at the turn of the 20th century by Marie and Pierre Curie. They observed that with time, radium breaks up into radon and helium, releasing energy in the process. If the masses of radon and helium are added, they account for only 99.997 percent of the mass of radium, losing 0.003 percent of mass. This reduction in mass is known as the mass defect, which when inserted in Einstein's equation shown above, can be used to obtain the binding energy of the subatomic particles in the nucleus (or nucleons) [6,7].

A larger mass defect per nucleon, thus, means that the nucleus is more stable. By measuring the mass defect of all elements and their isotopes, it was found that the most stable elements are iron and nickel, as can be seen in Figure 2.1. Elements to the left of Fe and Ni will release energy by fusing together (nuclear fusion) with other atoms, while elements to the right will release energy by breaking up into smaller elements (nuclear fission).

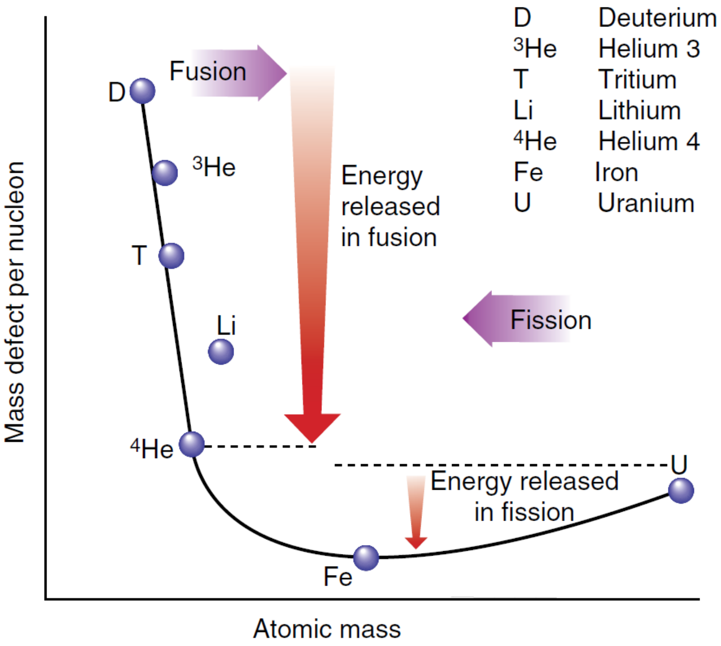

Figure 2.1: Energy released by fusion or fission reactions, expressed as the mass defect per nucleon [3].

By bombardment of uranium with neutrons to try and obtain heavier elements than uranium (the heaviest naturally occurring element on Earth), Otto Hahn and Fritz Strassman actually split the atoms, obtaining isotopes of lanthanum and barium. This led to the invention of the first atomic fission reactor by Enrico Fermi in 1943. Nuclear fusion turned out to be much more complicated.

2.1.1. Nuclear fusion in the stars

As mentioned above, Arthur Eddington deduced that the Sun and other stars generate their energy by nuclear fusion. He took the 0.7 % mass defect of helium atoms when compared to hydrogen atoms, or protons (p) and proposed the reaction:

$$4\mathrm{p} \rightarrow {}^{4}\mathrm{He} + 26.1\ \mathrm{MeV} \qquad (1.2)$$

as the main source of energy in the stars. This even allowed him to calculate the Sun would have enough hydrogen to last for about 15 billion years.

As a side note, before Eddington's calculations, the proposed source of the Sun's energy was the energy released by gravity's force pushing material into its center. Lord Kelvin calculated this would produce enough energy for the Sun to only last a few million years. Lord Kelvin was opposed to Darwin's theory of evolution, because this didn't provide enough time for species to evolve. Darwin was forced to admit that he had no explanation for this and would have to leave this enigma for future scientists to solve. And so it was [7].

Robert Arkinson and Fritz Houtermans in 1929 applied the theory of quantum tunneling to the fusion process in the Sun. They demonstrated that even at the high temperatures inside the Sun, only light nuclei at the high-speed tail of the Maxwellian speed distribution had enough energy to penetrate nuclei. This allowed them to explain the slow speed at which nuclear reactions take place in stars and how the rate of fusion reactions in a star's core rapidly increases with increasing temperature. This also allowed Atkinson to prove that the most frequent reaction inside the Sun was actually that of two protons fusing to form a deuteron, a positron and an electron neutrino (1.1) [5].

Finally, Hans Bethe, along other scientists, extended this reaction to obtain what he called the proton-proton chain (Figure 2.2). It starts with the collision of two protons with high kinetic energy. They fuse together to form a deuteron, releasing a positron and an electron neutrino. This is the speed defining step, as only one out of every 10^{25} proton collisions in the Sun's core allows protons to fuse together. The deuteron then quickly collides with another proton, forming a helium-3 (or tritium) ion and releasing gamma radiation. Two of these helium-3 ions can then react together for the final step of this chain, forming a helium-4 ion and releasing two protons. The total energy released by the proton-proton chain is 26.73 MeV.

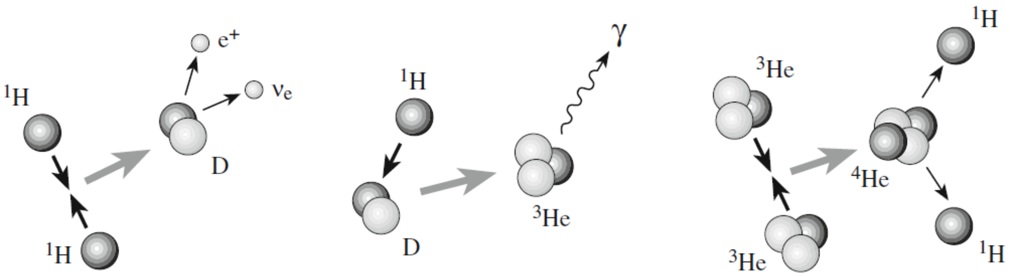

Figure 2.2: Proton-proton chain: Two protons fuse together to form a deuteron, releasing a positron and an electron neutrino. The deuteron then fuses with another proton, forming ^{3}He and releasing gamma radiation. Finally, two ^{3}He ions collide to form a ^{4}He ion and releasing two protons [5].

2.1.2. Nuclear fusion on Earth

As mentioned above, the first step in the proton-proton chain is a slow process. This is in particular due to the fact that one of the protons must be transformed into a neutron. No such transformation is required in the following steps, making them much faster. And since about 0.01% of all hydrogen on Earth is deuterium, this first step can be skipped. Even such small percentage of deuterium would be enough to power nuclear fusion reactions for many millions of years at current energy consumption rates.

The probability of a fusion reaction happening at certain temperature is measured in the cross section (σ). The cross section is, basically, the probability of two particles of colliding with each other with enough energy to react. As seen in Figure 2.3, the cross section for the fusion of two deuterons is several orders of magnitude smaller than for the D-T reaction at temperatures lower than about 1000 keV, or $12 \cdot 10^9$ K. This means that the easier and most efficient fusion reaction to achieve is between deuterium and tritium nuclei [3]:

$$D + T \rightarrow {}^4\text{He} + p + 17.6\ \text{MeV} \qquad (1.3)$$

Using tritium brings other challenges. Tritium is a radioactive isotope of hydrogen with a half-life of 12.3 years, making it incredibly rare on Earth. Tritium is produced in small quantities in some fission reactors, but this would not be enough to power fusion reactors, so another source of tritium is required. To solve this problem, tritium can be bred in fusion reactors, using lithium and the neutrons released by fusion reactions themselves. This is the basis of lithium breeding blankets. When a neutron with enough energy hits a lithium nucleus, tritium can be formed by the following reactions:

$$ {}^{6}\mathrm{Li} + n \rightarrow {}^{4}\mathrm{He} + T + 4.8\ \mathrm{MeV} \tag{1.4} $$

$$ {}^{7}\mathrm{Li} + n \rightarrow {}^{4}\mathrm{He} + T + n - 2.5\ \mathrm{MeV} \tag{1.5} $$

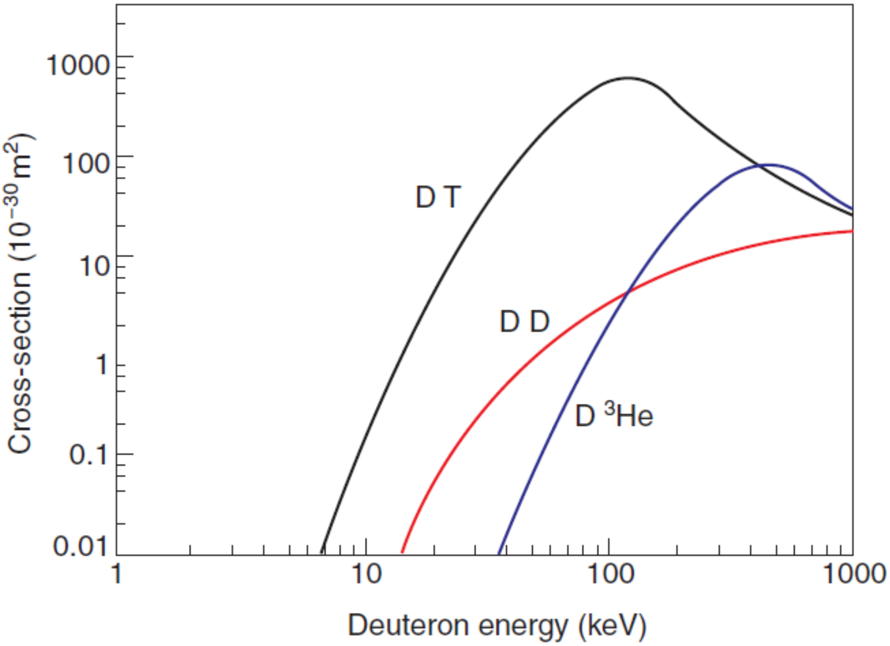

Figure 2.3. Reaction probability (expressed in the cross section of the reaction) for D-D, D-T and D-^{3}He reactions depending on deuteron energy [3].

Since the 1940s, many attempts have been made to harness the power of nuclear energy. Achieving nuclear fusion is not a problem, but for a reactor to be commercially viable, it has to produce more energy than it consumes. The way in which this is measured is with the fusion energy gain factor (Q):

$$ Q = \frac{P_{fus}}{P_{in}} $$

where P_{in} is the power used to heat the plasma, and P_{fus} is the power obtained by fusion reactions. The point where both are equal and $Q = 1$ is called breakeven. For a commercially viable fusion reactor the value of Q should in fact be greater than 1 to cover the energy needed for all the different systems used to run the reactor, and it must be many times greater than 1 to cover the actual costs of building and running the reactor [3,4].

As it turns out, developing a nuclear reactor on Earth, in particular one which can achieve breakeven, has one major difficulty, confinement. For fusion reactions to start, the fuel has to be heated to extremely high temperatures, in the range of millions of Kelvin. In fact, to produce fusion energy efficiently, plasma should be in the hundreds of millions of degrees range, an order of magnitude higher than in the core of the Sun. As temperature is increased, it causes particles to collide with higher kinetic energy, which causes the plasma to expand. As it expands, it also cools down, and eventually there is not enough energy for fusion reactions to take place anymore. In the Sun's core, plasma is compressed by its gravity and particles cannot escape, so temperature and density remain high. This is evidently not the case on Earth, and an alternative solution must be found. The obvious solution would be to find a material that can sustain such energies, but at the high temperatures needed, all matter is found in its plasma state. There is no material that is even close to being able to withstand this [3].

Several concepts to solve the issue of confinement have been conceptualized. The first, and most relevant for this work, is magnetic confinement, where magnetic fields are used to keep the plasma inside a vacuum vessel and preventing it from coming into contact with the vessel walls. The second concept being that of inertial confinement. This method consists of laser heating a fuel pellet so quickly that it achieves fusion temperatures before expanding. Inertial confinement fusion is, however, outside the scope of this work.

2.2. Magnetic confinement

One of the earliest attempts was made by George Thonemann in Oxford. He utilized what is called the *pinch effect*. A plasma is composed of ionized particles, which means that applying a current through the plasma causes a magnetic field around the direction of the current. This caused the plasma to be compressed, increasing its density and temperature. Fusion was finally achieved using this method with the Scylla device in the United Kingdom in 1958. The method had, however, severe problems with instabilities. A current flowing through a plasma creates a magnetic field, which in turn generates another electrical current, so on and so forth. This makes plasmas very hard to predict and to control, and it gave birth to the study of magnetohydrodynamics (MHD). These instabilities made the plasma get out of control after only fractions of a second and hit the walls of the device.

Almost in parallel with these attempts, in the Soviet Union in 1951, Andrei Sakharov and Igor Tamm designed what is now known as the *tokamak*. The word tokamak comes from the Russian "toroidalnaya kamera ee magnitaya katushka", or toroidal chamber with magnetic coils.

The principle of the tokamak is combining two magnetic fields (Figure 2.4, left). The first one, which resembles the one present in a pinch machine, is the magnetic field caused by an electrical current flowing through the plasma, which is generated by a transformer action. The second, and strongest, magnetic field is generated by coils placed around the torus. This field is several times stronger than the one generated by the pinch effect, and aids greatly in stabilizing the plasma [3].

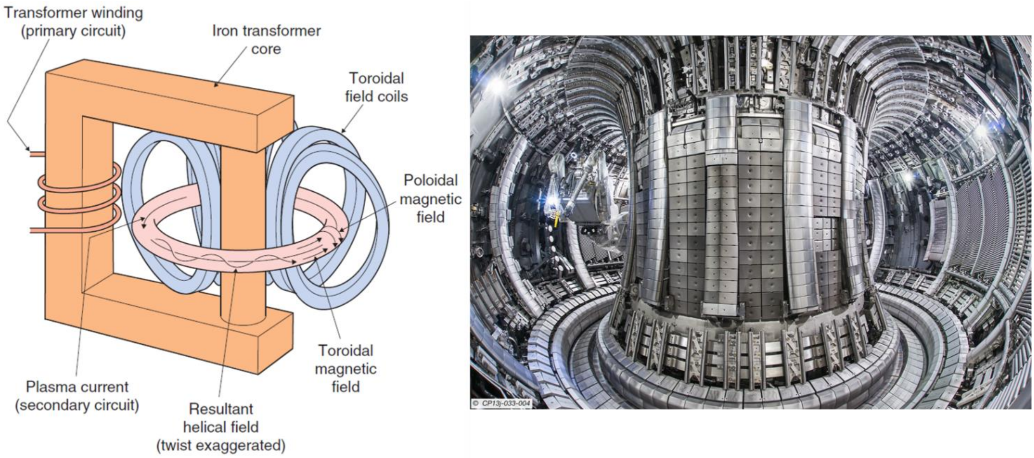

Figure 2.4. Left: schematic view of a tokamak, with its central solenoid which generates the electrical current in the plasma, and its toroidal magnetic field coils, which aid in stabilizing the plasma. Also shown is the helical field produced by the combination of the magnetic fields [3]. Right: View inside the JET tokamak in Culham, UK, with its ITER-like walls [8].

Since the late 1960s, tokamaks have been the most advanced fusion devices, due to their relative stability and success compared to other methods. The largest tokamak that has been built is the Joint European Torus (JET), in Culham, United Kingdom, Figure 2.4, right. Modern tokamaks such as JET have additional poloidal field coils, which help stabilize the plasma vertically [9]. A similar concept has also steadily been developed, the stellarator. Stellarators possess toroidal magnets designed in a non-axisymmetric geometry so that the plasma plasma is stabilized in a current free and can, therefore, operate in a steady state [10]. This concept, in fact, predates the tokamak, but due to their complex geometry and fabrication, development of stellarators has advanced at a slower pace and more research has been done toward tokamaks. The largest stellarator, Wendelstein 7-X, was built in Greifswald, Germany, and can be seen both as a schematic and from the inside in Figure 2.5.

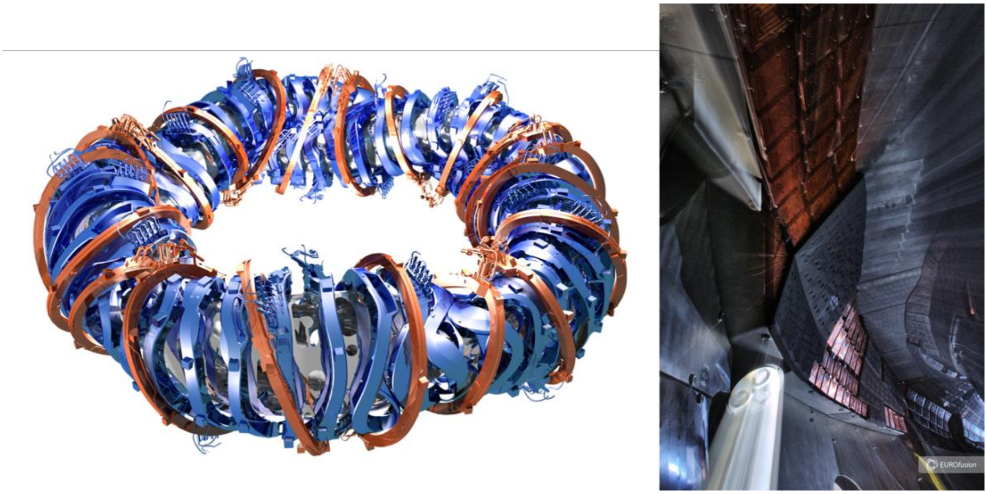

Figure 2.5. Left: schematic view of the Wendelstein 7-X stellarator with its twisting geometry and magnetic coils surrounding the vacuum vessel [11]. Right: View inside the Wendelstein 7-X stellarator [8].

Other magnetic confinement configurations have been tried, such as the magnetic mirror. This is cylindrical device with a linear magnetic field, and a stronger magnetic field in both ends, creating a *magnetic mirror effect*. This solution to the confinement problem was discarded due to the high amount of fuel loss despite the magnetic mirrors. These devices are, however, still used as fusion neutron sources [4,6].

To this day, no fusion device has achieved breakeven. The closest attempt to achieve was performed in 1997 with JET, which is also the only functioning reactor capable of DT reactions. JET achieved a record transient Q of 0.62, producing 18 MW of fusion power. It also produced a steady state fusion power of 4 MW during 4 s, with a Q of 0.18. As evidenced by these values, JET is still far away from breakeven. A new DT campaign is planned for 2020, but still, the stability of the plasma is in big part dependent on size, and larger tokamaks are needed [12].

2.3. ITER

As tokamaks get larger, they get invariably more expensive. But as seen above, their performance is in large part dependent on size. Thus, in order to be able to design, build and operate a tokamak large enough to break even, several countries had to join in one of the most expensive and ambitious scientific projects in human history. In 2010, and after two decades of negotiating and planning, construction of ITER ("the way" in Latin) started in Cadarache, France. ITER is being built and financed by 35 countries, China, the European Union (including Switzerland), India, Japan, South Korea, Russia and the United States. In order for ITER to be able to achieve its objectives, it will be several times larger than JET, and is expected to be able to generate 500 MW of power with a Q of 10. A comparison between both devices can be seen in Table 2.1. Of particular interest is that ITER will use superconducting magnets, which produce more powerful magnetic fields and require less energy. This adds a layer of complication, which is that they must be cooled to about 4 K with liquid helium [13].

Table 2.1. Comparison between size and capabilities of JET and ITER [2,8,12,13].

	JET	*ITER*
Q	0.62 (actual)	10 (expected)
P_{fus}	16	500
Plasma volume (m^3)	150	840
Magnetic coils	Conventional (Cu)	Superconducting (Nb_3Sn and Nb-Ti)
Toroidal magnetic field (T)	4	12
Plasma current (MA)	4.8	15

ITER is expected to prove that fusion is a viable alternative to produce clean and virtually inexhaustible energy, and that is not dependent on weather or any other factors. It will also be used as an experimental reactor to test designs, plasma conditions, diagnostics and materials. ITER itself will be an experimental reactor and is not designed to generate electric power for commercial use. The information obtained, however, will be vital in the pathway to commercial fusion power. Several countries have plans to build their own test reactor in the decades following ITER's start of operation (2030s). This test reactor, branded DEMO, will improve on the design of ITER, and is expected to be the last steppingstone before a commercial reactor is built. One of the main challenges in achieving this is the exhaust of fusion "ashes", in this case, helium [14].

As fusion occurs, deuterium and tritium react with each other to produce helium and a neutron. Neutrons cannot be contained by magnetics fields as they have no charge and will impact the vacuum vessel’s walls randomly. Helium will remain confined, and if more fuel is injected into the reactor, eventually the particle density will be too high, and confinement will be compromised. To prevent this, helium and other impurities that might be present need to be eliminated.

The outer plasma layer, called scrape-off layer (SOL) is deflected so that impurities collide against the divertor, which is especially designed to sustain higher loads than the rest of the inner walls of the vacuum vessel (Figure 2.6). Once the particles collide, they get neutralized and can be extracted by vacuum pumps. In colliding against the divertor, particles transfer large amounts of energy, which can cause melting, erosion, displacements, and other kinds of damage. It is, therefore, important to study the effects that these loads will have on the plasma facing components (PFCs) in ITER. In this way, issues that might arise once ITER is functioning at full power can be foreseen and, hopefully, prevented.

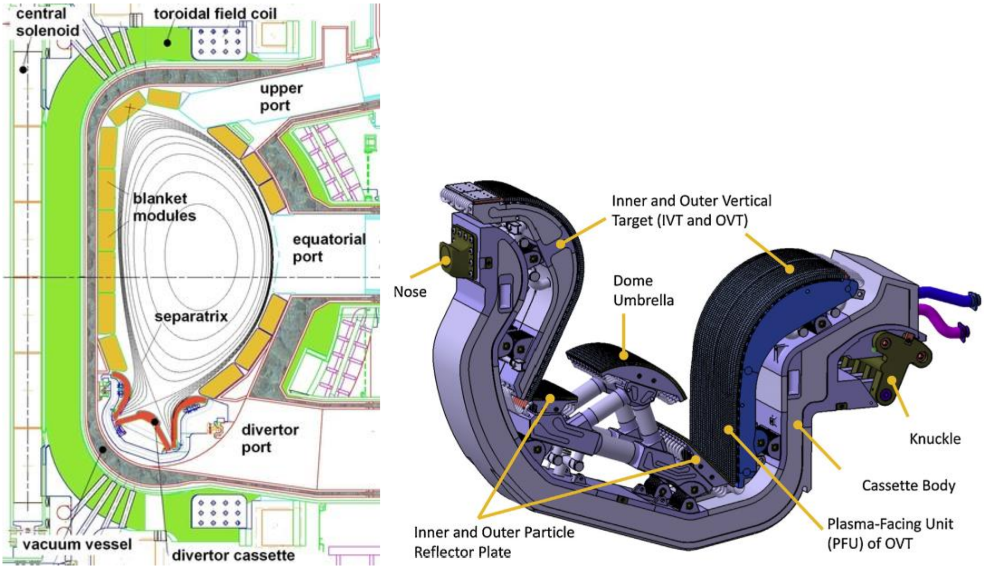

Figure 2.6. Left: Schematic of the cross section of ITER. Of particular interest are the magnetic field lines inside the vacuum vessel. Those inside the separatrix will confine the plasma particles, those outside it will cause the plasma particles to collide against the divertor, which can be seen at the bottom of the schematics [15]. Right: Schematic of a divertor cassette for use in ITER. The inner and outer vertical targets (IVT and OVT) will sustain the highest loads [16].

The divertor in ITER will be composed of 54 cassettes (a divertor cassette is shown in Figure 2.6, left and in Figure 2.7, right), each one weighing around 9 tons. The cassettes can be replaced by remote handling, to reduce the exposure of workers to activated materials. The vertical targets, being the components most exposed to plasma loads, feature a monoblock design (shown in Figure 2.7), with a CuCrZr tube for water cooling. The dome has a flat-tile design with a hypervapotron cooling system, as it is not expected for it to undergo such high loads [17–19].

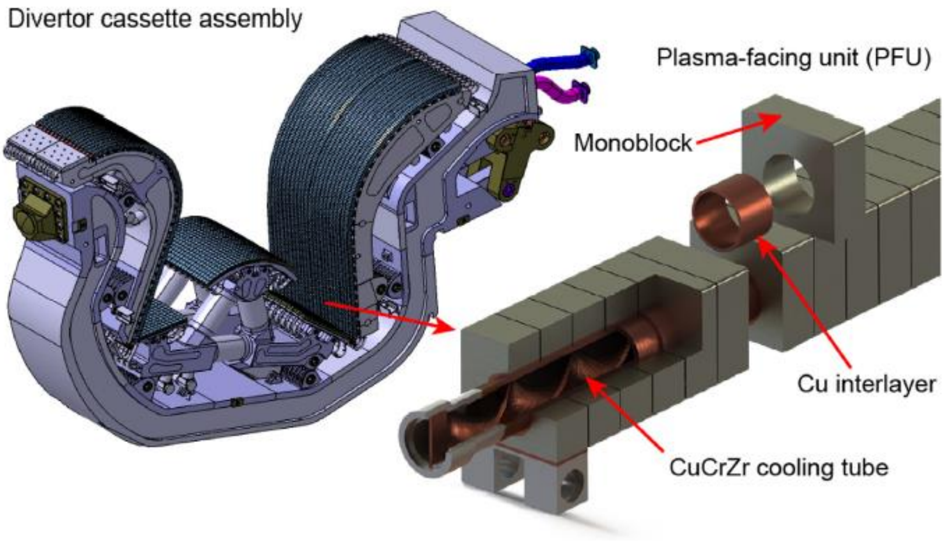

Figure 2.7. Detailed view of the monoblock design of the plasma-facing units (PFUs) in the ITER divertor [17].

2.4. Plasma facing materials (PFMs)

The materials chosen as plasma facing materials for ITER require certain specific characteristics to be able to be utilized in such demanding conditions. Furthermore, due to the time required to develop and qualify innovative materials, it was decided to use industrially available materials only. In order to qualify as a PFM, materials should have [20–23]:

- High melting temperature
- High thermal conductivity
- Resistance to thermal fatigue
- Low atomic number (Z)
- Low erosion rate (low sputtering yield)
- Low tritium retention
- Resistance to neutron irradiation and activation
- No long-term activation

A high thermal conductivity will allow the materials to be cooled more effectively. In plasma-facing components subjected to high fluxes there can be a temperature gradient in the order of 10^6 $\mathrm{Km^{-1}}$. A high melting point will make them more resistant to damage if the cooling elements are not able to keep temperature low enough. A low atomic number is also preferable, higher Z materials will radiate more if they come into the plasma. Plasma impurities of low Z materials, such as beryllium, can reach 1 % of the plasma without compromising its stability. For tungsten, with a Z of 74, it has been found that keeping it below 10^{-5} should keep the plasma from cooling down critically. For this same reason, a low erosion rate when impacted by plasma particles prevents the plasma from being contaminated by the PFMs [23–25].

As mentioned at the beginning of the chapter, tritium is hard to obtain, and it is also radioactive. This means that if tritium permeates the materials and is trapped, it might reduce the amount of fuel in the plasma and hinder the fusion reactions. It will also pose a security hazard in case of a loss of coolant accident (LOCA). With a large accumulation of tritium in the material and a lack of coolant during a LOCA, decay heat could catastrophically heat the materials [26]. Additionally, a large amount of trapped tritium would increase the amount of tritium released into the environment in case of a leak in the vacuum vessel. For these reasons, a maximum releasable working limit for tritium in the vacuum vessel has been set to 700 g. Hence, materials with low tritium retention are necessary.

The physical properties of most materials deteriorate when bombarded with neutrons, which could lead to damage to the reactor in the long-term. Neutrons can also lead to the transmutation of materials. So, to reduce risks and nuclear waste, it is important for materials to not produce long lasting radioactive products. This factor alone eliminates most elements in the periodic table from being considered as PFM [27–29].

Such requirements leave no available material to be used, as certain desirable characteristics, in fact, conflict with each other. A low Z material will have a lower melting point and a high erosion rate. Therefore, compromises had to be made in order to select the best materials, and since the beginning of the ITER planning phase, there have only been three suitable materials: beryllium, carbon (graphite and carbon-fiber composites, or CFCs) and tungsten. The advantages and disadvantages of each can be seen in Table 2.2 [23,30].

Table 2.2. Advantages and disadvantages of the possible plasma facing materials for ITER [21,23,29,31,32].

	Advantages	*Disadvantages*
Beryllium	• Low Z • Low tritium retention • Oxygen getter • Neutron multiplier for tritium breeding blanket • High thermal conductivity	• Low melting point • High toxicity • High erosion rate • Tritium retention by co-deposition
Carbon	• Low Z • Does not melt • High thermal conductivity	• Forms compounds with tritium • High tritium retention due to co-deposition • High erosion rate
Tungsten	• Highest melting point of all elements • Low tritium retention • Low erosion and sputtering yield • High thermal conductivity	• High Z • High ductile-brittle transition temperature (DBTT) • Embrittlement by neutrons • Recrystallization at high temperatures • Blistering by plasma irradiation

In ITER, beryllium was selected for the first wall, which covers most of the walls of the vacuum vessel. The first wall will receive most of the neutron irradiation, but relatively low thermal loads compared to the divertor. Beryllium is less brittle than tungsten at lower temperatures and the plasma will be less affected by the presence of beryllium impurities, making beryllium a better option for this purpose. However, tungsten will most probably be used as first-wall material in future reactors such as DEMO. This depends on the development of tungsten alloys or tungsten composites which lower its ductile-brittle transition temperature and lower the risk of oxidation in case of an incident where oxygen enters the vacuum vessel [21,22,33,34].

Tungsten will be the material utilized for the ITER divertor PFMs. Carbon was selected at first to be used in the strike points of the first divertor to be used in the non-nuclear phase of ITER. It would allow for some flexibility on the plasma parameters at the start of operations. Tungsten has a higher ductile-to-brittle transition (DBTT) than carbon, which might present problems when the reactor walls are still relatively cold. It is hard to set a definite range for DBTT, as it varies with several factors such as purity and thermomechanical treatments. For tungsten it tends to vary from room temperature to around 600 °C for most tungsten grades [35,36].

After the first testing phases, the divertor cassettes would then be replaced for full tungsten cassettes in preparation for full DT operation. CFCs are unsuitable for DT operation because of their chemical reactions with tritium, and the high tritium retention by co-deposition, as well as the rapid degradation of its thermal conductivity with displacements in their microstructure. In fact, in preparation for ITER, JET changed its inner walls from CFC panels to beryllium and tungsten ones. This new configuration is called ITER-like wall (ILW). Retention was reduced by a factor of 10 when comparing the previous CFC walls and the new ILW. The decision was then made to use a full tungsten divertor from the beginning, as this will spare the costly step of replacing the cassettes, and it is considered that enough data about the plasma parameters can be gathered without damaging the divertor. The loads that the divertor will have to sustain during its lifetime are explained in the next chapter [16,37–40].

2.5. Heat loads

During normal operation, the ITER divertor will be constantly bombarded by different kinds of particles, which can have damaging effects on the materials. Heat will also radiate from the plasma itself or can be transferred from the colliding particles into the material. These loads will undoubtedly have an effect on the materials, which can be detrimental to their physical properties and therefore to their function in the fusion reactor. Figure 2.8 shows a summary of the heat loads expected in the ITER divertor [41].

During a full-operation ITER pulse, the divertor will be subjected to a steady-state heat load of 10 MWm^{-2}, with slow transients lasting several seconds and depositing up to 20 MWm^{-2}. The former can take the vertical targets of the divertor above their recrystallization temperature of 1100-1400 °C (for most tungsten grades) [42–44], while the latter can take the surface to up to 2200 °C and some leading edges near melting temperatures. Leading edges are of particular concern. Plasma particles will impact the monoblock tiles along magnetic field lines at a grazing angle and can deposit disproportionally more heat in leading edges than in the rest of the surface [36,42,43,45].

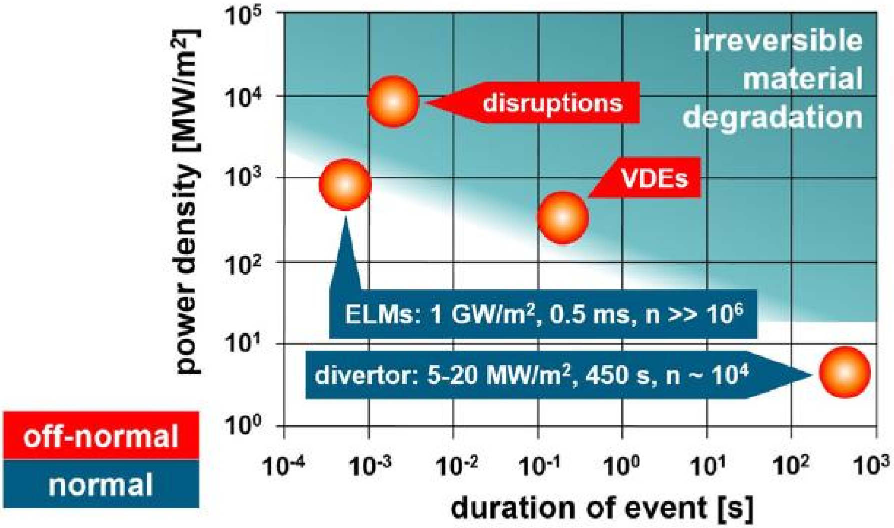

Figure 2.8. Heat loads expected to be deposited on the ITER divertor. The loads expected in normal operation are shown in blue, while those caused by irregular events are shown in red. The turquoise area shows the approximate range that will cause permanent damage to the PFMs, not taking particle loads into account [41].

If sufficient heating power is applied in a tokamak, the high plasma confinement mode known as H-mode is achieved. This considerably reduces plasma turbulence and increases confinement. In H-mode, a steep pressure gradient is formed around the separatrix in what is known as the pedestal region (see Figure 2.6). This pressure gradient is periodically relaxed by the release of energy during edge-localized modes (ELMs). These ELMs cause a portion of the stored energy and particles in the plasma to be released, depositing large amounts of this energy in the tokamak walls in a short period of time.

It has been calculated that unmitigated ELMs in ITER could deposit more than 10 GWm^{-2} in the divertor [41], which would lead without a doubt to the worst-case scenario of a full-surface melting of the monoblocks and a catastrophic failure of the components. ELM mitigation is, therefore, strictly necessary during DT operation. There are different kinds of ELMs, but those most relevant to ITER are known as type I ELMs. By extrapolation from smaller tokamaks, it is expected for ELMs in ITER to deposit, in the more optimistic scenario, about 1 MJm^{-2} into the divertor. This value could, however, be in the range of 10-30 MJm^{-2}, or up to 1 GWm^{-2} in a sub-millisecond burst [46]. These events will occur with a frequency of 1 Hz or more, amounting to millions of ELMs during the lifetime of the divertor [46–50].

Off-normal events can also occur in ITER. The thermal quench during disruptions can deposit up to 30MJm^{-2} in a few milliseconds and severely damage the PFCs, mainly because of the effect of runaway electrons. Vertical displacement events (VDEs) are a loss in the vertical control of the plasma, which can cause it to impact the walls of the reactor. VDEs can deposit up to 60 MJm^{-2} in 100-300 ms and hundreds of them might occur during the divertor's lifetime, in particular during the first stages of the reactor [25,41,51,52].

Figure 2.9 illustrates the effects of transient thermal events on the surface of a metallic material. At the moment of the power deposition the affected area heats up and expands. The colder material surrounding it does not expand at the same rate and causes a compressive stress, forcing the high temperature area to swell. If the heat flux is high enough, melting can also occur. Once the material cools down, some permanent changes can be seen, depending on the power density of the thermal shock. Effects such as surface roughening, cracking, recrystallization, grain growth and melting can be caused. These have been observed by simulating ELMs with high heat flux devices as, for instance, electron beam facilities and lasers [19,25,50,53,54]. Additionally, ELMs are expected to be the main source of erosion on the ITER divertor. Most eroded material will redeposit near its source, but a portion of it might enter the core of the plasma, which would cool the plasma down [55].

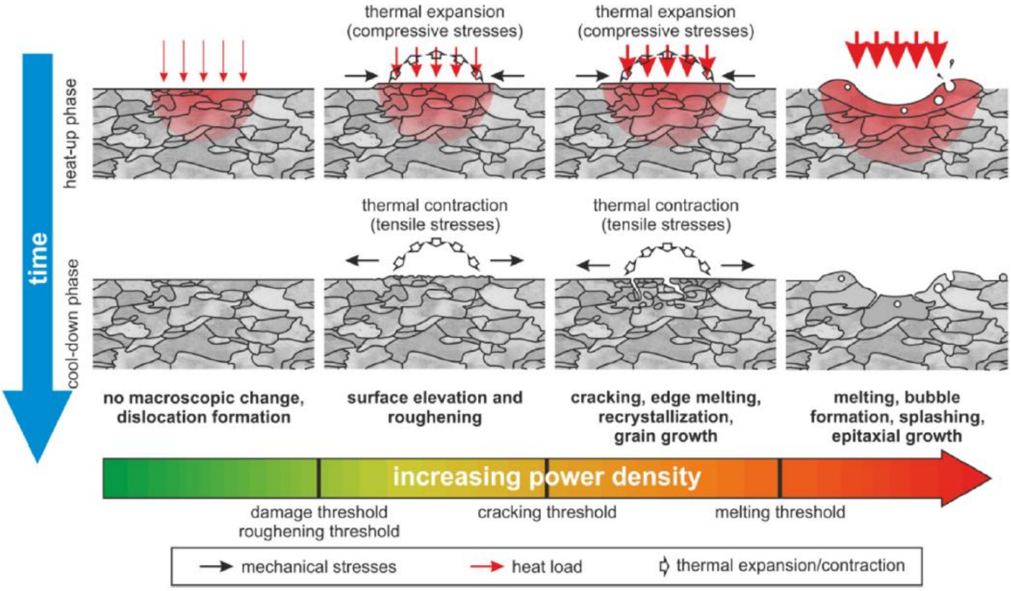

Figure 2.9. Illustration of the effects that transient thermal loads can have on the surface of a metallic material such as tungsten [25].

2.6. Particle loads

Energetic particles can cause different issues than the heat loads by themselves. The divertor will have to undergo collisions from ions, electrons and fusion neutrons with up to 14 MeV of energy.

Fusion neutrons can change the crystal structure of the PFMs by causing the displacements of atoms in the lattice. In the PFMs in the ITER divertor, about 0.5 displacements per atom (dpa) are expected [25]. This causes defects in the material such as voids and dislocation loops and can lead to increased brittleness and, depending on the conditions, energy and type of irradiating particles, either decrease or increase the hardness of the material [56]. Furthermore, neutron irradiation can also cause transmutations in the material. As mentioned above, one of the reasons why tungsten is a good option as a PFM is because it produces no long-lived radioactive isotopes, but the change in chemical composition can still have an effect on its mechanical and thermal properties. The main transmutation products of tungsten are Re, Ta, and Os. If the concentration of these products is high enough, it can even lead to a separation of phases, which would increase the brittleness of the material even more [28,56–63].

Near the divertor strike point, a flux of ions and neutrals of > 10^{24} $m^{-2}s^{-1}$, which translates into a fluence of over 10^{26} m^{-2} per pulse, and of 10^{30-31} m^{-2} during the divertor lifetime [64]. A D^+ impact energy of 15 keV is to be expected due to the plasma sheath potential. The impact of hydrogen and helium particles has been shown to cause blistering of tungsten surfaces and formation of nanobubbles under the surface, at temperatures below 1000 K. At higher temperatures, larger bubbles and pits can form [65–72]. Additionally, deuterium and helium implantation can have a strong influence on the hardening of the material. Helium has a tendency to bind in helium-vacancy complexes, a phenomenon that is then highly influenced by the concentration of vacancies in the material, and especially near the surface where the material is impacted by the helium particles, as the highest helium concentration is found in the near-surface area [73]. The hardening by deuterium implantation has been attributed to dislocation forest hardening and the pinning of dislocation by the deuterium atoms. This effect was shown to be reversible and the material recovered its original hardness after deuterium was desorbed [74].

Another phenomenon that has been observed due to helium ions impacting the tungsten surface is the growth of thin tungsten tendrils known as tungsten “fuzz”. Growth of tungsten fuzz was initially observed on tungsten-coated graphite, and it has been studied thoroughly since then [75]. The formation of these nanostructures seems to occur at temperatures above 900 K. Helium particles are implanted and eventually coalesce, forming helium nanobubbles. These nanobubbles cause the material to swell and form protrusions and holes in the surface. This process eventually leads to the formation of the tendrils, as schematically represented in Figure 2.10 [76,77]. Fuzz formation could potentially increase erosion rate in PFMs and generate a thermal barrier which disrupts heat dissipation. This thermal barrier could further worsen the damage inflicted to the components. Above about 1500 K, however, tungsten fuzz stops forming and eventually disappears due to the diffusion of the tendrils back into the bulk. In the strike point area, high transient heat loads might prevent fuzz growth. This effect could, however, still be seen in other areas of the divertor where surface temperature is not high enough to hinder its formation [41,66,75–79].

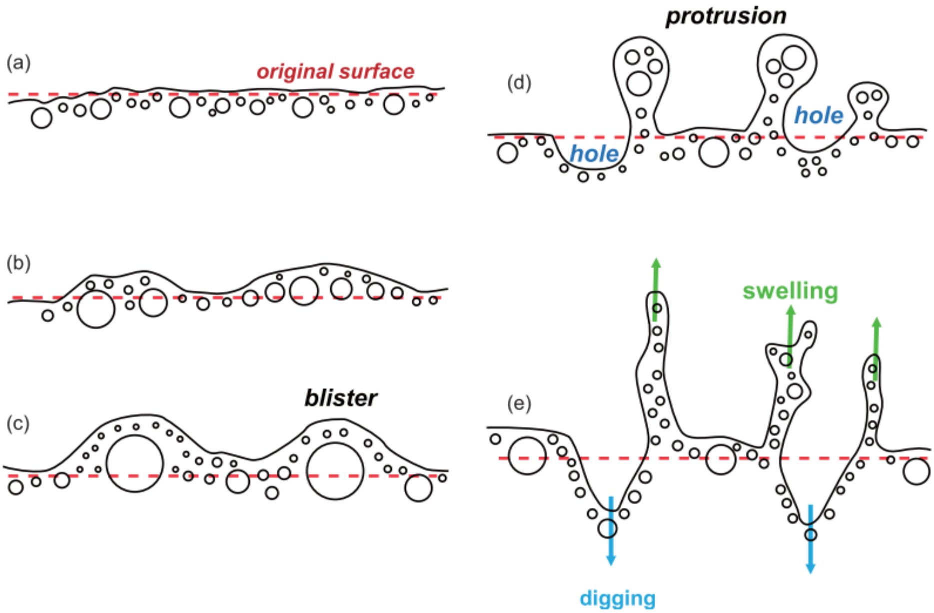

Figure 2.10. Schematic of the formation of tungsten nanotendrils or "fuzz". The implanted helium particles coalesce into nanobubbles and eventually into blisters. This process causes protrusions and holes in the material which then form the nanotendrils [76,77].

2.7. Synergistic heat and particle loads

Having described the conditions, the divertor must withstand in a large fusion reactor such as ITER and having discussed the effects the different kinds of loads can individually induce on the material, it is important to study the synergistic effect these might have. Currently, no fusion device can reach the loads expected in the ITER divertor, and no other device can simulate these conditions fully. Several tests have been made in linear plasma generators such as PSI-2 (plasma-surface interaction) at Forschungszentrum Jülich and in Magnum-PSI at DIFFER (Eindhoven). Tungsten fuzz, which is generated under helium bombardment of tungsten, might or might not form, depending on the surface temperature. Sufficiently energetic thermal loads could take the surface temperature into the tungsten fuzz formation window, or, if they are energetic enough, increase the surface temperature and cause any tendrils that form to rediffuse into the material. Increased bubble formation has also been observed when both kinds of loads are applied. Most experiments, however, have been performed with a relatively low number of thermal shocks compared to those expected in ITER. The synergistic effects the PFMs will undergo during their lifetime remain, therefore, not completely understood [80–85].

3. Scope of the thesis

ITER will be the largest fusion device ever built until now. Its size and capabilities will surpass the previous largest tokamak, JET, by almost an order of magnitude. This will allow scientists to gather data about plasma physics, engineering, technology and materials. At the same time, it also means that there are still many unknowns, which are almost impossible to foresee until the actual reactor is up and running. One of the big unknowns has to do with the materials that will be used for the inside of the vacuum vessel, known as plasma facing materials. These materials need to be able to withstand the conditions inside the reactor, for this, they need to have high melting points and thermal conductivities, be resistant to neutron embrittlement, not produce long-lived transmutation products, have a low erosion yield and have a low tritium retention. These demanding conditions leave few materials suitable for ITER. Initially, three main materials were selected, beryllium for the first wall, tungsten for most of the divertor and CFC for the divertor strike points, where the highest loads would have to be sustained. Finally, the decision was taken to exclusively use tungsten in the divertor, as this eliminates the need to replace the divertor before DT operation (see section 1.4).

Tungsten will be subjected to high steady-state and slow transient heat loads, which can bring the temperature within the recrystallization temperature. This means that the physical properties of the PFMs will be modified, and the material might become brittle even at such high temperatures. In some cases, there might even be local melting. Transient thermal loads also need to be accounted for. ELMs pose, arguably, the largest threat to the ITER divertor. They will be the largest source of tungsten erosion. Additionally, they will cause a constant expansion and compression of some areas (Figure 2.9), which will induce surface roughness and cracking, as well as formation of blisters and bubbles (see section 1.5). Aside from the thermal loads, PFMs will also be subjected to a large particle flux in ITER. Neutrons can cause embrittlement of the materials by modifying their crystal structure, as well as transmutation. Transmutation can generate not only radioactive isotopes, but also elements that change the characteristics of the material. Bombardment by ions and neutrals can have other effects. These include the formation of bubbles below the surface, erosion of the material and formation of tungsten fuzz (see section 1.6).

Currently, no device can replicate the exact conditions that the ITER divertor will have to withstand. However, linear plasma generators coupled with a high-power laser can simulate the effect of ion bombardment and periodic thermal shocks such as ELMs. PFMs have been previously tested in these conditions; however, no tests have been performed that try to simulate the full loads the divertor will sustain throughout its lifetime (see section 1.7). This work tries to clear this unknown and shed some light on the effects of ITER-relevant synergistic particle and heat loads on tungsten.

The linear plasma device PSI-2 was used to test ITER-grade tungsten samples provided by PLANSEE AG in Austria. These samples were exposed to conditions similar to those of PFMs in the ITER divertor during full DT-operation. In chapter 3, the results of these tests are shown. Both as-received sample with needle-like grains transversal to the surface and recrystallized samples were tested, to compare the influence of microstructure in the behavior under these conditions. First, the individual effects of heat and plasma loads were analyzed separately, to have a point of comparison and know which effects can be observed under which loads. Later, both kinds of loads were applied simultaneously to evaluate the synergistic effects and be able to more accurately predict how tungsten PFMs will behave in ITER.

Different kinds of effects were studied in this work. First, effects of the particle and heat loads on the surface of the sample, such as the formation of cracks and the increase in surface roughness, were determined. Other effects were then studied, including the effects of these loads on the residual stresses, which can influence the mechanical characteristics of the material. Other observed effects that will be analyzed on chapter 3 are the recrystallization and grain nucleation of the microstructure of the samples, as well as the formation of bubbles underneath the loaded surface and their possible effect on the physical and thermal behavior of the samples. The sum of these effects will help have a deeper understanding into the conditions that the PFMs in the ITER divertor will be able to withstand, and how their characteristics will change throughout their lifetime.

4. Test facilities and analysis methods

In order to assess the behavior of tungsten plasma facing materials for the ITER divertor, it is necessary to simulate the conditions the material will be required to sustain. There is currently no device which can accurately simulate these conditions. The materials in a fusion reactor, particularly in the divertor, will be bombarded with highly energetic ions and neutrons, which will cause activation, displacements and thermal shocks. The behavior of the materials when all these effects are combined simultaneously is of particular interest. Neutron sources for material studies were not used for this work, but synergistic loads caused by plasma particles and thermal shocks were studied using the linear plasma device PSI-2.

4.1. PSI-2

Tungsten samples were subjected to fusion relevant particle and heat loads with the linear plasma device PSI-2 at the Forschungszentrum Jülich [86]. This device was designed to produce loads similar to those that the divertor region inside fusion reactors such as ITER will have to withstand. This allows the effects caused by these loads, such as deuterium retention, erosion and cracking to be studied.

A schematic view of the device is given in Figure 4.1. In PSI-2, steady-state plasma is produced under vacuum by a high-current arc between a LaB_6 cathode and a molybdenum anode which is subsequently directed towards the target stage by an axial magnetic field. The plasma profile has the shape of a hollow circle with an outer diameter of 6 cm and a maximum plasma flux at a radius of 2.5 cm from the center of the ring. The plasma profile can be seen in Figure 4.2. The samples are placed accordingly in order to ensure a uniform plasma exposure. The maximum plasma flux that can be obtained at PSI-2 is of the order of 10^{23} $m^{-2}s^{-1}$ and the incident ions can have an energy of up to 200 eV and electron temperatures of T_e = 1-40 eV [86–88].

The plasma can be composed of deuterium, helium or other gases, or be a mixture of two or more of them. To determine the plasma flux, a double Langmuir probe is used. The probe has a radial resolution which is determined by the size of its tips (1.5 mm) [87]. Langmuir probes are essentially electrodes that are introduced into the plasma. A variable potential (V_p) is applied to the probe and the current-voltage curves generated in relation to V_p is analyzed to determine the different plasma parameters [89].

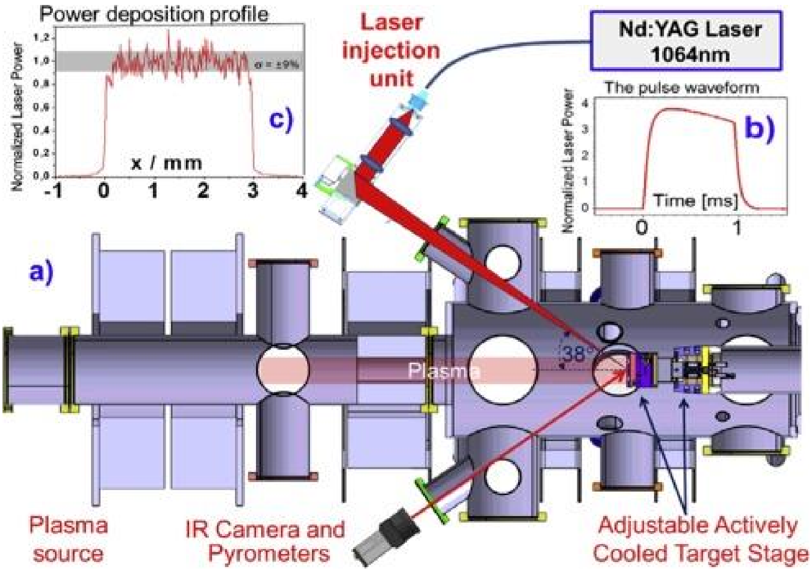

Figure 4.1. Schematic view of the linear plasma device PSI-2 located at the Forschungszentrum Jülich. It can simulate the conditions inside a fusion reactor with its steady-state plasma source and its pulsed Nd:YAG laser [88].

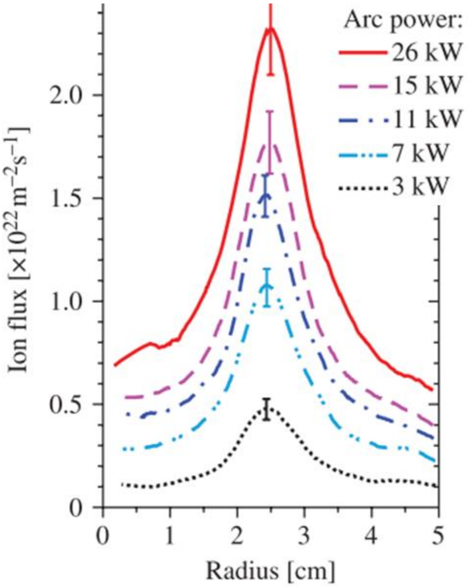

Figure 4.2. Typical plasma radial profiles of the ion flux of deuterium plasmas generated in PSI-2 [86].

Simultaneously, a Nd:YAG laser with a wavelength of 1064 nm is used to generate transient heat loads such as those expected from ELMs. Heat loads on the sample can reach power densities of up to 3 GWm^{-2} per 1 ms pulse in a circular area with a diameter of approximately 3 mm. The laser has a square power deposition profile, meaning that the target area is struck evenly and there is only a very thin transition area [87,88].

Temperature is controlled via a thermocouple (type K) at the back of the sample. Surface temperature could also be monitored with a thermal imaging camera to determine the temperature peaks during the thermal shock events, which would not be reflected accurately in the temperature measurement with the thermocouple.

4.2. Laser profilometry

Laser profilometry was used to characterize the surface of the samples, both before and after being exposed to particle and heat loads. The analyses were performed with a profilometer from OPM GmbH which has a KF3 confocal sensor. The sensor has a vertical resolution of 0.02 µm and a lateral resolution of up to 2000 points/mm. This technique is especially useful to determine sample roughness, changes in the morphology of the samples and cracking.

4.3. Scanning electron microscopy (SEM)

SEM is a technique in which an electron beam, typically in the keV energy range, is focused on the surface of a sample. The electrons then interact with the surface atoms and are scattered. Incoming electrons typically only penetrate the first few micrometers of the material, depending on their energy and the material itself, penetrating lighter elements deeper than heavier ones. These interactions generate backscattered electrons (BSE) and secondary electrons (SE). BSE convey information such as average atomic number, surface topography and crystallographic orientation. The SE that are generated depend on the topography of the surface as well, but also show differences in chemical state. Resulting SEM micrographs can have a resolution in the sub-micron scale, making it an useful technique to study the microstructure of the surface of a sample [90]. No sample preparation was necessary, as the surface of all samples was conductive enough for SEM imaging to be performed.

4.4. Focused ion beam (FIB)

SEM utilizes a focused electron beam on a sample to image it. Electrons have a low mass compared to atoms, so they are not able to remove material from a sample. But if instead of electrons, highly energetic heavy ions are focused on a certain area, material can be removed from the surface. This is called focused ion beam (FIB) milling. For this technique, gallium ions from a liquid metal source are typically used. The most commonly used FIB devices are SEM/FIB coupled devices, in which both sources are focused on the same point. This way, via Ga^+ FIB milling, a cross-section of the sample surface can be cut and then imaged via SEM, allowing the study of the microstructure of the material under the surface. A thin platinum layer is added when performing the milling to prevent artifacts in the end surface [90].

4.5. Electron Backscatter Diffraction (EBSD)

When a polycrystalline sample is investigated under an SEM, depending on the crystal orientation of the individual grains, some of the electrons will get diffracted according to the Bragg equation and form conical patterns with varying degrees of intensity. These patterns are called Kikuchi lines, and can be used to determine the crystalline orientation of the grains. Electron backscatter diffraction (EBSD) is the technique which utilizes this phenomenon to produce a “map” of the crystal orientations in a sample’s surface, similar to an SEM micrograph, but identifying more accurately the grain boundaries and crystal orientations of each individual grain. The sample surface should be flat, with low roughness, otherwise, the morphology will affect the scattering and diffraction of the electrons. In fact, this technique can also be utilized to differentiate between different textures present in a surface. Samples are placed in a steep tilted angle to ensure that the beam only penetrates the top few nanometers of the material [90,91].

4.6. Preparation and analysis of sample cross-sections

For this work, cross-section cuts of samples were performed. The resulting cross-section was then chemically etched with an H_2O_2-NH_3 solution. These could then be investigated via light microscopy to analyze the damage and microstructural changes caused by the exposure to fusion relevant loads at varying depths under the laser spot. This method was also utilized to prepare the sample surface for the nanoindentation tests (see section 2.7).

4.7. Nanoindentation

The indentation method consists of pressing a tip, generally a diamond tip, into the surface of the material and measuring the depth of penetration. The depth of penetration will be proportional to the force (load) applied. By comparing the relationship between these two, important physical characteristics can be deduced, such as hardness and Young's modulus (E) [92].

Of relevance to this work is nanoindentation, which applies indents in the nanometer scale, which allows for the testing of individual grains. For brittle materials, such as tungsten at room temperature, pyramidal diamond tips are mostly used. For this work, a Berkovich (three-sided pyramid) tip was used (a typical indent performed with a Berkovich tip can be seen in Figure 4.3). To determine hardness via nanoindentation, the most commonly used definition of hardness is the Meyer hardness (H), given by the equation

$$H = \frac{P}{A} \tag{2.1}$$

where P is the applied load and A is the projected area of contact, and depends on the tip geometry. In this sense, H equals the mean contact pressure at full load. Young's modulus is determined from the slope of the unloading of the load-displacement curve (as seen in Figure 4.3). The slope corresponds to the indentation modulus (E_{IT}) which, in ideal scenarios, equals E. The value of E_{IT} can be modified material behavior that is not accounted for in the analysis, such as piling-up [92,93].

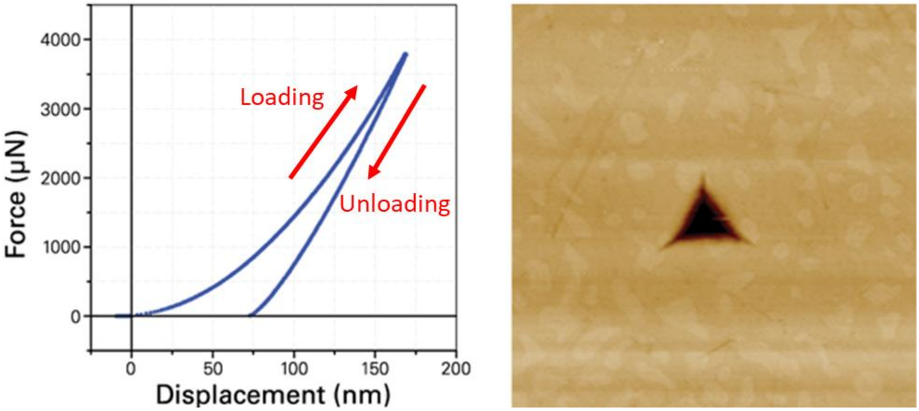

Figure 4.3. Left: Typical load-displacement curve obtained in a nanoindentation measurement. Right: Indent left by a Berkovich tip on a quartz surface after a nanoindentation measurement [93].

The nanoindenter utilized in this work was a Bruker Hysotron nanoindenter, which provides the possibility of coupling it with an SEM. By doing this, nanoindents could be made in individual grains of a cross-section cut to analyze the influence of the applied particle and heat loads on the physical characteristics of the samples and to analyze how deep into the sample bulk these loads have an effect. Additionally, EBSD was applied to compare the physical parameters obtained to the crystal orientation of each of the grains that were tested to analyze whether there is a relationship between grain orientation and the effects of fusion relevant loads on the hardness of the grains.

4.8. X-ray Diffraction (XRD)

Diffraction methods are based on the constructive interference of waves. Crystalline materials have a regular spacing between their atoms which makes them suitable for diffraction techniques. Due to the lattice spacing in most materials, light in the X-ray region of the spectrum is most relevant, according to Bragg's law:

$$\lambda = 2d_{hkl}\sin\theta_B \tag{2.2}$$

where λ is the wavelength of the incoming beam, d_{hkl} is the lattice spacing in the *hkl* lattice orientation and θ_B is the Bragg angle. The Bragg angle is defined as the angle between the incident beam (L_0) and the lattice planes, or half of the angle between the incident beam and the diffracted beam (L_D). If the wavelength fulfills Bragg's law, there will be constructive interference which can be detected and identified as a *diffraction peak*. When a material is strained, the lattice spacing in the grains changes, which in turn causes the diffraction peaks to shift, as can be seen in Figure 4.4 [94].

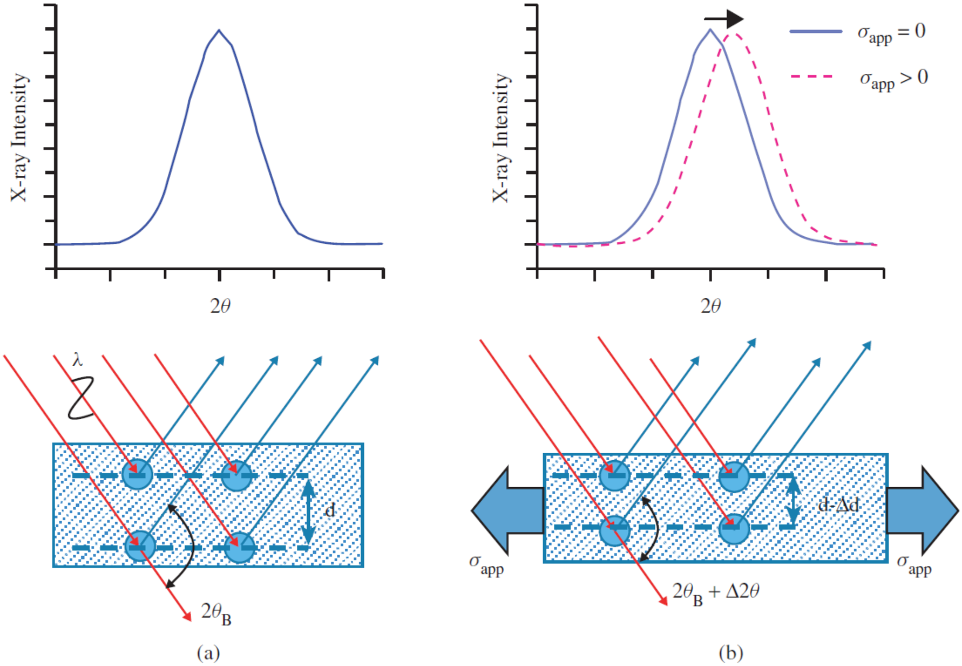

Figure 4.4. Diffraction peak in an unstrained crystalline material (a) and the shift of its peak when a tensile strain is applied (b) [94].

The shift in the peak will be proportional to the magnitude of the strain. This shift can then be used to measure the amount of strain and, therefore, stress, in a sample. By rotating the sample in the direction of the incident beam (Ψ angle, illustrated in Figure 4.5), the direction of the stresses can be twisted. This will, in turn, influence the peak shift. These shifts can afterwards be plotted in the form of the lattice spacing at a fixed φ and varying Ψ angle (d_Ψ) against $\sin^2\Psi$.

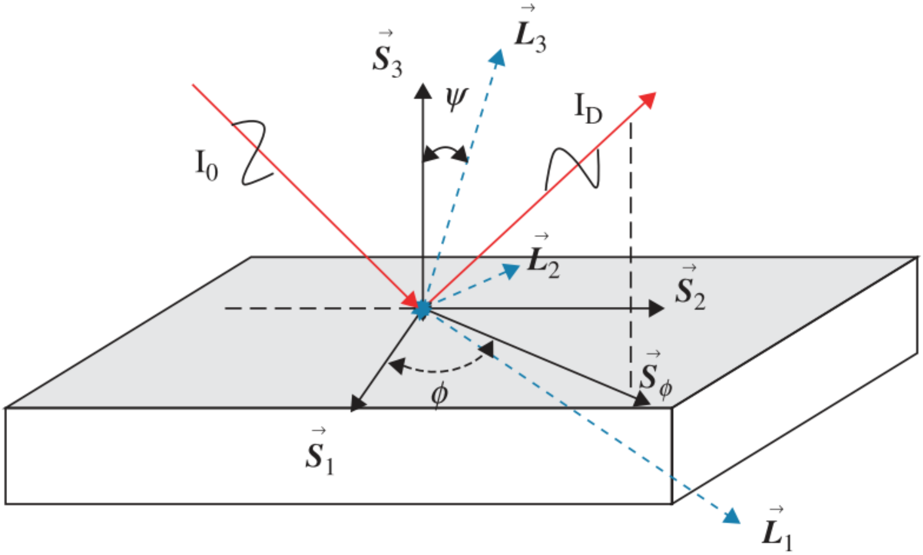

Figure 4.5. Definition of the laboratory $(\overrightarrow{L_\iota})$ and sample surface $(\overrightarrow{S_\iota})$ coordinate systems. It shows also the rotation angles between both, φ and Ψ; as well as the indent (I_0) and diffracted (I_D) beams [94].

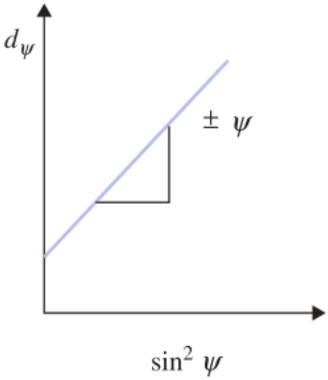

Figure 4.6. Illustration of a plot of the lattice plane spacing (d_Ψ) against $\sin^2\Psi$ [94].

The stress present in the sample can then be calculated from the slope of the plot (Figure 4.6) according to equation 2.2:

$$d_\Psi = \frac{1+\nu}{E} d_0 \sigma_\varphi \sin^2 \Psi - \frac{\nu}{E}(\sigma_{11} + \sigma_{22}) d_0 + d_0 \qquad (2.3)$$

where ν is Poisson's ratio, E is the Young's modulus, d_0 is the unstrained lattice spacing, σ_φ is the surface stress along $\overrightarrow{\boldsymbol{S}_\varphi}$, and σ_{11} and σ_{22} are the stresses along the sample surface. As seen in the equation, the slope (m) of the d_Ψ vs. $\sin^2\Psi$ would be equivalent to:

$$m = \frac{1+\nu}{E} d_0 \sigma_\varphi \qquad (2.4)$$

This method, called the $\sin^2\Psi$ method, is useful to calculate the residual stresses in a sample, which can have an important effect on its physical properties.

5. Effects of fusion relevant particle and heat loads on tungsten

In sections 1.4-1.7 it was described how PFMs in a fusion reactor are exposed to harsh conditions that can eventually lead to a catastrophic failure in the material and prevent the fusion reaction from taking place. Damage can come from two main sources, thermal shock events and particle collisions. Thermal shock events are caused mostly by the energy transfer from high temperature particles from the plasma and can cause the rapid heating and successive cooling of the materials and components. This rapid expansion and contraction can cause cracking of the material, in particular because the thermal shocks occur in a specific area in the material, which means there will necessarily be a temperature gradient, with the ensuing expansion and contraction at different rates through the material. The collision of highly energetic particles against the materials causes different kinds of damage compared to thermal shocks. Particles can come either from the plasma, ionized particles, or from neutrons generated by the fusion reaction. These collisions cause point defects in the materials and, depending on the energy of the collisions, cause a collision cascade. These changes can degrade the physical and thermal properties of the material, making it more brittle, susceptible to erosion and reducing its thermal conductivity. These defects could also potentially cause the PFMs to retain a higher amount of gases. This is particularly serious in the case of tritium, as tritium is radioactive and difficult to obtain. Its retention decreases the amount of tritium available to continue the reactor and, most importantly, it makes the components less safe and thus complicated to handle since they would contain radioactive particles. Thus, a tritium retention as low as possible is desirable, and according to the safety guidelines, less than 1 kg of tritium should be retained in the walls of the reactor vessel, to stop an excess of radioactive material from escaping in case an accident occurs where the inner vessel is exposed [95].

In this chapter, tests performed on ITER-grade tungsten in conditions similar to those it will have to sustain during its lifetime in the ITER divertor are discussed. First, the effects of transient thermal events and steady particle loads will be analyzed independently, and afterwards the synergistic effects of both will be studied. Physical parameters such as surface roughness, crack depth and hardness will be utilized to evaluate the damage suffered by the material. Additionally, X-ray diffraction (XRD) will be used to determine the changes in residual stresses in the samples.

5.1. Tungsten

The material used for all tests comes from samples cut from forged tungsten rods produced by PLANSEE AG, with a purity of at least 99.97 wt%. The process of production, seen in Figure 5.1, starts with the low concentration ores, with generally 0.3-2.5 wt.% of tungsten content. The concentration can then be increased to around 60% by crushing, grinding, floating and roasting. Most other impurities are then eliminated by digestion with sodium hydroxide and the sodium tungstates obtained are transformed to tungsten oxide by a series of chemical processes. WO_3 is then reduced in a hydrogen atmosphere at up to 1000 °C to obtain tungsten powder. The mixing and alloying step was omitted in this case as no additional elements were desired in the material.

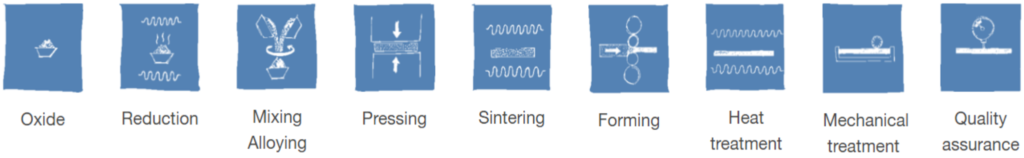

Figure 5.1. Summarized production process of the double forged tungsten rods used to obtain the samples used in all experiments. In this case, no alloying was performed [96].

The tungsten powder was then pressed and sintered at up to 2000 bars and 2000 °C, respectively, obtaining a dense tungsten material. This is then forged two-directionally to obtain the final microstructure with elongated grains (Figure 5.2, a and b) [96].

Double forging of tungsten has been demonstrated to improve its material properties by increasing the strength of the intergranular bindings. The as-received material has a needle-like microstructure. Two different kinds of samples were cut from the tungsten rod, one with its grains oriented longitudinally to the sample surface (L samples) and another with grains oriented transversally to the sample surface (T samples), as both have been considered as PFM for the ITER material [97].

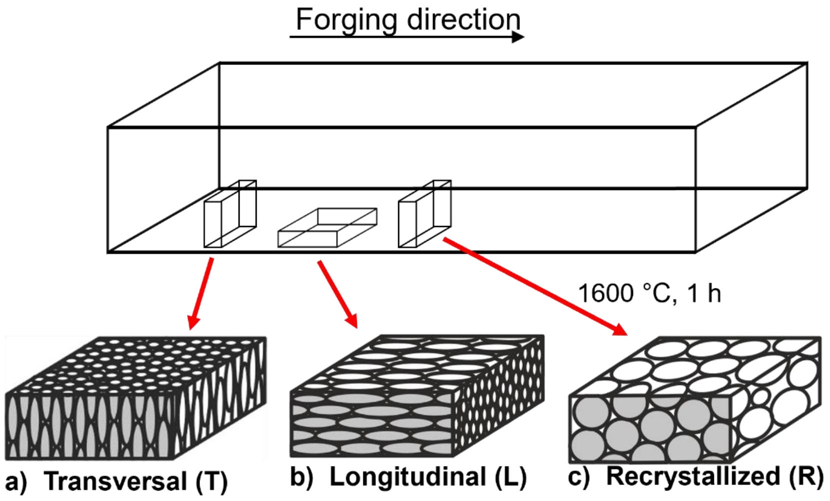

Figure 5.2. Microstructure of the tungsten (> 99.97 wt%) samples utilized. a) Needle-like grains transversal to the surface (T). b) Needle-like grains longitudinal to the surface (L). c) Isotropic grans obtained by heating T samples at 1600 °C for 1 hour to induce recrystallization (R samples).

All samples were cut from a single tungsten rod, with the direction of the grains determined by the way in which they were cut, as can be observed in Figure 5.2. A single sample size was used for all experiments, as it is the standard size of the samples used in PSI-2 tests. The dimensions are illustrated in Figure 5.3.

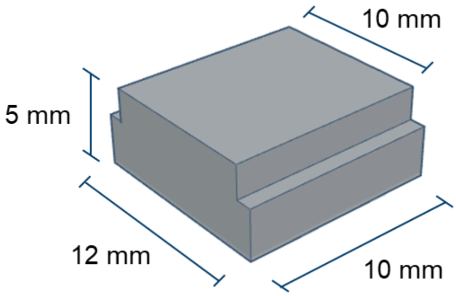

Figure 5.3. Standard PSI-2 sample dimensions used for all tests. The step allows for a correct fit between the sample holder and the mask.

Samples were cut by electric discharge machining (EDM). The top surface of the sample was then grinded and polished to a mirror finish. The final polishing steps were performed with a diamond paste of a maximum particle size of 1 μm and for the final polish, a colloidal silica suspension was used. Afterwards, surface roughness was measured by laser profilometry to obtain an average surface roughness of 0.1 µm in all cases. An even surface without any damage that might have been introduced by EDM or other sources provides a good reference surface to compare the effects that the heat and particle loads will have on the material. After polishing, some of the T samples were heated up in a furnace under inert atmosphere at 1600 °C for 1 hour, obtaining samples with recrystallized grains (R samples), which have larger, isotropic grains.

Finally, only transversal and recrystallized samples were used for the tests. The transversal grain configuration is preferred for the ITER divertor due to its more favorable cracking behavior. The longitudinal grain configuration generates cracking parallel to the surface, which was deemed to be detrimental to the erosion behavior of PFMs and to their heat dissipation capacity. An isotropic grain structure may be obtained either from the fabrication process, such as in spark plasma sintering, or, as in this case, thermal treatment above the recrystallization temperature of the material. By recrystallizing a material, new, strain-reduced grains are formed and keep growing until the strained microstructure is consumed. This process can reduce the strength, hardness and shock resistance of tungsten, as well as causing an increase in its DBTT. In a fusion environment such as ITER, the divertor PFMs are expected to undergo recrystallization in the areas most affected by thermal loads, independently of the selected microstructure [17,35].

A comparison of the cracking behavior of all three microstructures after a thermal shock of 1.13 GW/m^2 during 1 ms can be seen in Figure 5.4. The difference in cracking patterns is caused by the tendency of cracks to expand along grain boundaries. Crack growth parallel to the surface was observed on the samples with longitudinal grains and in those with an isotropic microstructure. This can not only affect erosion behavior as mentioned above, but it also locally restricts the heat removal capacity of the material, which could cause a build-up of temperature near the surface and accelerate the damage suffered by the material [98].

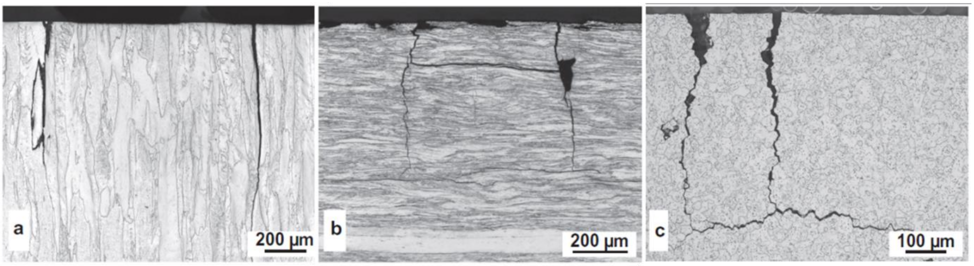

Figure 5.4. Cracking behavior of tungsten samples with needle-like grains transversal to the surface (a), longitudinal to the surface (b) and with an isotropic grain configuration (c). Samples were loading with one 1 ms pulse of 1.13 GWm² absorbed power density [98].

In order to be able to compare the effects of ITER-like loads on tungsten, it is necessary to characterize the as-received material. One important method used to characterize surface modification was the measurement of arithmetic average surface roughness by laser profilometry (R_a). An R_a of 0.1 µm was obtained for both, transversal and recrystallized samples after the sample preparation described above. It is also helpful to compare the microstructure of the material before and after exposure to fusion-relevant conditions. Figure 5.5 shows the chemically etched cross-section cuts of both kinds of samples and showcases the differences in grain size and grain shape of the samples. The needle-like grains in transversal samples can clearly be seen on the left image, with an average length of about 80 µm and an average width of 20 µm. The recrystallized samples have an isotropic microstructure with more clearly defined grains and an average grain diameter of about 50 µm. The range of grain sizes is, however, very broad, with much larger and smaller grains observed. This kind of isotropic microstructure obtained by recrystallization has much larger grains than the one observed in Figure 5.4, which was obtained from the fabrication process.

The recrystallization of tungsten samples, aside from increasing average grain size and modifying the grain shape, changes the material properties. This process strongly reduces defects such as dislocations and increases material ductility, while also decreasing material hardness. This increase in average grain size also leads to a decrease in tensile strength, as predicted by the Hall-Petch relation for polycrystalline materials and can reduce the cracking threshold of the material. This has been observed in previous experiments with fusion relevant loads, where transversal samples show no damage while recrystallized samples already show some cracking and surface roughening [81,98,99].

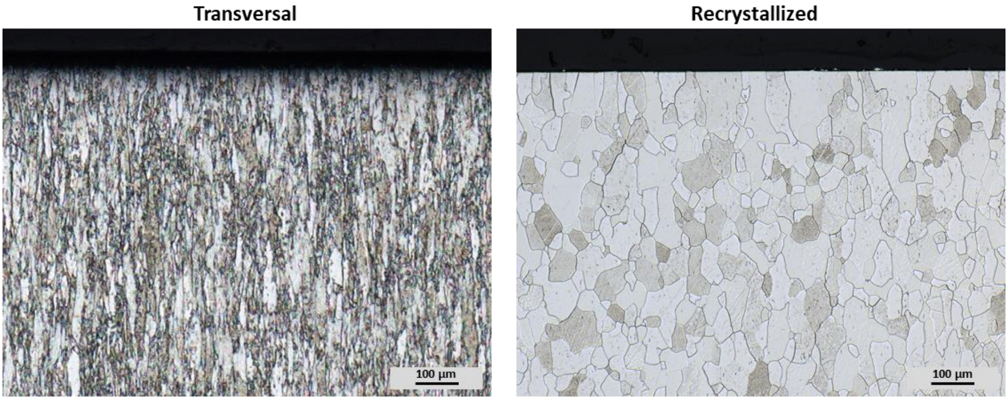

Figure 5.5. Chemically etched cross-section cuts of as-received transversal (left) and recrystallized (right) tungsten samples.

5.2. Individual effects

In order to properly study the synergistic effects of both, plasma and laser loads in the linear plasma device PSI-2, the individual effects of each load must be determined. Once these effects have been investigated, it can be established whether there are any synergistic effects only observed when both types of loads come into play. In all cases, a base temperature of 700 °C was used. This is higher than the DBTT of most tungsten materials and still several hundred degrees below its recrystallization temperature of 1100-1400 °C [36,42,43]. This provides a ductile material behavior such as is expected for the operational range of PFMs in ITER, while ensuring only negligible microstructural changes will take place at the base temperature utilized.

5.2.1. Heat loads

The highest, and, therefore, most damaging, heat loads expected to affect the divertor in ITER during normal operation come from ELMs (see section 1.4). Millions of ELMs will impact the divertor during its lifetime, with a power density of up to 1 GWm^{-2}. To be able to compare these results with the results in previous studies, laser pulses with an absorbed power density of 0.2, 0.4 and 0.8 GWm^{-2} and 0.5 ms of duration were used to simulate the effect of ELMs on the PFMs in ITER. This is equivalent to a heat flux factor (F_{HF}) of 4.5, 9 and 18 MWm^{-2}s$^{1/2}$, respectively. The absorbed power density (P_{abs}) in tungsten samples is about 40% of the applied power density, as measured by a photo diode before and after the laser hits the sample. The remaining energy is either reflected by the sample or absorbed by the windows, mirrors, lenses or fiber-optic cables of the device. To ensure this remains true, samples had to always be located in the same position with respect to the laser beam. The absorption rate has been proven not to change significantly with surface modification in the case of thermal shock tests [100]. This was not tested with the influence of plasma or a higher number of thermal shocks, but it is assumed that the observations are still valid.

To study the damage evolution of the samples, 10^5 thermal shocks of 0.5 ms were applied to a different sample for each of the three power densities. Samples have been studied in previous tests under almost identical conditions, and these results will be presented to follow the damage evolution of the samples with more detail [101,102]. Additionally, 10^6 laser pulses with a P_{abs} of 0.2 GWm^{-2} were also applied to a transversal and a recrystallized sample. Such a high laser pulse number can shed light on the effects that the transient heat events caused by ELMs will cause during the lifetime of the divertor. The frequency of the laser pulses could also have an important effect on the damage observed in the material if it leads to a temperature build-up in the material. It has been observed that for equal power densities, a higher frequency leads to higher damage. This can be explained by the fact that a low pulse frequency allows the material to relax and disperse the excess heat before the next pulse occurs. For the tests with 10^5 pulses, a frequency of 10 Hz was used, as it closely resembles the currently expected ELM frequency in ITER. A frequency of 25 Hz was used for the high pulse number tests due to limitations on the amount of time the device could be continuously operated. 25 Hz is still, however, within the expected frequency range for ELMs in ITER. Using a higher power density at such high frequency would not have allowed the samples to maintain a stable base temperature, as there is no possibility of active cooling in the device. A higher base temperature would, thus, not have permitted a significant comparison to other tests and high pulse number tests at higher power densities were therefore not taken into account for this study [41,103]. A summary of all experiments performed can be seen in Table 5.1.

Table 5.1. Summary of the thermal shock treatments applied to tungsten samples. One sample of each microstructure, transversal and recrystallized, per treatment was tested. Each laser pulse had a duration of 0.5 ms and samples were kept at a 700 °C base temperature.

P_{abs} (GWm^{-2})	F_{HF} (MWm^{-2}s$^{1/2}$)	Number of pulses	Frequency (Hz)
0.2	4.5	10^5	10
		10^6	25
0.4	9	10^5	10
0.8	18	10^5	10

The results from a test performed in the same base conditions with a P_{abs} of 0.4 GWm^{-2} and 10^4 laser pulses is presented in Figure 5.6. As has been established in previous works [104,105], the damage threshold of transversal tungsten lies below 0.4 GWm^{-2}. A considerable surface roughening is observed, with an R_a of 0.66 µm, compared to 0.01 µm for the original tungsten surface. A slight cracking can also be observed in the close-up.

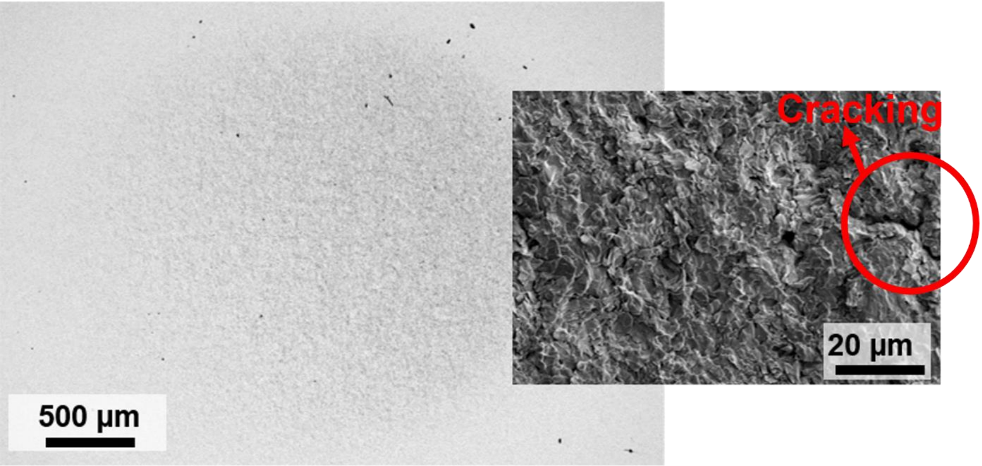

Figure 5.6. Surface modification and damage of a transversal sample after 10^4 0.5 ms laser pulses with a frequency of 10 Hz and an absorbed power density of 0.4 GWm^{-2} at 700 °C base temperature [102].

SEM micrographs of the surface of the samples exposed to 10^5 laser pulses at all three power densities can be seen in Figure 5.7. Some surface modification and light cracking could already be observed after the 0.2 GWm^{-2} tests for both types of samples. The transversal sample shows a smoother surface with some thin cracks and some roughening of the surface. The recrystallized sample displays a rougher surface and the formation of a jagged microstructure. It also formed wider cracks than the transversal one. These can already be seen in the zoomed-out view of the sample, whereas the cracks in the transversal sample are only observable in the close up. These observations go in accordance with previous studies, where it was found that the damage threshold for tungsten lies around the 0.2 GWm^{-2} range, with transversal tungsten showing a higher damage threshold than recrystallized tungsten [50,106].

After exposure to 0.4 GWm^{-2} pulses, a crack network formed on the surface of both materials. The transversal sample shows a larger number of cracks, forming a crack network throughout the area affected by the laser. In the recrystallized case, isolated groups of cracks were formed. This phenomenon also agrees with previous studies, in which at this temperature range recrystallized tungsten displays lower levels of damage than transversal tungsten. This could be attributed to the gain in ductility after the recrystallization process [81].

The close-ups (right side of b and e in Figure 5.7) also show some finer differences in the microstructure. Several sharp, jagged edges formed in the recrystallized sample, showing a shark tooth-like microstructure with triangular sharp formations, while the transversal one has rounder features. This jagged microstructure is still observed after exposure to the highest power density in the recrystallized sample (f) while the transversal one (c) displays a much smoother microstructuring of the surface. This observation comes into contrast with previous studies, where this microstructure was observed in transversal and longitudinal samples, but not in recrystallized ones [105].

The formation mechanism of such structures has been described as having been generated from a process of delamination of the material. This hinders the heat dissipation by creating a thermal barrier, causing the subsequent melting and resolidification of the material into the observed structures (described as scale-like in the past) [105]. In this case, the shape and position of these structures do not seem to match completely those obtained in past experiments, and in some cases do not point to a delamination process as the mechanism behind their formation, particularly for the two highest laser power densities. In these cases, several of these structures are positioned at high angles to the surface, which makes the explanation of their formation by delamination from the surface less probable. Especially problematic for this explanation would be the hindering of heat dissipation once the "scale" starts separating itself from the bulk tungsten. Once thermal conductivity is sufficiently disrupted, heat would begin to accumulate in these structures, and if melting indeed occured, it is more probable that the structures would disappear as a consequence, or that they would be rounder in appearance. Such a delamination process could explain why these structures form in samples with transversal, and particularly, those with longitudinal grains. The thinner grains would facilitate this delamination process, since cracks could form in the grain boundaries, starting the delamination process. The grains could then separate from the surface and the thinner grains would indeed have this jagged shape. This fails, however, to explain why, in this work, the structures are only seen in the recrystallized samples. A more satisfactory explanation for the formation of these structures in this case is that the stresses generated during the expansion and contraction of the material during and right after the laser pulses causes the plastic deformation of the material.

In both cases, after tests with 0.8 GWm^{-2}, there are broad valleys of several hundreds of micrometers in width that are seen mostly in the outer part of the laser spot and extending outside the area directly hit by the laser. This is possibly due to the large temperature gradient at the edges, causing a high thermal fatigue, while the center of the spot is only in contact with other areas also heated up by the laser pulses. The temperature gradient in the edges causes part of the material to expand more than its surroundings, with a subsequent rapid cooling. This causes tensile stresses which in turn can originate cracks [81,82,100]. A smaller gradient in the middle would therefore hinder the appearance of cracks. Another possible explanation, which does not exclude the previous one completely, is that in the middle of the laser spot a higher temperature is reached. This could cause an increase in temperature enough for the material to become plastic enough to prevent cracking. It could even indicate the presence of localized melting, which can serve as a crack closing mechanism. Localized melting has been observed in divertor tiles in JET when replicating ITER-like ELM loads, even if temperatures above the melting point of tungsten could not be detected (due to the low resolution of most diagnostics) [107]. At the highest power densities, no significant difference between the cracking behavior of samples with the two microstructures.

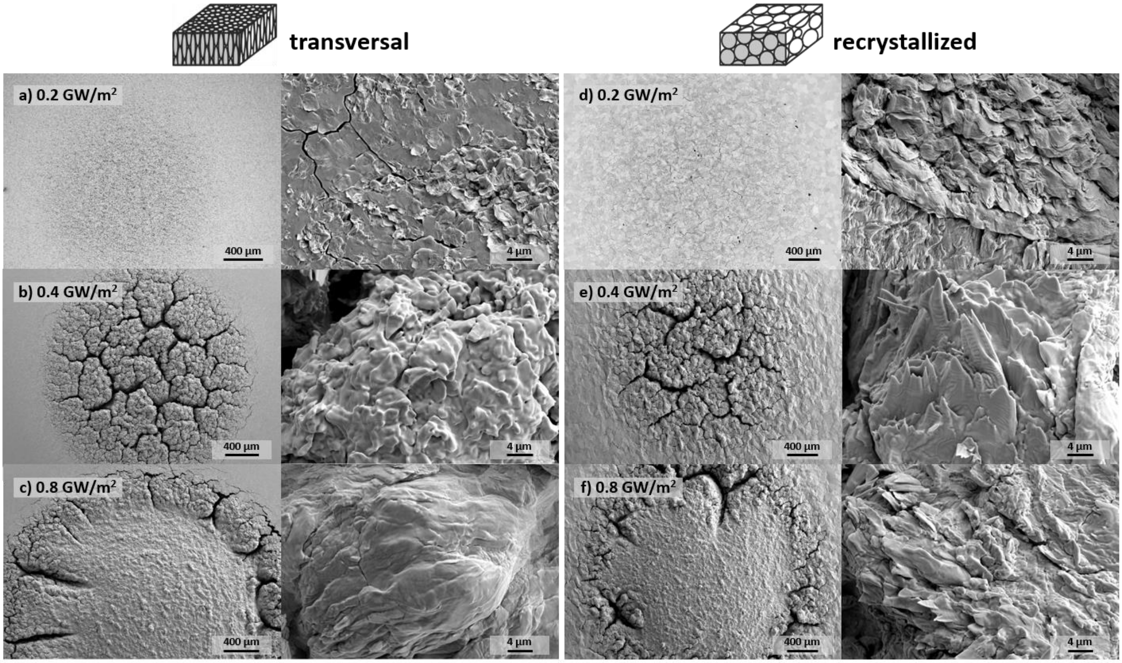

Figure 5.7. Comparison of surface modification and damage of T and R samples after 10^5 0.5 ms laser pulses with a frequency of 10 Hz and an absorbed power density of 0.2, 0.4 and 0.8 GWm^{-2}, at 700 °C base temperature.

In order to investigate the effects of these loads inside the bulk material, cross-section cuts were performed (Figure 5.8). The higher roughness of the recrystallized sample after being exposed to a P_{abs} of 0.2 GWm^{-2} that was previously observed in Figure 5.7

can also be seen here. The transversal sample exhibits an almost smooth surface, while the recrystallized one shows grains protruding from the surface. Only very small, superficial cracks of about 20 µm in depth were observed in the transversal sample, with the cracks in the recrystallized sample being several times longer, reaching up to 80 µm in depth. No recrystallization or any other such change in the grain structure was observed at this point. It can, thus, be assumed that the temperature increase at the surface was not enough for the material to show any visible sign of recrystallization. The temperature rise using a comparable power density of 0.19 GWm^{-2} was measured in the past during experiments with lower pulse numbers, obtaining a ΔT of 350 °C. This would mean, in this case, an increase of the surface temperature from the base temperature of 700 °C to just under the lower boundaries of the recrystallization temperature of tungsten of 1100 °C [82].

Significant cracking could be observed once the power density was increased to 0.4 GWm^{-2}. In both cases, cracks with a depth of 200 µm were formed, with no visible difference in the severity of the cracking. Recrystallization can already be seen at this point, up to a depth of about 200 µm below the surface in the transversal samples. Recrystallization is observed deeper into the surface in areas near the cracks, which means that they were formed early enough that the laser pulses can have an impact in the temperature of the material surrounding the cracks for long enough that the grains can recrystallize. In areas where no cracking occurs, recrystallization depth is only about 100 µm. The cracks also act as thermal barriers, which prevent heat dissipation and generate higher temperature areas, which can contribute to the recrystallization of the material. In a similar manner, grain nucleation can be observed in the recrystallized sample, up to depths comparable to those in the transversal samples. This grain nucleation, or formation of sub-grain boundaries, can be attributed to the influence of the thermal fatigue on the strain inside the grains, and is a highly dynamic process where the thermal fatigue, temperature, strain and microstructure come into play [108].

At the maximum power density, as could be seen above in Figure 5.7, no more cracking is observed in the area directly impacted by the laser beam. Two large cracks (not seen in the cross-section images) were observed, however, at the edges of the laser spot, i.e. in the transition area between the affected and unaffected area of the sample. No evidence of substantial melting at the surface can be observed, but presence of localized melting cannot be discarded. The presence of cracks only at the edges of the area where the laser hit the surface indicates a higher and more slowly dissipated temperature in the middle of the spot, which increases the ductility of the material and decreases the presence of temperature gradients. The differences in lattice size due to thermal expansion generated by these temperature gradients are one of the main causes of cracking in the material. This is why cracks are observed where the laser spot borders the material not directly affected by the laser, which is much colder than the inside of the laser spot after each laser pulse.

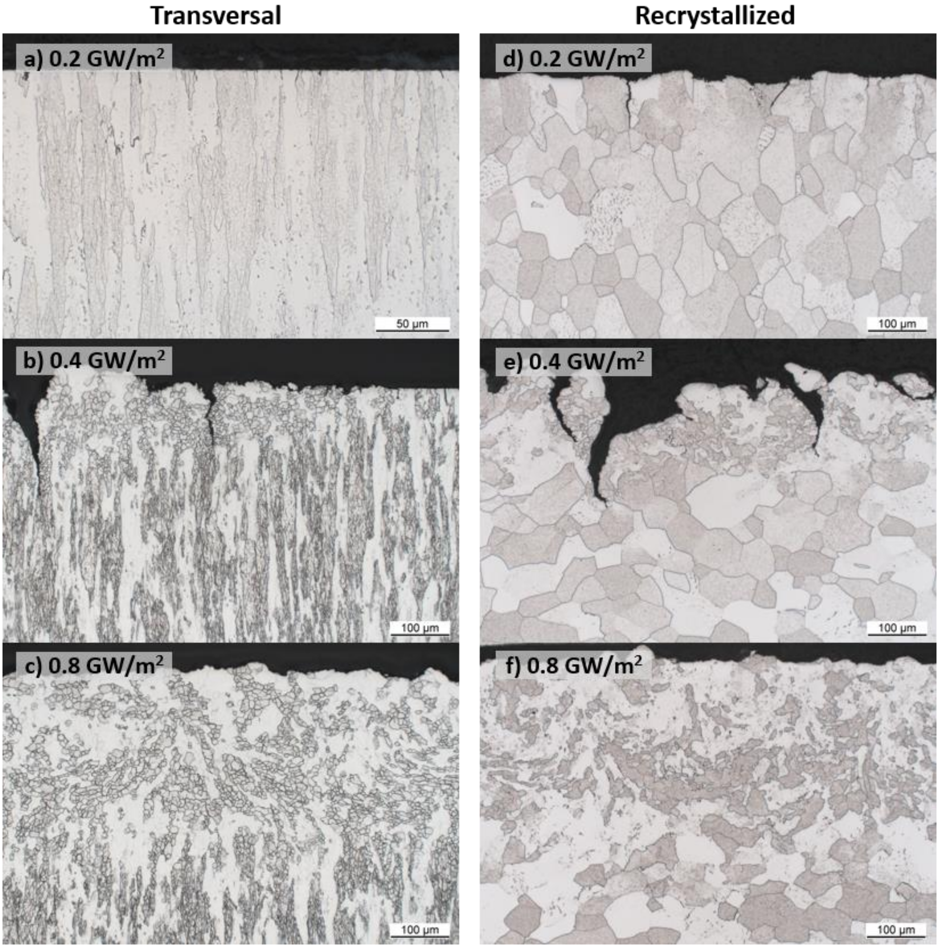

Figure 5.8. Light microscopy images of the cross-section cuts of transversal and recrystallized samples after 10^5 0.5 ms laser pulses with a frequency of 10 Hz, at 700 °C base temperature.

As previously mentioned, millions of ELMs are expected during the lifetime of the ITER divertor. This means that 10^5 thermal shocks might not reveal the full scale of the consequences of ELMs on the material and testing at even higher pulse numbers is necessary.

The effect of 10^6 thermal shock events of 0.2 GWm^{-2} can be seen in Figure 5.9. The small, isolated cracks observed in Figure 5.7 a and d have now grown into a crack network seen throughout the damaged area. The cracks observed are considerably narrower, about 20 µm, than those observed for the tests with 10^5 0.4 GWm^{-2} pulses (up to ~ 100 µm) and would most probably not be critical for the functioning of the divertor. This means that the material, whether it is transversal or recrystallized, could resist an even larger number of thermal shocks in the lower range of energy release by ELMs. The cracks, of up to about 100 µm in width on the surface, observed after only 10^5 pulses with 0.4 and 0.8 GWm^{-2} might be more problematic, although the full extent that this would affect the functioning of a reactor is not clear.

It is evidenced by these results that the power density deposited by ELMs in the material will be highly influential on the damage it will undergo, much more so than the number of ELMs. An increase by a factor of 2 in power density generated much wider and deeper cracks than an increase by a full order of magnitude in the amount of thermal shocks. This phenomenon has been recognized previously and is one of the basis upon which an ELM mitigation system is being developed, ELM pacing in particular. To reduce the damage in the ITER divertor, ELMs with a lower energy but a higher frequency can be triggered by techniques such as the insertion of small fuel pellets into the plasma. This techniques have not yet been fully developed, but it is expected for ITER to make use of such techniques, making these results even more relevant for the reactor [109–113].

The shark tooth-like microstructure can be seen as well after the high pulse number tests. These structures now seem to be ubiquitous, whereas in the previous experiments with lower pulse numbers they were only sparsely present. Also contrasting with the previous results is the fact that this sharp-edged microstructure was observed in both, transversal and recrystallized samples, whereas they could previously only be seen in the recrystallized samples. The higher damage threshold of the transversal samples might affect the formation of these structures, preventing them from forming at the lower frequency and pulse numbers. Now, with a frequency increased by a factor of 2.5 and 10 times the thermal shock events, this higher threshold might have been surpassed, allowing the formation of the structures.

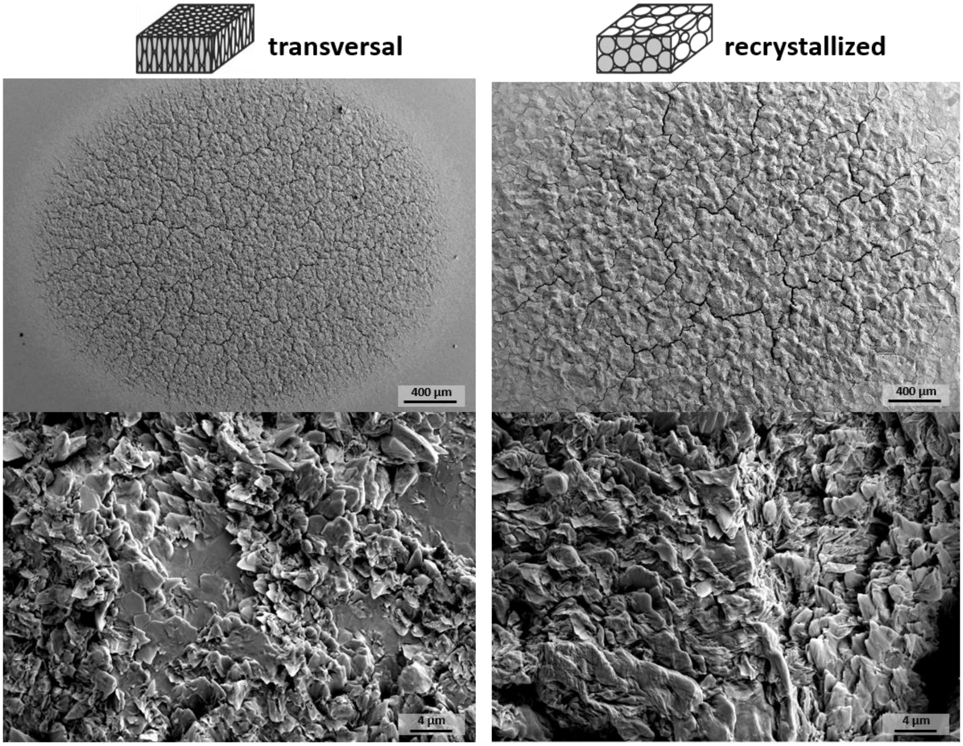

Figure 5.9. SEM micrographs of transversal and recrystallized samples after 10^6 0.5 ms laser pulses with a frequency of 25 Hz and an absorbed power density of 0.2 GWm^{-2}, at 700 °C base temperature.

Cross-section cuts of these samples were also performed. The damage observed below the surface was similar for both microstructures. Some slightly deeper cracks, reaching about 200 µm below the surface, can be observed in the transversal sample, against cracks about 170 µm deep in the recrystallized sample. A larger number of smaller cracks formed in the transversal sample, suggesting that after crossing the damage threshold, which is higher for transversal samples than for recrystallized ones, transversal samples are more susceptible to cracking. This difference is, however, not significant, as there is only one sample per treatment to analyze, and only a small portion of the cracks formed are observed. A statistical analysis would be necessary to determine the significance of the data, and only information about cracks in one plane of the sample was obtained. Despite the higher damage threshold, a larger number of cracks is not unexpected on transversal tungsten. Recrystallization removes dislocations, and the dislocation mechanism is one of the main mechanisms of crack initiation [114]. Crack initiation can also occur in grain boundaries, and due to its smaller grain size, transversal samples have more grain boundaries for cracks to be initiated. This has been demonstrated in tungsten of similar grade. Still, the crack depth observed is comparable to that seen in similar thermal shock tests performed at the electron beam facility JUDITH 2 [108,114].

The recrystallization depth in the transversal sample is also noteworthy. Recrystallized grains can be observed up to a depth of about 70 µm, whereas no recrystallization could be seen in the samples exposed to 10^5 pulses with the same power density. In the recrystallized sample, grain nucleation is observed, with smaller grains forming inside the larger grains near the surface. The mere number of pulses might be enough to explain these differences. The lack of evidence of recrystallization in the lower pulse number tests is then due to the fact that recrystallization depends not only on the temperature but also on the time the material remains at such temperature. The higher frequency in the higher pulse number tests could also have caused a small build-up of temperature in some near-surface areas, with not enough time between pulses for the heat to be dissipated. This causes the surface to reach higher temperatures for a longer time than the experiments at 10 Hz. The formation of smaller grains or sub-grain boundaries in the recrystallized sample is again observed in this case. This indicates the introduction of energy into the lattice from the thermal fatigue, which causes the larger grains to fragment [108].

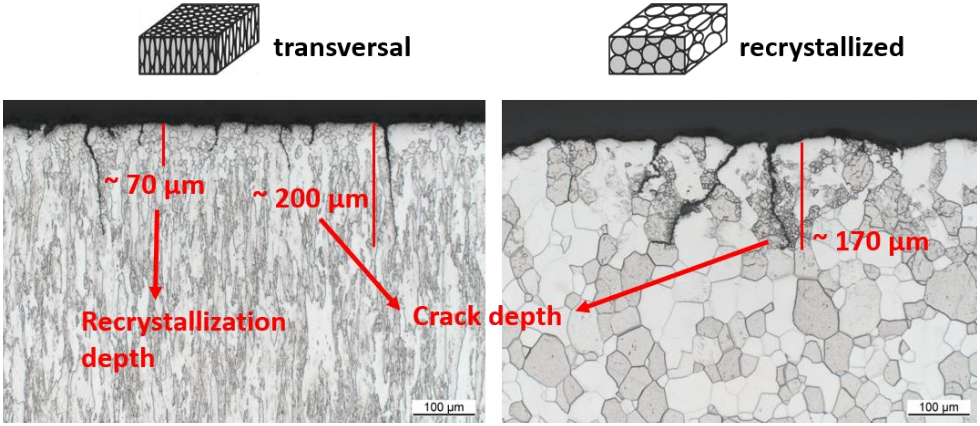

Figure 5.10. Light microscopy images of the cross-section cuts of transversal and recrystallized samples after 10^6 0.5 ms laser pulses with a frequency of 25 Hz and an absorbed power density of 0.2 GWm^{-2}, at 700 °C base temperature.

FIB cuts of selected areas inside the damaged portion of the samples exposed to 10^6 pulses were then performed (Figure 5.11). The top layer is the platinum covering used in FIB cutting to prevent artifacts caused by the ion impingement. On this scale, only very small, intergranular cracks can be found, but there is otherwise no large evidence of damage to the surface. The surface does, however, show signs of roughening when compared to the smooth original surface (shown in section 3.1, Figure 5.5). There is also no evidence of intragranular pores, bubbles or blisters even near the surface. The cross-section of some of the shark tooth-like formations are observed, particularly in the recrystallized sample, but also on a smaller scale in the transversal one. All of these formations seem to be pointing towards the same direction, despite being located in different grains with, presumably, different grain orientations. Grain orientation is probably, thus, not a defining factor in the formation of these structures. Some of the tips form intragranularly, but a tip is present at the grain boundaries of the recrystallized sample in all grains. Material seems to be diffusing and accumulating preferentially at certain points of the sample surface, eventually forming these structures. This also might indicate the plastic deformation of the grains along a certain direction. Because of the difference in the thermal expansion in the material due to differences in temperature, stresses are generated in along the temperature gradients. It is conceivable for the direction of the plastic deformation of the grains to follow the direction of the stresses. The higher density of dislocations in the transversal sample might then have a large influence on the direction of the deformation, making it more arbitrary in nature and direction, as well as preventing the formation of the sharp structures.

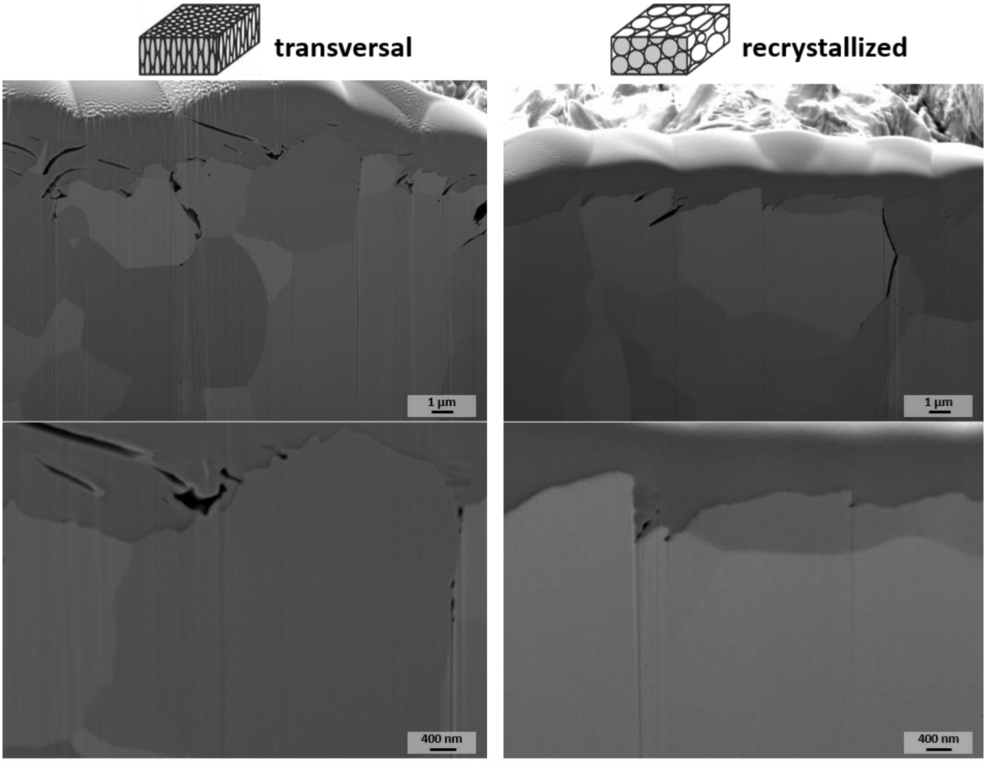

Figure 5.11. SEM micrographs of FIB cuts of transversal and recrystallized samples after 10^6 0.5 ms laser pulses with a frequency of 25 Hz and an absorbed power density of 0.2 GWm^{-2}, at 700 °C base temperature.

Both samples show a similar grain structure, even to the maximum analyzed depth of about 10 µm. This indicates a temperature increase to temperatures above the recrystallization temperature in the analyzed area. This means an increase of several hundreds of Kelvin in the surface temperature, which also propagates into the bulk of the material, causing grain growth in the originally thin, elongated grains which made them larger and isometric, just like in its recrystallized counterpart.

Arithmetical mean roughness (R_a) and maximum depth (relative to the original surface) were measured by laser profilometry for all samples and are shown in Figure 5.12. An increase in roughness can already be seen after exposure to the lowest power density, with the roughness in both samples increasing from an R_a of 0.1 µm to around 3 µm. It then increases dramatically about 5-fold when increasing the power density from 0.2 to 0.4 GWm^{-2}, with both materials showing a similar behavior. The recrystallized samples show a slightly higher roughness and maximum depth.

After further increasing the power density to 0.8 GWm^{-2}, these values were even lower than those for the samples exposed to 0.4 GWm^{-2} pulses. A smoother surface with less cracks in the center of the laser spot could already be seen in the SEM micrographs and as explained above, it might be due to a lower temperature gradient in the middle of the laser affected area, while the edges suffer from a more severe thermal fatigue. The possible localized melting and accelerated diffusion of the material to smoothen the surface is another probable explanation for this observation. For the transversal case in particular, the lower R_a value reflects how the higher surface temperature generated by the thermal shocks hinders the formation of the shark tooth-like structures and how the surface is overall smoother.

Surface roughness was approximately half for the transversal samples, both at the maximum P_{abs} and after 10^6 pulses, with a much lower maximum depth as well. The deeper valleys in the recrystallized sample could be a direct consequence of the lower hardness of the material and its larger grains obtained after the recrystallization process, which facilitate the deepening of the valleys. The additional surface smoothening effect observed in the transversal samples might be an indication of a difference in the thermal conductivity between both kinds of microstructure. Recrystallized grains have a lower defect density and a lower number of grain boundaries. Defects and pores allow for a more rapid dispersion of heat, as observed in previous studies [115]. The surface of transversal samples takes, therefore, longer to cool down, causing the surface to remain at higher temperatures for longer periods and in this way causing the smoothening of the surface. Roughness measurements were also performed in the past on samples exposed to an electron beam to simulate ELMs. With 10^5 pulses of 0.55 GWm^{-2} a roughness of 6.3 µm was obtained, which is between the results for 0.4 and 0.8 GWm^{-2}. This seems to confirm the smoothening of the surface when the power density is increased [116].

The observed differences in depth measured by laser profilometry (crack depth specifically) and by investigation of cross-section cuts are to be expected, as both techniques have their drawbacks. Laser profilometry can measure changes in the surface's z-axis, however, as it detects this with a laser emitted from above the sample, cracks that expand horizontally to the surface cannot be measured. This technique is more suitable, therefore, to measure the large valleys formed in the surface at higher power densities. In the case of cross sections, they give a full view of the sample from top to bottom, but only information about cracks present in the plane where the cut was performed can be obtained.

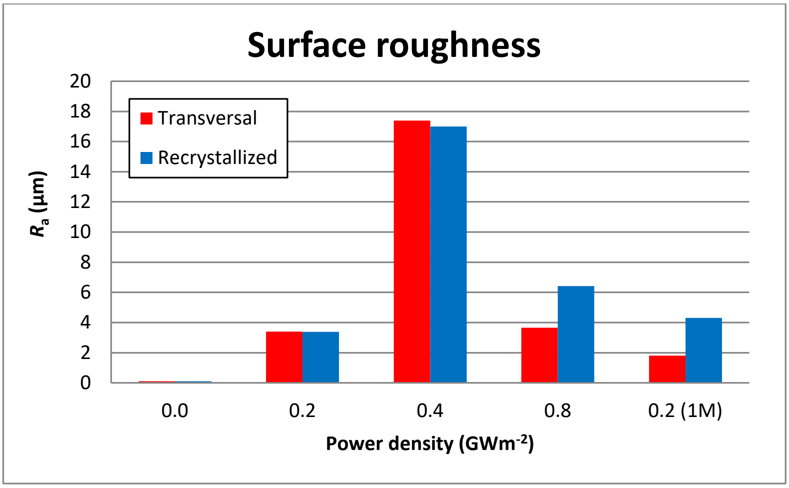

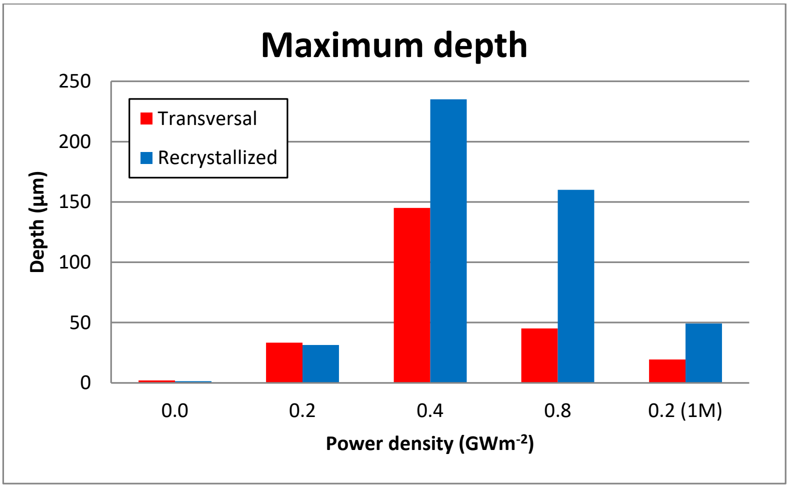

Figure 5.12. Mean arithmetic roughness and maximum depth of transversal and recrystallized samples after exposure to 10^5 or 10^6 (1M) 0.5 ms laser pulses with a frequency of 10 or 25 Hz, respectively, and varying absorbed power densities, at 700 °C base temperature. The surface analyses were done by laser profilometry.

5.2.2. Particle loads

The vertical targets in the ITER divertor are expected to reach a lifetime particle fluence in the range of 10^{30} m^{-2}. This fluence has only been reached recently in a linear plasma device [117], and never in a tokamak or any other fusion device. PSI-2 can reach plasma fluxes in the range of 10^{21} $m^{-2}s^{-1}$ and would take an impossibly long time to reach ITER fluences. With this flux, however, it is still possible to study the effects of plasma particles impinging on the surface of PFMs.

In order to study the effects of plasma particles on the surface of tungsten, an unexposed sample of transversal tungsten was compared to a sample exposed to a flux of $6.0 \cdot 10^{21}$ $m^{-2}s^{-1}$ D plasma with 6% He content at 700 °C base temperature during 192 min, amounting to a fluence of approximately $8 \cdot 10^{25}$ m^{-2}. The plasma particles had a temperature of about 35 eV, lower than the displacement energy for tungsten (60-80 eV), so no significant displacement of the atoms was expected [118]. In Figure 5.13, on the left, the surface of the unexposed sample can be observed. The surface is smooth, with some imperfections that might have remained after the polishing process, but no discernible nanostructures can be observed. On the right of Figure 5.13 is the surface of the sample exposed to plasma. The tendril-like nanostructure known as tungsten “fuzz” can be clearly observed, as well as small superficial pores. This nanostructuring was to be expected, as the base temperature and the ion temperature of the plasma are within the range where it has been observed in the past. However, no cracking or surface damage was observed [66].

As helium particles enter the tungsten surface, helium bubbles form. These bubbles grow as more helium impacts the material, and, if they are close enough to the surface, the bubbles will come to the surface and bisect it, forming pores. As these pores increase in size and number they coalesce, leaving behind this fuzzy structure, which grows in size as fluence increases (see Figure 2.10 and section 1.6) [76,119,120].

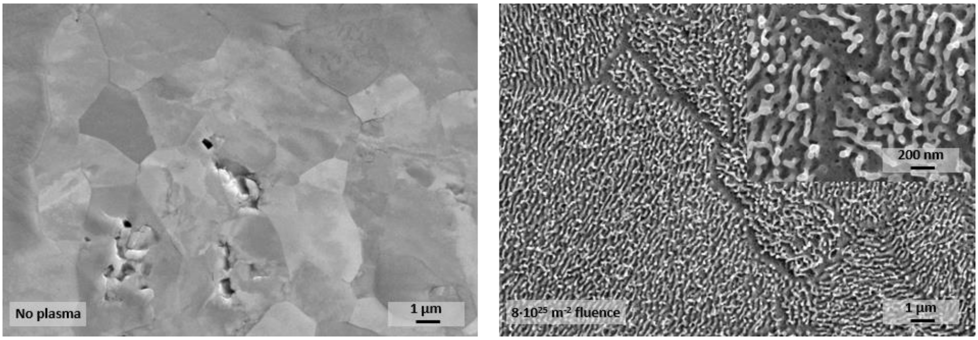

Figure 5.13. SEM micrograph of transversal tungsten samples without being exposed to plasma and after exposure to a fluence of 8 ·10^{25} m^{-2} D plasma with 6% He content at 700 °C base temperature.

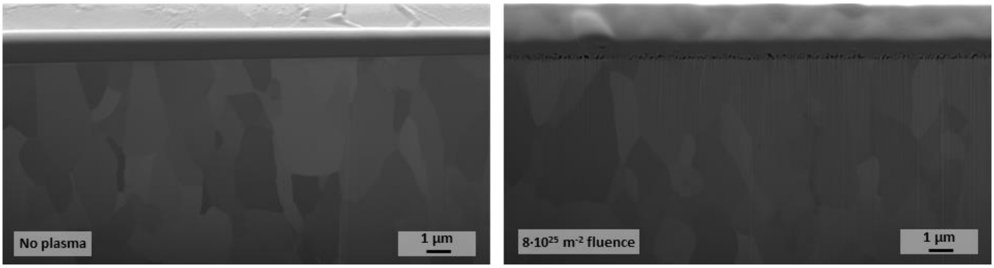

Figure 5.14. SEM micrograph of FIB cuts of transversal tungsten samples without being exposed to plasma and after exposure to a fluence of 8 ·10^{25} m^{-2} D plasma with 6% He content at 700 °C base temperature.

The FIB cuts in Figure 5.14 show that the microstructure below the surface was not observably affected by the plasma loads. The grain structure is similar between the unexposed sample and the exposed one. The tungsten fuzz can be observed on the interface between the platinum layer and the sample, but no bubble or blister formation was detected. This has been observed under similar conditions with more energetic particles 300-2000 eV [68] but also with particles within the energy range used in this work [121,122]. In all of these cases mentioned previously, however, the formation of blisters was observed at temperatures lower than the base temperature for the current experiments. Fuzz formation, such as was observed here, could be an issue for ITER, as it could make the tungsten more easily erodible, introducing a large amount of high Z material into the plasma [66].

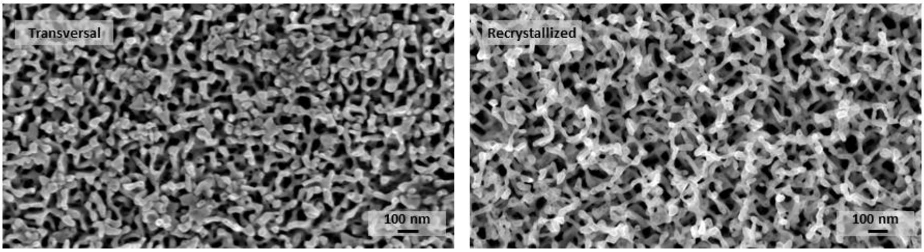

Figure 5.15. SEM micrograph of the surface of transversal and recrystallized tungsten samples after exposure to a fluence of $2 \cdot 10^{26}$ m^{-2} D plasma with 6% He content at 700 °C base temperature.

After being exposed to a total plasma fluence of $2 \cdot 10^{26}$ m^{-2}, both transversal and recrystallized samples showed a similar behavior in the formation of tungsten fuzz (Figure 5.15). At this increased fluence, the density of the nanostructure formation appears much larger than in Figure 5.13. This was expected, as formation of fuzz highly depends on the helium ion fluence [76], and here it was about 2.5 times higher than in the previously shown case. Tendrils in the hundreds of nanometers range were formed in both samples, making it impossible to observe the tungsten surface with the SEM, which was still possible in the previous test.

5.3. Synergistic effects of particle and heat loads

In sections 5.2.1 and 3.2.2, it was seen how transient heat and stationary particle loads affect tungsten in different manners. Heat loads, in this case transient thermal shocks, cause surface roughening and modification, intergranular cracking and recrystallization. A steady-state plasma load was shown to cause the formation of nanostructural tendrils (tungsten fuzz) and superficial pores. Both kinds of loads will normally be present in ITER simultaneously, and it is, therefore, the purpose of this chapter to study the synergistic effects of transient heat loads and steady-state particle loads.

In a similar fashion to the thermal shock tests, laser pulses with an absorbed power density of 0.2, 0.4 and 0.8 GW/m^2 were used to simulate the effect of ELMs on ITER's PFMs. The pulse length of 0.5 ms and base temperature of 700 °C were kept constant throughout all experiments. In this case, tests with 10^4, 10^5 and 10^6 laser pulses were performed, with a frequency of 10 and 25 Hz, respectively. The summary of heat loads applied to the samples can be seen in Table 5.2. A steady-state plasma flux was applied simultaneously to the laser pulses. Three different fluxes were applied, 3.3, 6.0 and $7.4 \cdot 10^{21}$ m^{-2}s^{-1}. Due to time restriction at the device, the full range of tests shown in Table 5.2 was only performed with the 3.3 m^{-2}s^{-1} flux. A medium flux of 6.0 m^{-2}s^{-1} was applied only to transversal samples, while the highest flux of 7.4 m^{-2}s^{-1} was applied to both, recrystallized and transversal samples, in both cases performing only the tests with 10^5 laser pulses.

For this reason, the results of all the tests with a flux of 3.3 m^{-2}s^{-1} will be shown first, to analyze the effects of the different thermal shock regimes with a constant plasma flux. The tests with the different plasma regimes can then be compared while maintaining the thermal shock parameters. All results and parameter variations can then be compared and analyzed. Afterwards, the changes in the physical properties of the material caused by the synergistic loads will be analyzed more specifically using X-ray diffraction to analyze residual stresses in the surface of the samples and nanoindentation to determine the change in hardness in the recrystallized sample exposed to the highest loads.

Table 5.2. Summary of the thermal shock treatments applied to tungsten samples along D/He(6%) steady-state plasma loads. One sample of each microstructure, transversal and recrystallized, per treatment was tested. Each laser pulse had a duration of 0.5 ms and samples were kept at a 700 °C base temperature.

P_{abs} (GWm^{-2})	F_{HF} (MWm^{-2}s$^{1/2}$)	Number of pulses	Frequency (Hz)
0.2	4.5	10^4	10
		10^5	10
		10^6	25
0.4	9	10^4	10
		10^5	10
0.8	18	10^4	10
		10^5	10

5.3.1. Effects of the variation of the thermal loads

5.3.1.1. Tests with 10.000 laser pulses

The tests with the lowest laser pulse number, 10^4, and a flux of $3.3 \cdot 10^{21}$ $m^{-2}s^{-1}$, seen in Figure 5.16, already show signs of surface modification. Only the transversal sample exposed to a power density of 0.2 GWm^{-2} shows no visible signs of damage or surface modification. The recrystallized sample shows a slight roughening of the surface under these conditions, particularly in the grain boundaries, as well as a clear pore formation. This demonstrates already how the combined effects of both kinds of loads interact with the surface, the thermal shocks producing the surface roughening and the plasma particles causing pore formation. It also confirms that the transversal microstructure confers the material a higher damage threshold than the recrystallized microstructure [106].

At higher power densities, both kinds of microstructures show significant surface modification and roughening, but still no visible cracking. The transversal sample after exposure to 0.4 GWm^{-2} has a much smoother surface than what can be observed for laser only exposure in Figure 5.6. The recrystallized sample exposed to 0.4 GWm^{-2} shows signs of fuzz formation. This, however, is not seen at the highest power density, which is a clear sign that the surface temperature temporarily increases above 1200 °C during the laser pulses. The nanostructures are not able to form above this temperature and can indeed be reintegrated into the surface at temperatures around 1700 °C [66,78]. No nanostructure formation is observed in the transversal samples either. As in the case for the laser only tests, recrystallized samples seem more prone to forming micro- and nanostructures, whether they are tungsten fuzz or the jagged structures seen without the influence of plasma. This could possibly be attributed to differences in the dissipation of heat from the affected surface area into the bulk or due to the higher plastic deformability of recrystallized materials. It would require, however, further investigations to clearly prove whether this is the case or not, or if this trend can be seen after more samples are tested.

At 0.4 GWm^{-2} and 0.8 GWm^{-2} pore formation is increased and some larger pores start to form. None of the smaller structures observed in the purely thermal shock tests (Figure 5.6 and Figure 5.7) were observed in either of these cases, also indicating that plasma loads hinder their formation [78].

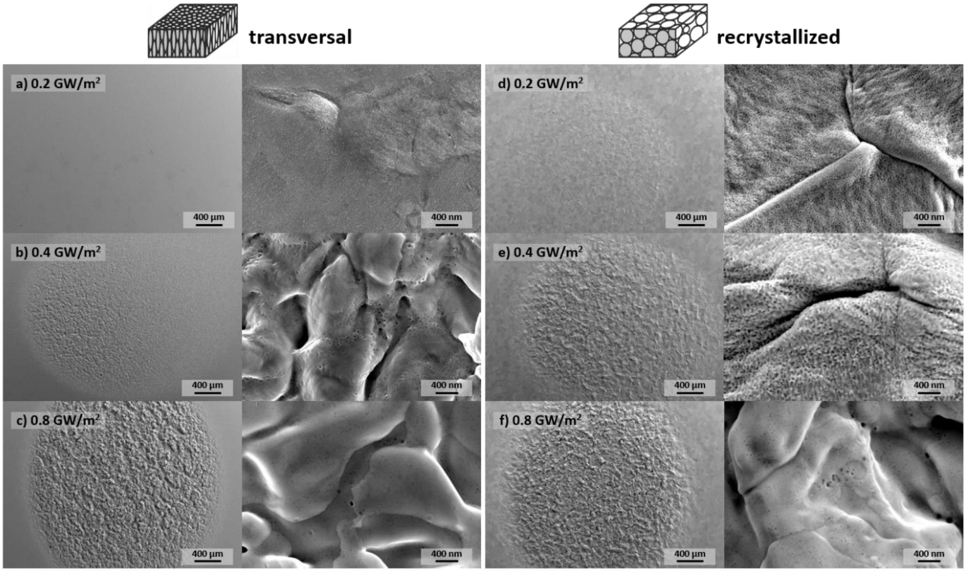

Figure 5.16. Comparison of surface modification and damage of T and R samples after 10^4 0.5 ms laser pulses with a frequency of 10 Hz and an absorbed power density of 0.2, 0.4 and 0.8 GWm^{-2}, at 700 °C base temperature, and a simultaneous steady-state D/He(6%) plasma flux of $3.3 \cdot 10^{21}$ m^{-2}s^{-1} and a total plasma fluence of $4 \cdot 10^{24}$ m^{-2}.

The cross-section cuts of these samples were analyzed and can be seen in Figure 5.17. At the lowest power density, just as in the SEM images, the transversal sample shows no sign of damage or surface roughening, while a slight roughening can be observed in the recrystallized one. Aside from the roughening, there are no evident microstructural changes present.

This trend is kept on the samples exposed to 0.4 GWm^{-2}. The transversal sample shows only a very slight roughening and no sign of recrystallization at this scale. The roughening in the surface of the recrystallized sample is now more evident, with some small peaks forming on the surface. Additionally, some smaller grains can be seen near the surface, showing evidence of grain nucleation.

The microstructural change and surface roughening are increased after exposure to 0.8 GWm^{-2}. Surface roughening severely increased in both samples. The transversal sample displays signs of recrystallization up to a depth of about 80 µm. In the recrystallized case, the formation of smaller grains is observed significantly deeper into the sample, at around 150 µm below the surface.

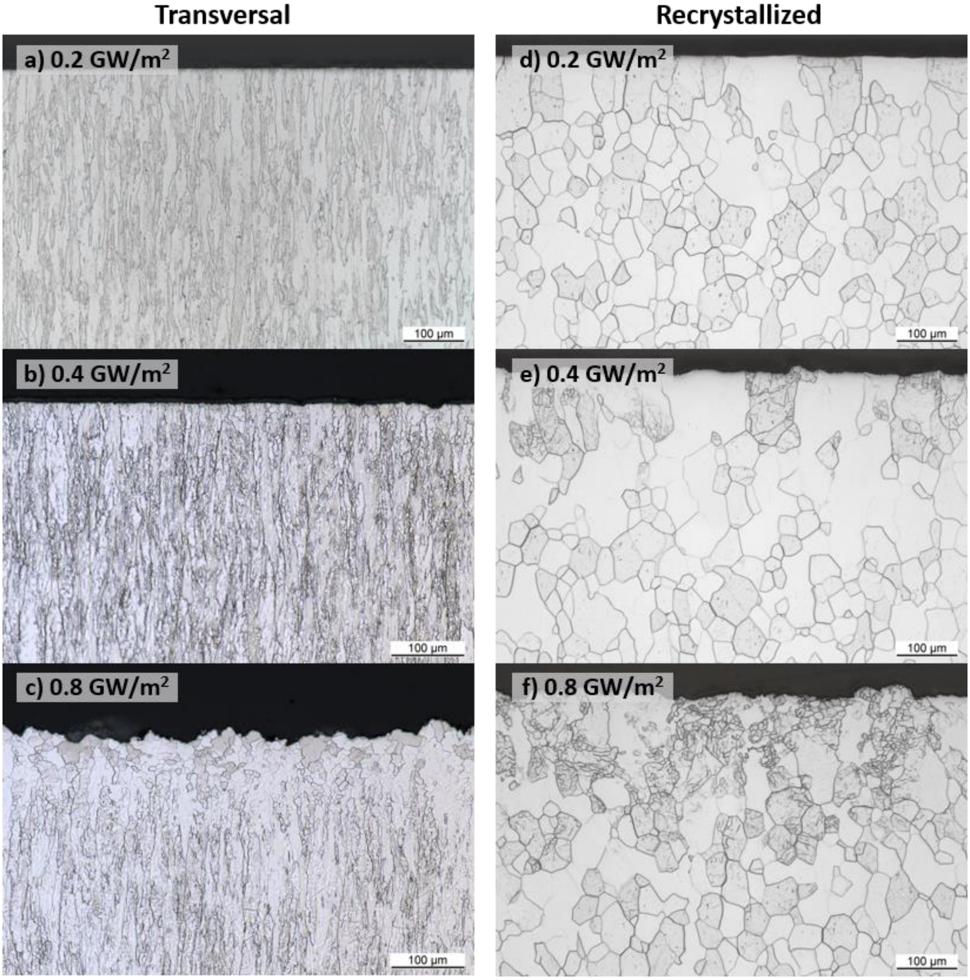

Figure 5.17. Cross-section cuts of samples after 10^4 0.5 ms laser pulses with a frequency of 10 Hz and an absorbed power density of 0.2, 0.4 and 0.8 GWm^{-2}, at 700 °C base temperature, and a simultaneous steady-state D/He(6%) plasma flux of $3.3 \cdot 10^{21}$ $m^{-2}s^{-1}$ and a total plasma fluence of $4 \cdot 10^{24}$ m^{-2}.

5.3.1.2. Tests with 100.000 laser pulses

The amount of laser pulses was then increased by an order of magnitude, to 10^5, while maintaining a flux of $3.3 \cdot 10^{21}$ $m^{-2}s^{-1}$. The frequency was kept at 10 Hz, which means the total fluence also increased by an order of magnitude, to $4 \cdot 10^{25}$ m^{-2}. SEM micrographs of the surface of the samples can be seen in Figure 5.18. After exposure to thermal shocks of 0.2 GWm^{-2}, the same trend as in the 10^4 pulse tests can be observed. In this case, the transversal sample does show signs of surface roughening, but it is less visible than for the recrystallized sample. A detail to note is that there is an artifact on the image for the recrystallized sample, seen as darker grains. These could not be observed in any close-ups of the surface of the sample and are assumed to have no relevant physical significance. Additionally, nanostructural tungsten fuzz can be clearly seen in both samples. This phenomenon is not apparent in Figure 5.16, but the formation of these tendrils can be seen in the small pores observed in the surface.

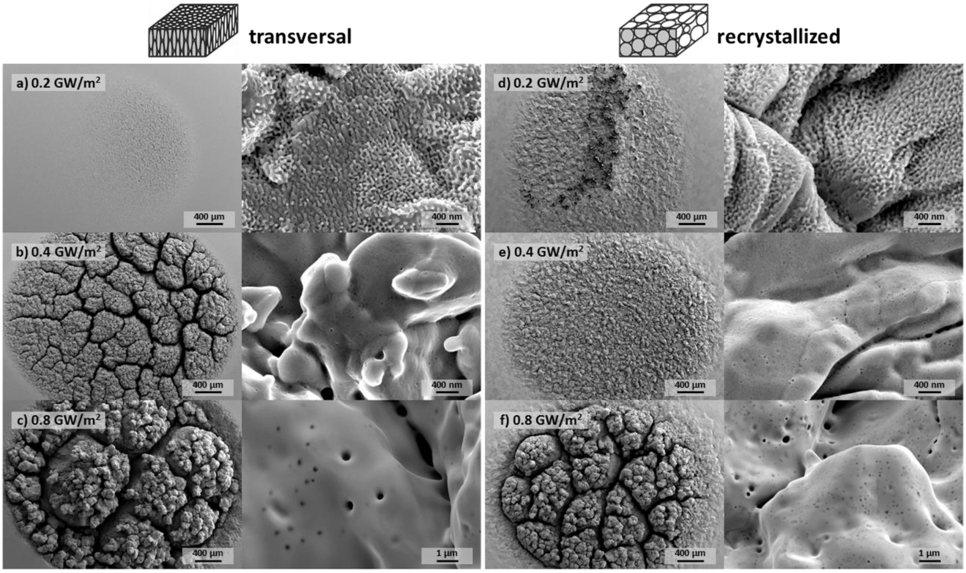

Figure 5.18. Comparison of surface modification and damage of T and R samples after 10^5 0.5 ms laser pulses with a frequency of 10 Hz and an absorbed power density of 0.2, 0.4 and 0.8 GWm^{-2}, at 700 °C base temperature, and a simultaneous steady-state D/He(6%) plasma flux of 3.3 ·10^{21} m^{-2}s^{-1} and a total plasma fluence of 4 ·10^{25} m^{-2}.

At higher laser power densities, all traces of tungsten fuzz formation disappear. Once again, the thermal shocks cause a momentary increase in the temperature of the tungsten surface and hinders fuzz growth [66,78]. The presence of tungsten fuzz in the recrystallized sample with 10^4 pulses might indicate a local zone with lower temperature. The laser heating, despite its square profile, will dissipate differently depending on the position within the sample and the surrounding temperature gradient and microstructure, particularly when surface roughening, cracking and recrystallization have taken place, modifying the original smooth surface. Surface morphology is especially relevant because the laser impacts the surface at an angle of

38°, and some areas might be shadowed from a direct impact of the laser beam. This might cause some areas to reach temperatures that impede fuzz growth and others where it does grow. Uneven tungsten fuzz growth has been observed in past experiments under similar conditions [76].

After the tests with 0.4 GWm^{-2} power density, with and without plasma, a smoother surface is obtained in the nanoscale. This could be an indication that both kinds of structures are formed and/or hindered by the same processes. Furthermore, the shark tooth-shaped nanostructure is not formed in any of the samples exposed to plasma particles. This could be caused by several reasons. The addition of plasma loading on the surface sample might locally increase the surface temperature in areas where thermal barriers are present such as happens when these structures start to form. This local temperature increase might enough to prevent the development of these formations. The presence of particle impingement has also been found to have an effect on recrystallization temperature and could affect other material properties, although this phenomenon is still under research [117]. This might cause the surface of the sample to recrystallize and the crystals to rearrange themselves without the presence of any outside nanostructure. This would be a similar phenomenon to the halting of fuzz formation at higher temperatures. The formation of nanobubbles might also prevent heat dissipation or prevent the plastic deformation of the material in a specific direction, preventing the formation of sharp structures.

Even if fuzz is not formed, pores are still observed. Their size ranges from a few nanometers at lower power densities up to a diameter of hundreds of nanometers after exposure to the 0.8 GWm^{-2} laser pulses. This indicates that the basic process responsible for fuzz formation, namely, the formation of helium bubbles, still takes place at higher surface temperatures. However, there are competing processes that prevent the nanostructure formation from taking place. A higher temperature will increase the diffusion coefficient of atoms, accelerating the diffusion of helium into the bulk of the material and causing the helium bubbles to coalesce in order to reduce the surface tension of the bubbles. Additionally, tendrils, because of their thin, long shape, have a slower heat dispersion into the rest of the material. This will cause them to have a higher temperature than the rest of the surface, further accelerating their diffusion into the surface, or even causing them to melt back into the surface if the heat loads are high enough [123].

Evidence of local melting can, in fact, be seen in the samples exposed to 0.8 GWm^{-2} laser pulses. Figure 5.19 shows a close-up of the local melting on these samples, seen in the form of solidified tungsten droplets. Such droplets were not observed for the purely thermal loads, which indicates that the plasma loading influences their formation. The deformation of the surface due to the roughening and cracking leads to protruding sections which can act as thermal barriers and as leading edges. These sections, in a similar manner as tungsten fuzz, will have a reduced ability to disperse heat. If the dispersion of heat is slow enough that the material cannot cool down to the base temperature between thermal shock events, heat will accumulate, and temperature will increase. This can lead, in some cases, to the observed melting of the material. Another contributing factor to the melting of the material is the reduced ability of the surface of the material to disperse heat caused by the bubbles forming inside the material [106].

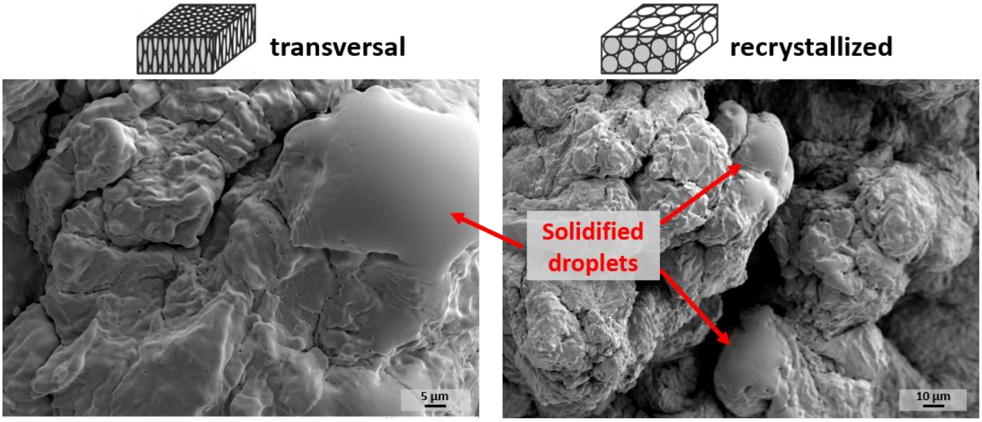

Figure 5.19. Close-up of solidified tungsten droplets on T and R samples after 10^5 0.5 ms laser pulses with a frequency of 10 Hz and an absorbed power density of 0.8 GWm^{-2}, at 700 °C base temperature, and a simultaneous steady-state D/He(6%) plasma flux of $3.3\cdot10^{21}$ m^{-2}s^{-1} and a total plasma fluence of $4\cdot10^{25}$ m^{-2}.

The tests with 0.2 GWm^{-2} laser pulses show once again how the damage threshold of transversal tungsten is higher than for recrystallized tungsten. The transversal sample shows only slight surface modification, while the recrystallized one has a much rougher and uneven surface. This trend, however, switches when 0.4 GWm^{-2} laser pulses are applied to the samples. The transversal sample formed a crack network encompassing the whole laser spot, with wide cracks of about 100 µm width or more. The thermal shocks caused the surface of the recrystallized sample to roughen further, but cracks did not form, which did occur with the purely thermal loads. Once a P_{abs} of 0.8 GWm^{-2} was applied, crack networks were present in both samples, with the transversal sample forming valleys of up to a few hundreds of micrometers, and the recrystallized one forming narrower ones. This increase in the amount and severity of cracks might be originated by the hydrogen embrittlement of the material [124]. Why a hydrogen embrittlement effect is observed for a P_{abs} of 0.8 GWm^{-2} but not for 0.4 GWm^{-2} is uncertain.

In both of the samples exposed to a P_{abs} of 0.8 GWm^{-2}, a clear swelling of the surface is observed, forming a cauliflower-shaped structure in the laser damaged area. This swelling can only be seen when applying both kinds of loads simultaneously and was not observed after the thermal load only tests. One reason why this swelling occurs might be the volume increase due to the bubble formation inside the material, which happens only when there are plasma particles entering the material and could not be detected in any of the samples exposed to thermal shocks exclusively. This bubble formation, along with the swelling, depends then not only on the fluence itself, but also on the temperature of the surface, in turn related to the power density deposited in each laser pulse. As mentioned above, this increases the diffusion of the gas into the bulk and the coalescing of smaller bubbles into larger ones, increasing the total volume of the material.

Cross-section cuts of the samples were then performed and can be seen in Figure 5.20. In the samples exposed to the lowest power density, just as can be seen above in the SEM images of the surface, the transversal sample displays a slight roughening, but there is otherwise no visible sign of damage or microstructural changes. A more visible roughening is observed in the recrystallized sample, with grain nucleation already discernible, which was not seen on the samples tested with 10^4 pulses.

These results contrast with those of the tests with purely thermal loads. When only thermal loads were applied, there were no observable signs of cracking, but the addition of the particle loads seems to accelerate microstructural changes. The stark difference in cracking behavior of both samples after the tests with 0.4 GWm^{-2} is just as evident in the cross-sections as it is in the SEM micrographs of the surface. The transversal sample displays cracks similar in shape and in depth, of about 200 µm, as the sample exposed to only laser. The recrystallized sample was resilient to cracking, with no signs of cracks and only superficial roughening being able to be seen in the cross-sections. Despite this, the microstructural changes were similar to those in the laser only tests. Recrystallization in polycrystalline materials is known to increase ductility, and this might have played a role in its tolerance to cracking, as well as the larger number of defects in the transversal sample which, as mentioned above, can increase crack formation. There might, however, be some other mechanism that takes place when plasma impacts the surface that affects the cracking of the surface only in the recrystallized samples.

Once P_{abs} was increased to 0.8 GWm^{-2}, any advantage in the resistance to cracking that the recrystallized sample might have had was overcome by the stresses caused by the increased energy being transferred into the sample. At this power density, the cracking behavior in both samples appears to be similar. Microstructural changes are observed deeper into the sample in the transversal case, though, at about 300-400 µm of depth, whereas there is not much grain nucleation in the recrystallized sample after about 200 µm below the surface. This and the apparently increased resistance to cracking of recrystallized tungsten observed with $P_{abs} = 0.4$ GWm^{-2} might be due to the lower number of defects and grain boundaries within the material, which would mean a faster heat dissipation from the surface and into the bulk, reducing the damage caused by the thermal shocks.

It is clear by comparing the results of the laser only to those of the simultaneous laser and plasma tests that plasma influences the cracking behavior of the material. It has been observed previously that samples pre-loaded with hydrogen by exposing them to hydrogen plasma are more susceptible to cracking than as-received samples. This can be explained by the trapping of hydrogen in the material. Trapping of hydrogen, and perhaps of helium as well, is enhanced by the presence of defects, such as vacancies, dislocations and grain boundaries [125]. Transversal samples have more of these defects, such as vacancies, dislocations and grain boundaries, and so can trap the gases more easily than recrystallized samples. The distortions in the lattice and in grain boundaries that are generated by the trapping of the gases cause stresses that can induce cracking, and the more gases that are trapped, the higher the stresses will be. This can explain both, the presence of cracking only on the synergistically loaded samples, and the higher cracking resistance of recrystallized samples [124].

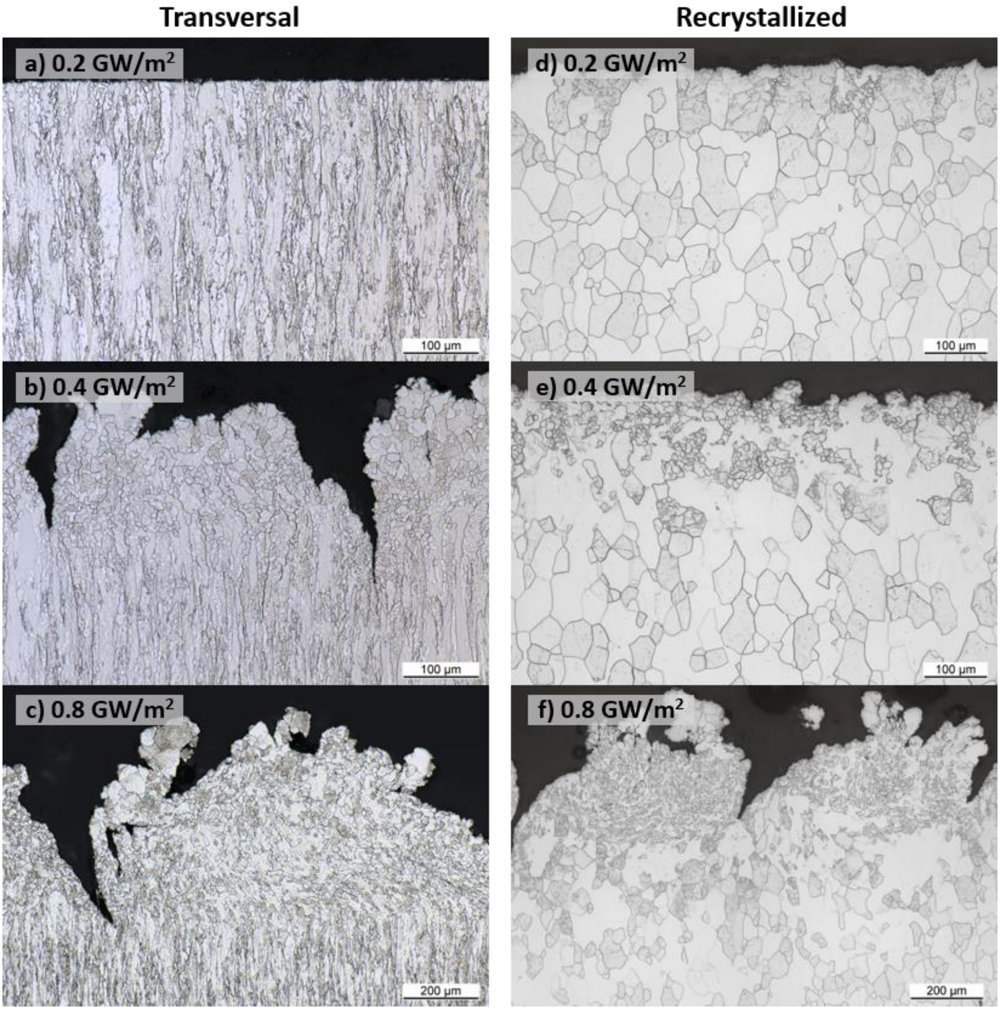

Figure 5.20. Cross-section cuts of T and R samples after 10^5 0.5 ms laser pulses with a frequency of 10 Hz and an absorbed power density of 0.2, 0.4 and 0.8 GWm^{-2}, at 700 °C base temperature, and a simultaneous steady-state D/He(6%) plasma flux of $3.3 \cdot 10^{21}$ $m^{-2}s^{-1}$ and a total plasma fluence of $4 \cdot 10^{25}$ m^{-2}.

5.3.1.3. Tests with 1.000.000 laser pulses

As mentioned in the previous sections, the amount of ELMs currently expected in ITER is in the range of 10^6 or higher, thus, 10^5 laser pulses might not reveal the full extent of changes and damage in the PFMs that can be expected in the ITER divertor. Samples were therefore exposed to a million pulses of P_{abs} = 0.2 GWm^{-2} (Figure 5.21) with a frequency of 25 Hz, keeping the same plasma conditions, resulting in a total fluence of about $2 \cdot 10^{26}$ m^{-2}. Both samples showed increased damage when compared to the laser only tests (Figure 5.9). A crack network formed throughout the laser spot in both samples. The transversal sample, however, formed wider cracks all over the spot. Isolated wider cracks formed in the recrystallized one, while the majority of the crack network is composed of narrower ones.

Nanometer sized bubbles can be seen throughout the surface. Once again, no bubbles were formed during the laser only experiments, even with such a large amount of laser pulses and an increased frequency. The pores are larger than those formed on the samples exposed to 10^5 pulses of 0.4 GWm^{-2} but still smaller than for the 0.8 GWm^{-2} tests. The increase in pore size might be the combination of multiple factors. The total time the samples were exposed to the plasma was higher, leading to an increase in the total plasma fluence. This means there were many more gas particles entering the material to form these bubbles. The increased frequency could also have led to a hotter surface, aiding in the formation of the bigger gas bubbles. Finally, the added influence of a longer exposure time, higher frequency and reduced thermal conductivity as the surface is damaged all leads to an even higher surface temperature. For a clearer answer experiments with 10^5 pulses and 25 Hz frequency would be needed, this would, however, lower the fluence, making it difficult to isolate the factors causing this effect.

In the recrystallized sample, a fuzz-like structure can be observed. It does not completely resemble the thin tendrils of fuzz. Instead, these formations appear to be the remnants of molten nanostructures. This seems to indicate the formation of fuzz or similar nanostructures, which then causes a local increase in temperature enough to cause local melting. Such molten nanostructures have been observed in previous studies after only 1000 laser pulses at higher power loads (0.76 GWm^{-2}), which suggests, once again, that peak temperature accelerates the formation of fuzz and its melting at the same time. These tests were, however, performed under pure helium plasma, and the helium flux was therefore higher, which also would accelerate fuzz formation [126].

No evidence of nanostructure formation can be observed inside the laser spot of the transversal sample, despite pore formation throughout the surface being present, which is the basic mechanism for the formation of tungsten fuzz. A larger number of defects leads to a lower thermal conductivity. These defects have also been shown to facilitate bubble formation, which, in turn, also decreases thermal conductivity. This impaired thermal conductivity would lead then to an increased surface temperature, hindering fuzz formation. Whether this is actually the case would require, however, further investigation on the surface temperature during these tests and on the initial presence of defects and its eventual influence on bubble formation. If so, this difference would probably only be relevant during the initial stages, as the surface will inevitably recrystallize, and most defects will be annealed. No evidence of larger solidified droplets was observed in either sample, indicating that the temperature remained, in general, below the melting temperature.

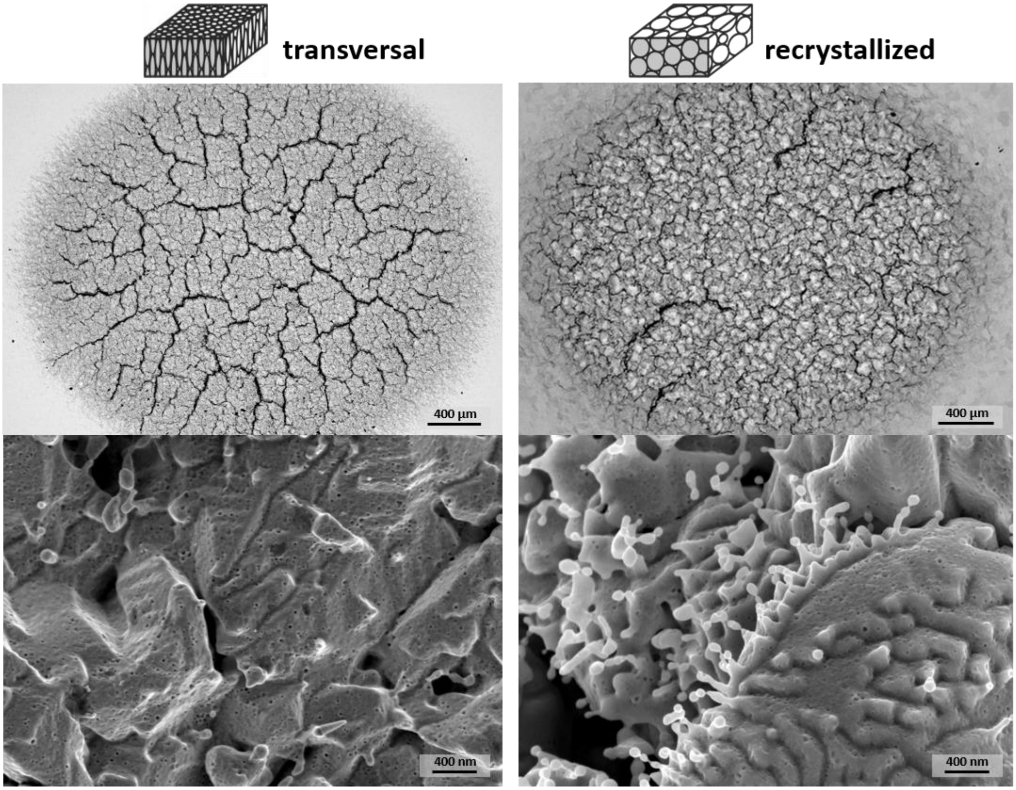

Figure 5.21. SEM micrographs of transversal and recrystallized samples after 10^6 0.5 ms laser pulses with a frequency of 25 Hz and an absorbed power density of 0.2 GWm^{-2}, at 700 °C base temperature and with a total plasma fluence of $2 \cdot 10^{26}$ m^{-2}.

Not all sections of the ITER divertor will receive the full load of ELMs and will therefore remain at lower temperatures. To analyze the effects to be expected in some of these areas, images were taken of the transition area (Figure 5.22) between the laser spot and the area unaffected by thermal shocks. It was already demonstrated that, lacking the influence of thermal shocks, no difference can be observed between the transversal and recrystallized materials (Figure 5.15). However, inside this transition area, there is still a visible difference between both microstructures. The surface of the transversal sample is rougher, with some fuzz formation, but the fuzz appears shorter and thicker, indicating some melting. In the recrystallized sample the fuzz is longer and thinner, which indicates a less impaired growth. This confirms the observation that microstructure does influence fuzz growth. This difference appears, however, only when thermal shocks are combined with plasma loads.

This does indicate that fuzz growth is to be expected in many surfaces of PFMs in the ITER divertor, except at the strike points where loads are high enough to impair its growth or melt it if it forms.

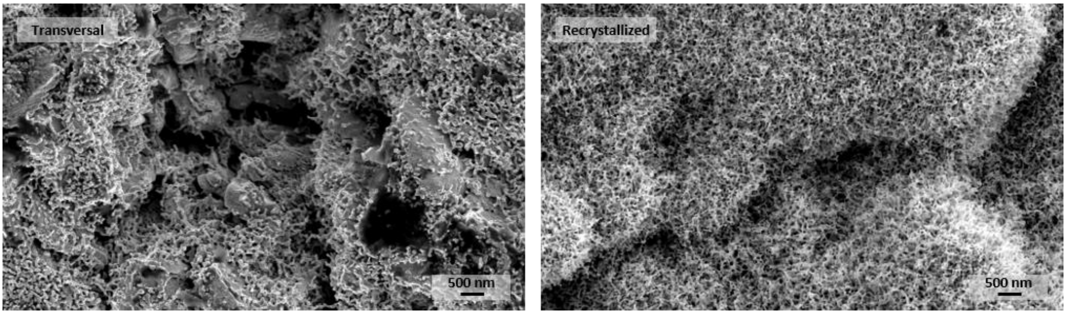

Figure 5.22. SEM micrographs of the transition area between laser spot and the unaffected area of transversal and recrystallized samples after 10^6 0.5 ms laser pulses with a frequency of 25 Hz and an absorbed power density of 0.2 GWm^{-2}, at 700 °C base temperature and with a total plasma fluence of $2 \cdot 10^{26}$ m^{-2}.

In Figure 5.23, the FIB cuts of the samples exposed to 10^6 laser pulses of 0.2 GWm^{-2} and a total fluence of $2 \cdot 10^{26}$ m^{-2} can be seen. Both samples have a similar microstructure in the area of the cut, showing that recrystallization took place near the surface. No signs of tungsten fuzz can be seen in these images, contrasting with what was observed in Figure 5.14 in the sample loaded only with plasma and where the tungsten fuzz tendrils could be seen in the interface between the platinum protective layer and the sample surface. This was expected, as the transversal sample showed no signs of fuzz growth and the recrystallized one showed only some short tendrils. A few, barely visible, bubbles can be observed in the higher magnifications. None could be observed in the FIB cuts of laser only tested samples (Figure 5.11). This demonstrates that bubbles do form even at lower power densities, but their rate of formation and growth is much lower. Bubbles several times larger are observed in the transversal sample. This might be an effect of the higher initial defect density of transversal samples, which facilitates the formation and growth of bubbles, but more a larger number of samples and cross-sections would be needed to corroborate this difference. This means, at the same time, that surface temperature does not sufficiently increase to the point where bubbles are annealed, or that there is a competing effect between the annealing of the bubbles and their formation.

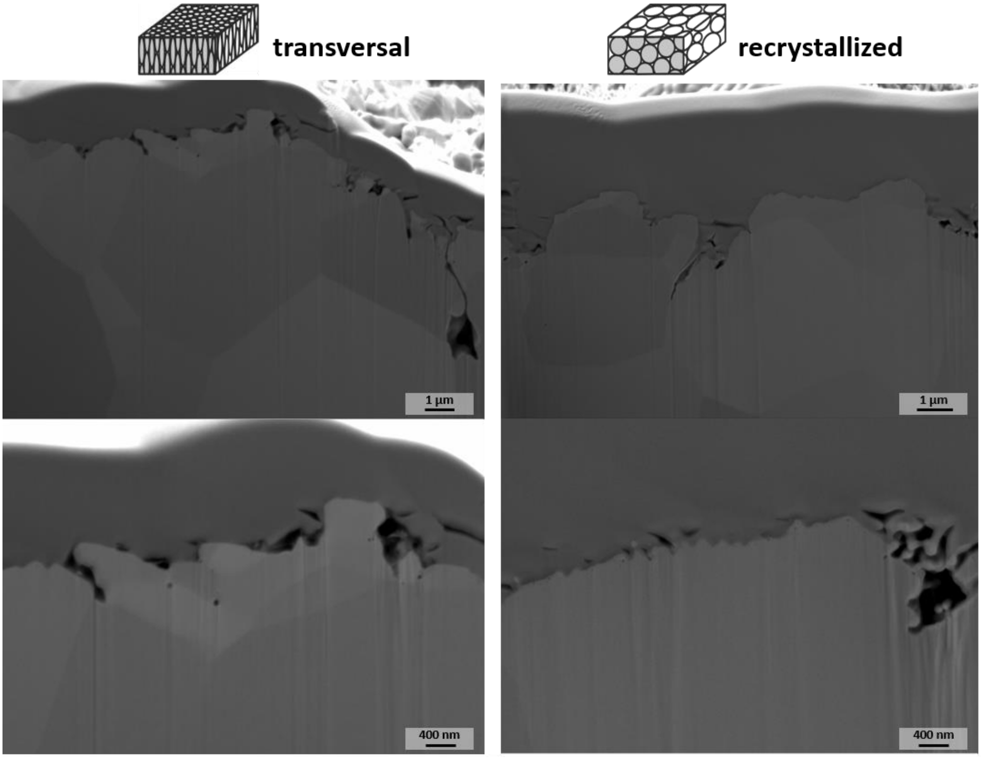

Figure 5.23. SEM micrographs of FIB cuts of transversal and recrystallized samples after 10^6 0.5 ms laser pulses with a frequency of 25 Hz and an absorbed power density of 0.2 GWm^{-2}, at 700 °C base temperature and with a total plasma fluence of $2 \cdot 10^{26}$ m^{-2}.

The cross-section cuts of these samples (Figure 5.24) show similar results to those from the laser only tests (Figure 5.10) in crack length and recrystallization depth. Crack length increased in both cases, but the number of cracks observed in the cross-sections was lower. Recrystallization depth also increased in the transversal sample, which is to be expected with the additional load of the plasma particles. The heat transmitted by the plasma might cause local increases in temperature, particularly near thermal barriers such as cracks. The original grain structure in the recrystallized sample also changed significantly. This could already be seen in the laser only sample but is much clearer in this case. Smaller grains are formed near the surface and surrounding cracks, where the material might remain at higher temperatures for longer periods of time due to the hindering of heat dissipation by cracks. The constant thermal fatigue causes stresses in the material, generates defects and introduces energy into the lattice and, therefore, inducing the formation of the smaller grains.

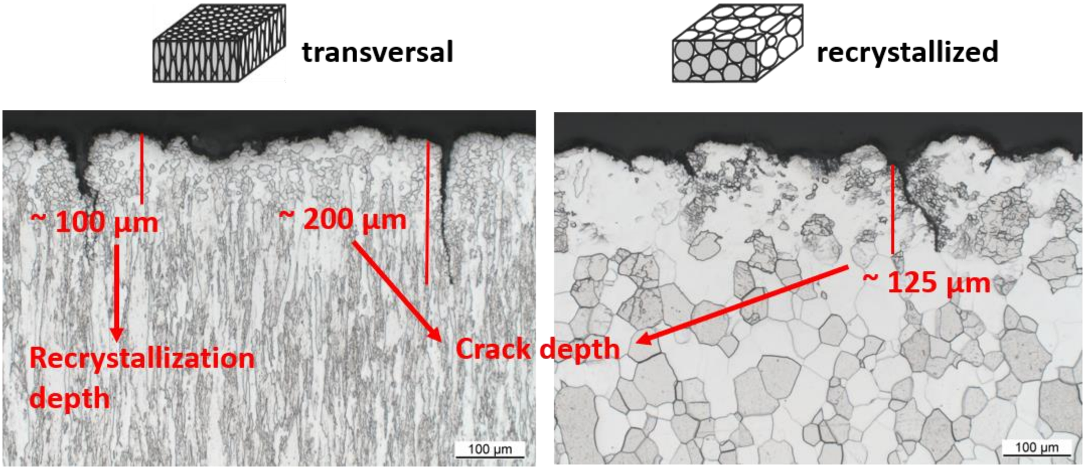

Figure 5.24. Light microscopy images of the cross-section cuts of transversal and recrystallized samples after 10^6 0.5 ms laser pulses with a frequency of 25 Hz and an absorbed power density of 0.2 GWm^{-2}, at 700 °C base temperature and with a total plasma fluence of $2 \cdot 10^{26}$ m^{-2}.

5.3.1.4. Surface modification

The measurement of surface mean roughness and maximum crack depth (Figure 5.25) shows that after exposure to 0.2 GWm^{-2} laser pulses, samples exposed to plasma and those exposed to only laser pulses show little difference. The transversal sample exposed to 10^5 pulses showed lower surface roughness and maximum crack depth, but this trend was not observed after 10^6 pulses. The difference between samples is in any case small and individual variations in the samples themselves might explain this difference, making it hard to draw conclusions in these cases. Samples exposed to plasma and 10^6 pulses do seem to have rougher surfaces and deeper cracks than those not exposed to plasma.

In any case, samples showed only small cracks that might not hinder the performance of a fusion reactor. This is an important result, methods to mitigate ELMs are being intensely researched. One of the main methods is ELM pacing via D_2 pellets or other methods. This would cause more frequent ELMs but with lower power densities. If ELMs can be successfully limited to power densities lower than 0.2 GWm^{-2}, severe damage to the PFCs might be prevented throughout the lifetime of the ITER divertor [109].

Results after thermal shocks of 0.4 and 0.8 GWm^{-2} are just as inconclusive. The recrystallized sample exposed to both plasma and 0.4 GWm^{-2} laser pulses showed a significantly lower roughness and cracking, comparable to the results of samples exposed to 0.2 GWm^{-2}. Both plasma exposed samples, after the 0.8 GWm^{-2} pulses, showed a significantly higher roughness and maximum crack depth. This seems to indicate that hydrogen embrittlement and bubble formation do have an effect, at least when higher power loads are involved, but once again, more samples should be tested to draw a definitive conclusion. The recrystallized samples also appear to form shallower valleys where cracks are formed. This, naturally, could be due to the aforementioned drawback of laser profilometry, as it can only detect changes in the surface topography in the z axis. The transversal microstructure provides a more direct route for cracks to grow vertically, promoting the formation of wider and deeper valleys, while the larger isometric grains of recrystallized samples would force cracks to take a more indirect route. This would slow cracks from reaching the cooling tubes in a full divertor component but might also facilitate the erosion of grains and hinder heat dissipation by generating heat barriers between the surface and the bulk of the PFMs which would pose an even greater risk to the performance of the reactor.

A high surface roughness is, in itself, not detrimental to the divertor. In fact, a higher roughness has been shown to lower material erosion in molybdenum in the PSI-2 and also on simulations under fusion relevant conditions [127,128]. The higher roughness promotes the redeposition of the material after being sputtered. Assuming a similar behavior on tungsten, this would prevent sputtered particles from entering the plasma, which is one of the main concerns for the successful operation of ITER.

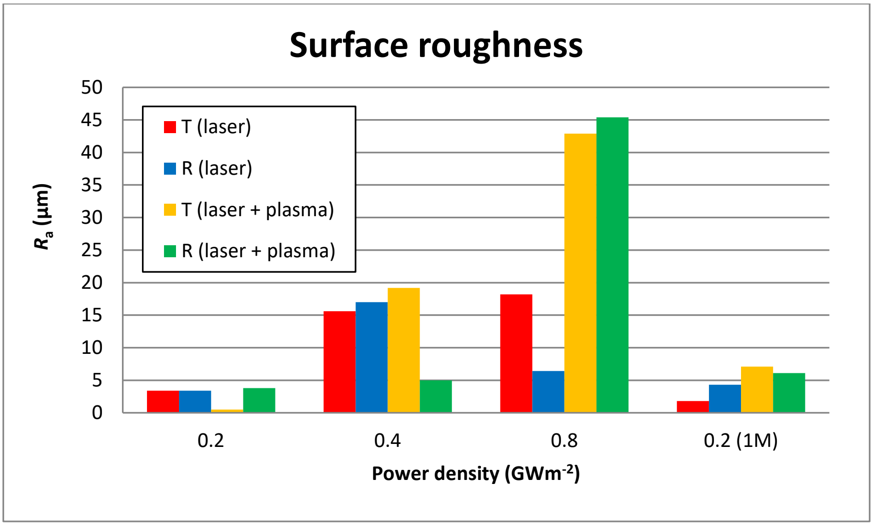

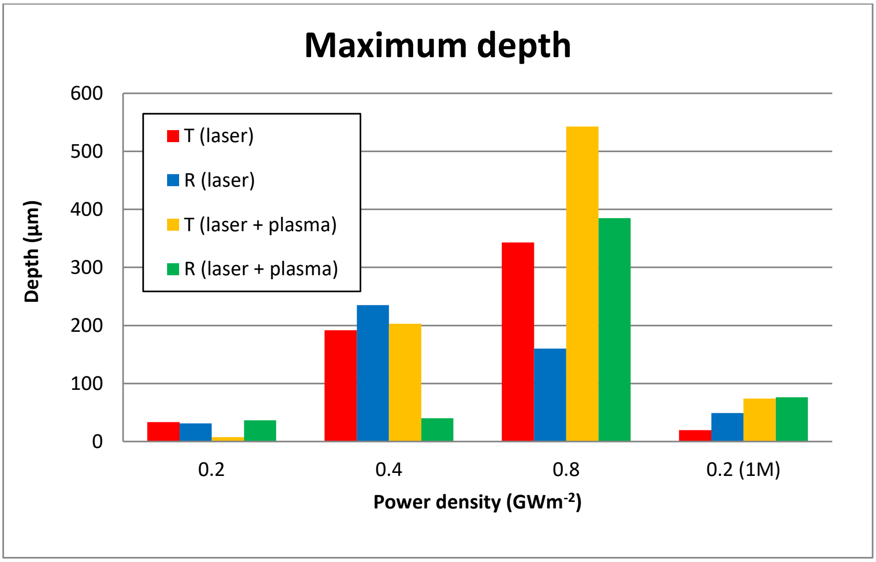

Figure 5.25. Mean arithmetic roughness and maximum depth of transversal (T) and recrystallized (R) samples after exposure to 10^5 or 10^6 (1M) 0.5 ms laser pulses with a frequency of 10 or 25 Hz, respectively, and varying absorbed power densities, at 700 °C base temperature. Samples exposed to plasma were exposed to a total plasma fluence of $4 \cdot 10^{25}$ m^{-2} and of $2 \cdot 10^{26}$ m^{-2}, respectively. The surface analyses were done by laser profilometry.

5.3.2. Effects of the variation of the plasma flux

In the previous sections, samples were all tested under the same plasma flux (3.3 - 3.8 · 10^{21} $m^{-2}s^{-1}$) and with a maximum plasma fluence of 2 · 10^{26} m^{-2}. It is projected that the ITER divertor will sustain a fluence of over 10^{30} m^{-2} during its lifetime [64], while the fluence in commercial, power-producing reactors will surpass 10^{31} per year [122]. Experiments at PSI-2 are not able to reach such high fluences in a reasonable amount of time. However, the influence of increasing the plasma fluence can be studied and insight into the effects that the elevated fluences will have on the ITER divertor can be obtained. Therefore, samples were exposed to 10^5 pulses and a plasma flux of 7.4 · 10^{21} $m^{-2}s^{-1}$, resulting in a total plasma fluence of 2 · 10^{26} m^{-2}.

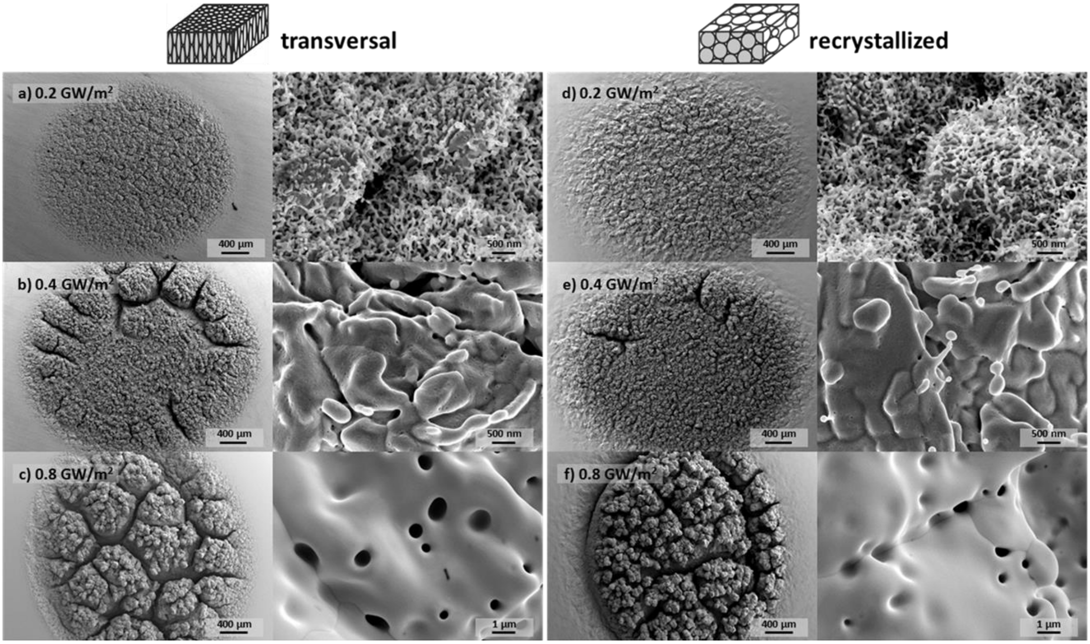

Figure 5.26. Comparison of surface modification and damage of T and R samples after 10^5 0.5 ms laser pulses with a frequency of 10 Hz and an absorbed power density of 0.2, 0.4 and 0.8 GWm^{-2}, at 700 °C base temperature, and a simultaneous steady-state D/He(6%) plasma flux of 7.4 ·10^{21} $m^{-2}s^{-1}$ and a total plasma fluence of 2 ·10^{26} m^{-2}.

SEM micrographs of samples exposed to these conditions can be observed in Figure 5.26. After exposing the samples to the lowest power density, long tungsten fuzz tendrils were formed. The fuzz formation is considerably more pronounced than for the tests at the lower plasma flux. In this case, the tendrils reach several hundreds of nanometers, while in the previous case they did not exceed 100 nm. Fuzz formation has been observed to be accelerated at logarithmic rates by increasing the ion fluence [129]. It can also be seen that the nanostructures are thinner than in the experiments with lower flux. Thinner tendrils have been observed to form as fluence increases and fuzz length increases. As explained above, fuzz forms by the formation of helium bubbles which cause swelling in the material. These bubbles are present in the surface and inside the tendrils themselves. As fluence increases, the size of the bubbles increases and the tungsten is stretched, making the walls thinner. If the bubbles grow enough to reach the surface of the tendrils, the helium can be released, leaving narrow tungsten walls behind [77,130].

As mentioned at the beginning of this section, the fluence the samples were exposed to in these experiments is only a fraction of the fluence expected in the ITER divertor. Formation of tungsten fuzz in many areas of the divertor should, thus, be expected. It is also expected for the fuzz tendrils to be much longer than in these experiments in areas not exposed to thermal loads high enough to hinder their formation [130]. The formation of these nanostructures could lead to unipolar arcing in the plasma, enhancing the erosion of the material, which would be detrimental to the fusion reaction. On the other hand, there have been indications that the presence of fuzz might be able to increase the resistance to cracking in tungsten, which could increase the lifetime of some PFCs [131].

After exposure to 0.4 GWm^{-2}, as in previous cases, no more tungsten fuzz is formed. It is, thus, possible to conclude that at higher power densities, tungsten fuzz formation is not merely slowed, but stopped completely. Similar to the results seen in Figure 5.18, transversal samples were more prone to cracking than recrystallized ones, which suggests that this phenomenon is due to the characteristics of the microstructure and not an artifact of the samples.

No large crack network was observed in any of the two samples exposed to 0.4 GWm^{-2}, with an isolated network of cracks in the transversal sample and only separate cracks being formed in the recrystallized one. Cracks are seen with more prevalence in the edges of the laser spot, which could also be seen in Figure 5.7 on laser-only samples. This reinforces the idea that cracks start in the edges of the area affected directly by the thermal shocks, where there is a greater temperature gradient and, therefore, greater compressive stresses generated by the expansion of the hot material and the constrain imposed by the colder material outside of the laser spot.

After exposure to the highest power density, an arborescent, cauliflower-shaped structure, such as the one seen after the tests with the lower plasma flux, is observed. A crack network is also formed, with deep and wide valleys. Superficially, the transversal sample looks similar to the one exposed to the lower plasma flux, but the recrystallized sample formed a more evident separation between the laser spot and the surrounding material, forming what seems like a crevasse between both sections of the sample.

The most evident difference between the samples exposed to different plasma regimes is that the ones with the highest fluence present much larger pores in the surface, with pores measuring almost 1 µm in this case. A direct comparison between the pores formed in both samples can be observed in Figure 5.28. The higher the fluence, the higher the number of hydrogen and helium particles coming into contact with the surface of the material. This leads to more particles being absorbed by the material to form bubbles, which can then coalesce into larger ones. The difference in fluence was about 2.2:1, but the bubbles were many times larger, suggesting that bubble size does not increase linearly with fluence, but much faster. More data points are, however, necessary to establish an exact trend.

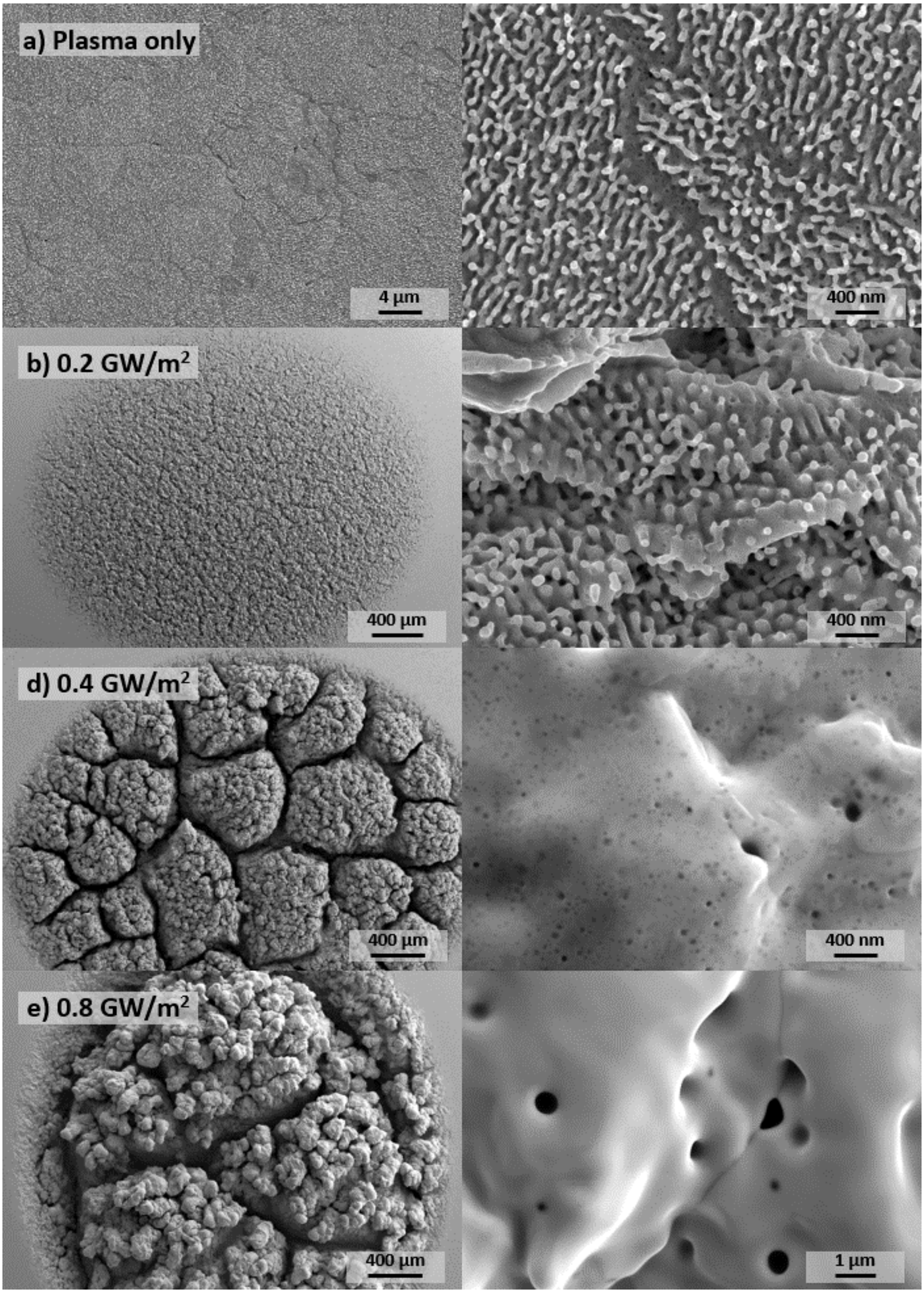

Figure 5.27. Comparison of surface modification and damage of transversal samples after 10^5 0.5 ms laser pulses with a frequency of 10 Hz and an absorbed power density of 0.2, 0.4 and 0.8 GWm^{-2}, at 700-900 °C base temperature, and a simultaneous steady-state D/He(6%) plasma flux of $6.0 \cdot 10^{21}$ m^{-2}s^{-1}.

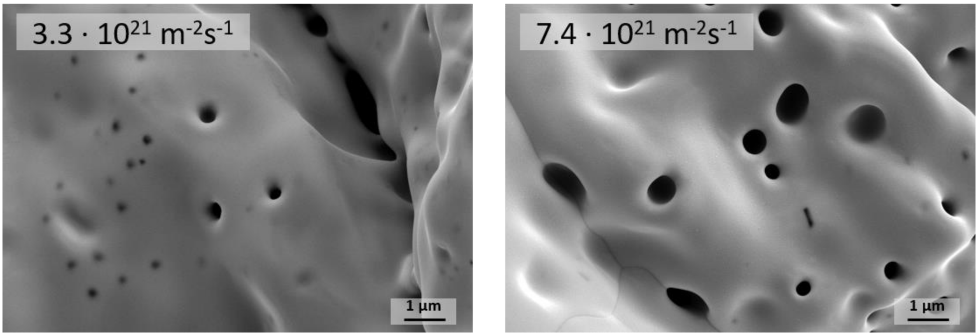

Figure 5.28. Bubble size comparison in transversal samples exposed to different plasma fluxes with a simultaneous exposure to 10^5 0.5 ms laser pulses with a frequency of 10 Hz and an absorbed power density of 0.8 GWm^{-2}.

The first tests performed at the beginning of this project were done with only transversal samples and a plasma flux of $6.0 \cdot 10^{21}$ m^{-2}s^{-1}. Temperature control was problematic during these first tests, with the sample exposed to 0.2 GWm^{-2} reaching 800 °C base temperature and the one exposed to 0.8 GWm^{-2} reaching up to 900 °C. This does not allow for a precise comparison with previously shown samples, but the results can still provide some insight into the behavior of tungsten and are depicted in Figure 5.27. The sample exposed to plasma only is also included in the image for ease of comparison with the results in the following section. A better temperature control was achieved by a more careful regulation of the heating elements and by using a holder with better heat dissipation capabilities for the tests where a higher P_{abs} was required.

The behavior observed is comparable to the one seen in Figure 5.18 and Figure 5.26. Without any thermal shocks, no visible damage occurred, but the formation of tungsten fuzz is evident. At the lowest power density, surface modification was more significant than for the experiments with the lower plasma flux, but no cracks are observed as seen with the highest flux experiments, despite the higher base temperature. This confirms the influence of plasma on surface modification and cracking, probably due to the effect of hydrogen embrittlement.

The experiment with 0.4 GWm^{-2} can be more accurately compared to the experiments with lower and higher plasma flux as only in this case was the base temperature kept at approximately 700 °C. The sample shows an extensive crack network such as the one observed with the lower plasma flux. At the highest power density, extensive cracking and evidence of localized melting can be observed, in a similar way as in previous results. The elevated base temperature did not cause any evident differences in the damage suffered by the sample. The size of the superficial pores also increased in comparison to the samples exposed to a lower plasma flux but did not reach the size of those exposed to the higher flux.

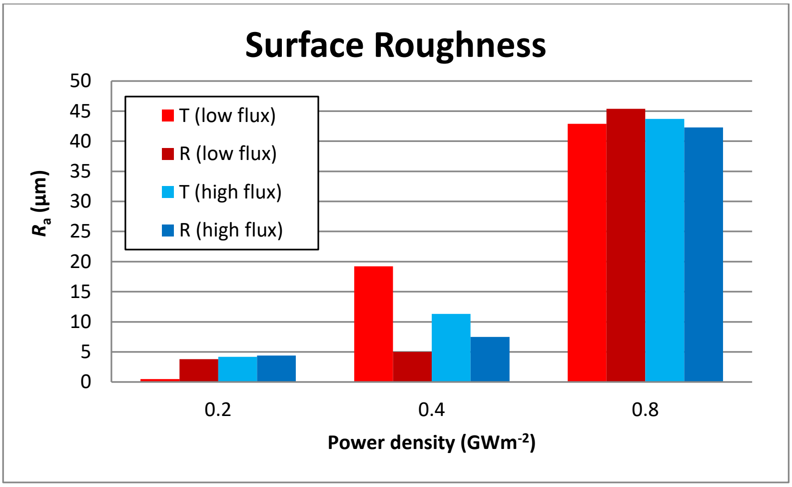

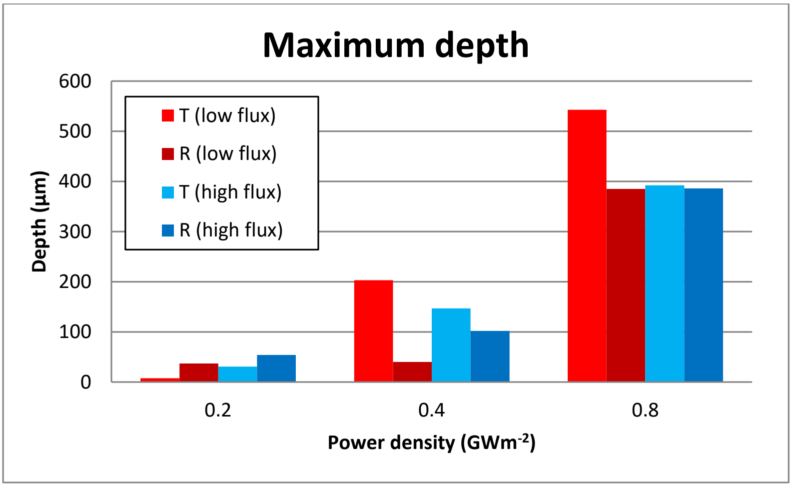

Figure 5.29. Mean arithmetic roughness and maximum depth of transversal and recrystallized samples after exposure to 10^5 0.5 ms laser pulses with a frequency of 10 Hz and varying absorbed power densities, at 700 °C base temperature. Samples were simultaneously exposed to a steady-state D/He(6%) plasma flux of $3.3 \cdot 10^{21}$ m^{-2}s^{-1} and a total plasma fluence of $4 \cdot 10^{25}$ m^{-2} (low flux) or a plasma flux of $7.4 \cdot 10^{21}$ m^{-2}s^{-1} and a total plasma fluence of $2 \cdot 10^{26}$ m^{-2} (high flux). The surface analyses were done by laser profilometry.

The mean arithmetic roughness and maximum depth (relative to the original surface) of the samples exposed to both, lower and higher fluxes, can be observed in Figure 5.29. After exposure to the lowest power density, the results seem to be very similar between the samples exposed to the different plasma fluxes. Only the transversal samples exposed to a lower flux showed a significantly lower surface roughness and maximum depth. After exposure to 0.4 GWm^{-2}, the trend is the opposite and only the transversal sample exposed to a lower flux showed a higher roughness and depth. In both cases, it would be impossible to affirm this is a significant result. After exposure to the maximum power density, however, surface roughness was very similar, and only the same sample as before showed a different behavior in its maximum depth. This indicates that at higher power loads, the effect of the thermal shocks and the recrystallization due to the high temperatures reached by the material in its surface counteract any initial differences in the behavior of the material initially caused by the different microstructures. At the same time, the variation of the plasma flux seems to have had little to no effect on the surface roughness and maximum depth reached.

To further investigate the effects of varying the plasma flux, a 2D line profile was obtained from the laser profilometer measurements. This allows the determination of the presence of possible effects on the samples, such as the swelling of the material. The 2D line profiles of samples exposed to 10^5 laser pulses with $P_{\mathrm{abs}} = 0.8$ GWm^{-2} and no plasma (Figure 5.30), low flux (Figure 5.31) and high flux (Figure 5.32) are presented for this purpose. The approximate original surface is illustrated with a red line. The original surface might appear slanted in the line profiles due to several reasons. The samples might have been cut slightly slanted during the EDM cutting process from the original material or the polishing of the samples might have produced a slanted surface. Additionally, during exposition in the PSI-2, parts of the graphite used on the sample holder remains attached to the back of the sample and this could affect the laser profilometry measurements. Lastly, the areas of the sample where the line profiles cut off might have still been affected by the thermal shocks, modifying their height in the line profiles. This might have had a small effect on the line profiles themselves, but not on the R_a measurements.

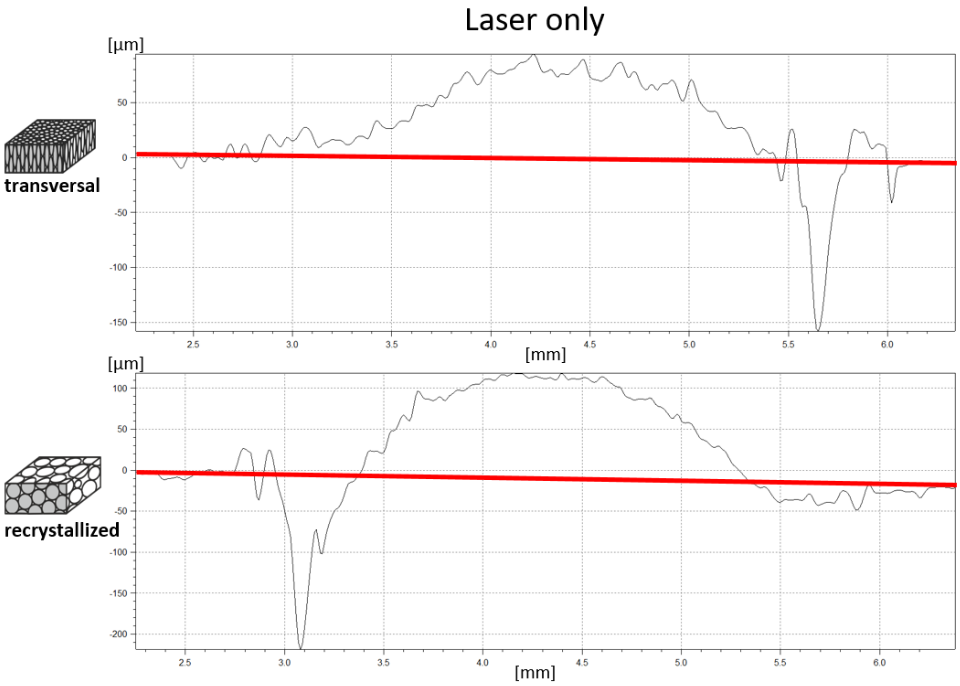

Figure 5.30. 2D line profiles obtained by laser profilometry of the samples exposed to 10^5 laser pulses with 0.8 GWm^{-2} and no plasma.

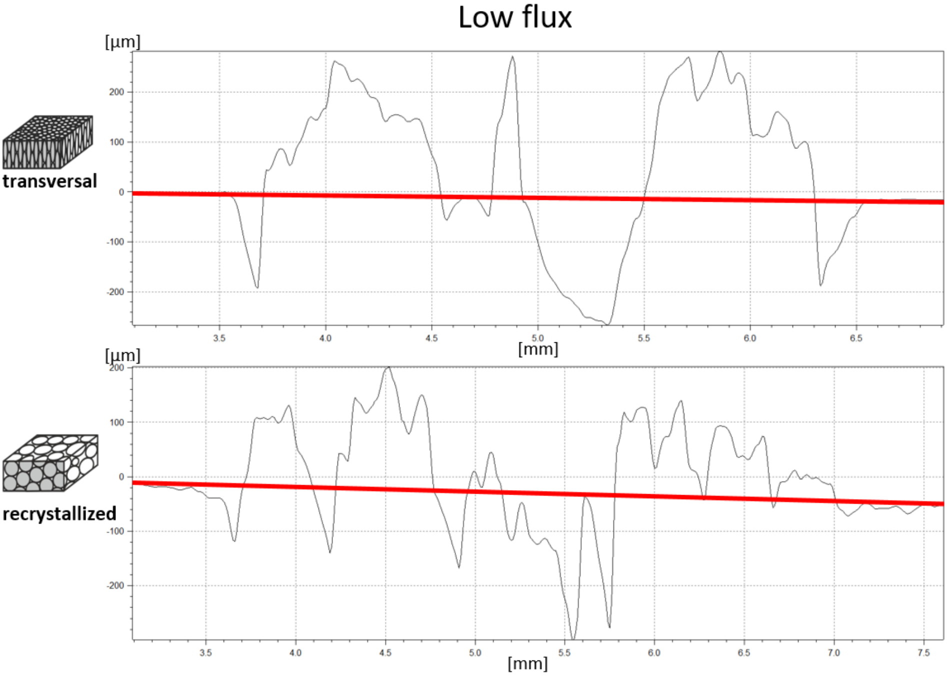

Figure 5.31. 2D line profiles obtained by laser profilometry of the samples exposed to 10^5 laser pulses with 0.8 GWm^{-2} and a simultaneous steady-state D/He(6%) plasma flux of 3.3 ·10^{21} m^{-2}s^{-1}.

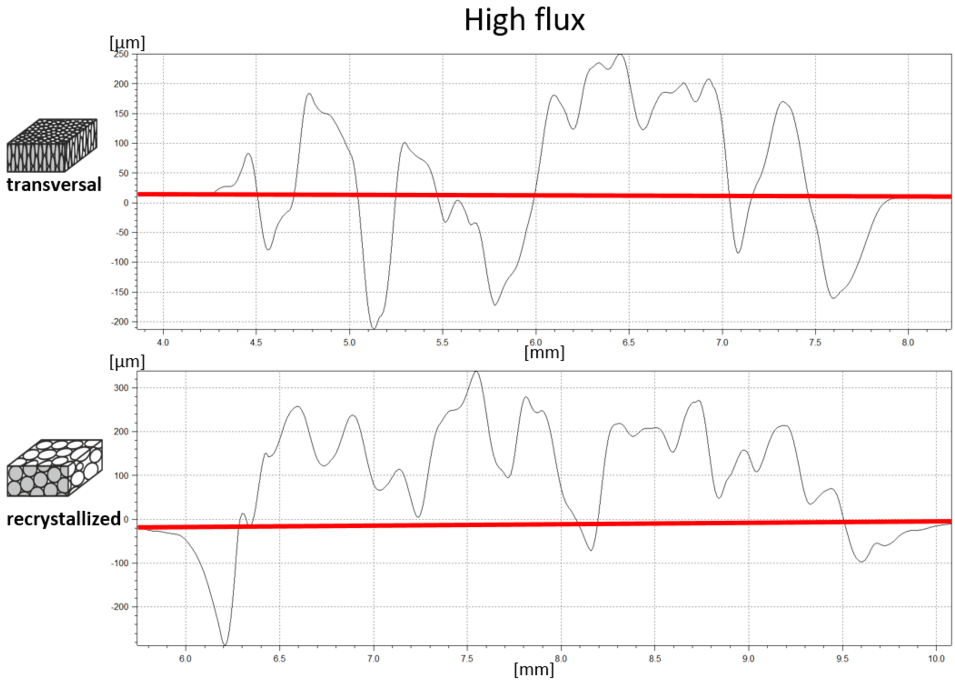

Figure 5.32. 2D line profiles obtained by laser profilometry of the samples exposed to 10^5 laser pulses with 0.8 GWm^{-2} and a simultaneous steady-state D/He(6%) plasma flux of 7.4 ·10^{21} m^{-2}s^{-1}.

In Figure 5.30, just as in the SEM images of the samples exposed only to thermal shocks, very few cracks can be identified. In these cases, only one big crack can be seen in each of the line profiles, with a large protuberance of material in the center, with a rugged surface, but no cracks visible. This bump observed is probably a product of the plastic deformation generated by the rapid heating and expansion which occurs during the laser pulses, expansion which is prevented by the material present around the laser spot, leaving as only possibility the upward movement of the material [50].

Aside from the increased cracking observed in the samples when plasma irradiation is combined with thermal shocks, which has been discussed in previous sections, it can also be observed on the line profiles that there is an increased deformation of the surface of the samples. The bulging of the laser only samples reaches about 100 µm above the original surface in the center of the dome formed in the middle of the laser spot. After applying the combined loads, the material protrudes more than 300 µm with several sharp peaks and valleys being formed. This indicates that the plastic deformation suffered by the samples due to the rapid heating from the laser pulses is more severe than in the previous cases without plasma. This can be a direct effect of the additional heat loads on the surface from the plasma irradiation. Surface temperature can indeed have a large effect on the elevation of the surface as has been observed in electron beam experiments without any plasma, where higher thermal loads indeed increased the deformation, but this effect was also observed by increasing the base temperature [132]. This means that the increased temperature facilitates the deformation of the material. Whether plasma particles themselves have an effect on this phenomenon could not be proven, as no significant difference was observed after increasing the plasma flux. However, surface protrusions are more drastic due to the bubble formation under the surface, which decrease the density of the material and cause it to swell. The presence of such protruding structures could generate very high temperature areas in the sample surface, increasing erosion of the material, making surface swelling an important issue. Thus, bubble formation is analyzed more closely in the next section.

5.3.3. Bubble formation

Bubble formation can affect the material properties in the ITER divertor and other parts of a fusion reactor, including thermal conductivity, fuel retention and cracking behavior. Thus, it is important to study bubble formation and to understand the mechanism and the causes of this phenomenon, in order to predict how this will affect the PFCs of ITER and possibly future reactors as well. Cross-section cuts are not optimal for the study of bubble formation, as the process of cutting, polishing and chemical etching of the cross-section destroys most, if not all, information about bubble formation that could have been obtained. Focused ion beam (FIB) is then necessary to study this phenomenon. Because of the amount of time required for FIB analyses, only select samples were chosen to be analyzed. The first FIB cuts on samples were performed on the first samples to be exposed in PSI-2 (Figure 5.27), in order to obtain more information on how the material's microstructure changed below the surface. The results are shown in Figure 5.33.

In the images of the FIB cuts, the uppermost layer on the surface is the protective layer, in this case composed of platinum. In the first two samples the formation of tungsten fuzz is noticeable between the platinum layer and the bulk tungsten. Very small nanometer-sized bubbles can be seen in this fuzzy layer. It is hard to identify which bubbles are actually inside the tungsten material and which are simply areas which were not completely filled by the platinum layer. Despite this, some bubbles are evidently formed in the tungsten sample very near the surface and even inside the nanotendrils, which is to be expected, as this is the mechanism of formation of these nanostructures [76,77].

After exposure to 0.4 GWm^{-2} laser pulses, larger bubbles of tens of nanometers are observed up to 100-200 nm below the sample surface, comparable to what was observed in similar studies [101]. After increasing the power density to 0.8 GWm^{-2} the bubble size also increases dramatically, reaching about 1 µm in size in some cases. These bubbles are not seen any more in areas close to the surface and only start being observed around 1-2 µm deep into the bulk. At the temperatures reached with this power density (over 2000 °C), helium particles will diffuse rapidly. Thus, they will either move deeper into the material, coalescing to form the large bubbles observed (note that very few small bubbles are observed) or move towards the surface and escape.

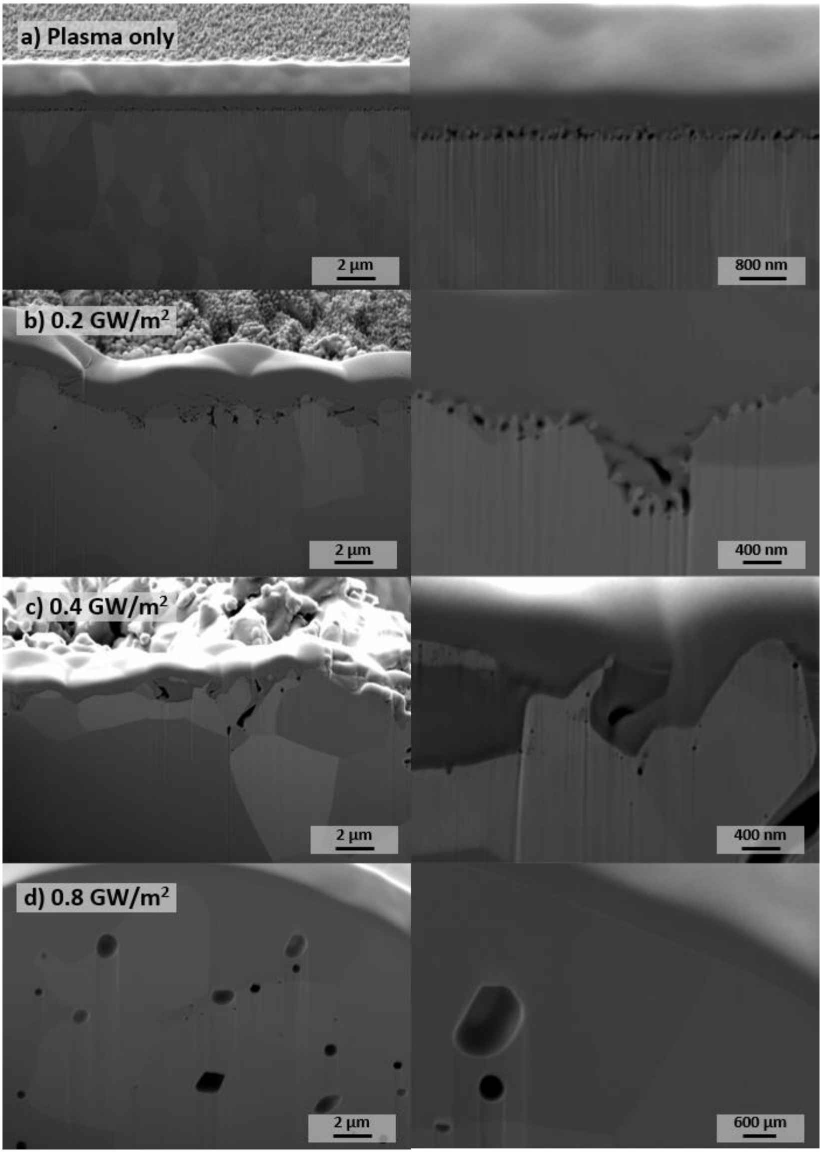

Figure 5.33. FIB cuts of transversal samples after 10^5 0.5 ms laser pulses with a frequency of 10 Hz and an absorbed power density of 0.2, 0.4 and 0.8 GWm^{-2}, at 700-900 °C base temperature, and a simultaneous steady-state D/He(6%) plasma flux of $6.0 \cdot 10^{21}$ $m^{-2}s^{-1}$.

FIB cuts of a transversal sample exposed to laser only (0.8 GWm^{-2}) under similar conditions is shown in Figure 5.34, where no sign of bubble formation can be seen. This case demonstrates how bubbles will not form when plasma loads are not present, even at the highest laser power densities.

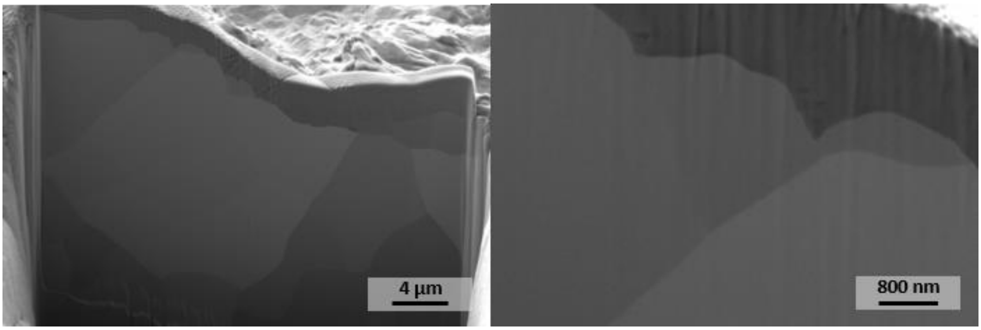

Figure 5.34. FIB cuts of transversal samples after 10^5 0.5 ms laser pulses with a frequency of 10 Hz and an absorbed power density of 0.8 GWm^{-2}, at 700 °C base temperature.

It is apparent from the results shown until now that after the simultaneous exposure to 10^5 laser pulses of 0.8 GWm^{-2} and plasma loading that a significant amount of swelling occurs in the samples. One of the reasons why this occurs is that the formation of bubbles inside the material reduces its density and, therefore, the total volume of the sample increases. To study this possibility, the FIB cut shown in Figure 5.33d was analyzed with the ImageJ Image Analysis software. By converting the image into a binary black and white image, the amount of space occupied by the bubbles in the cross-section was able to be determined. Due to the difference in brightness in different parts of the image, the analysis had to be performed only in certain areas of the image, as shown in Figure 5.35.

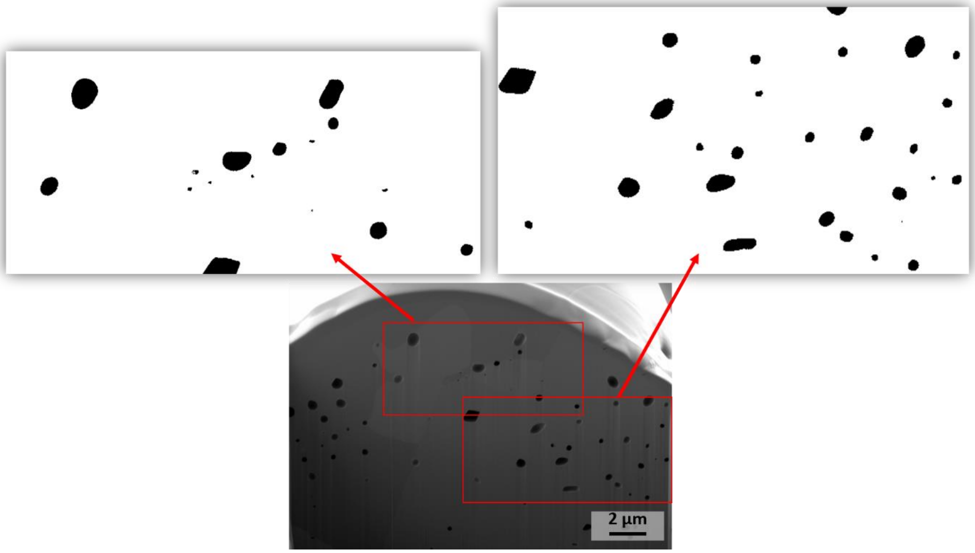

Figure 5.35. Analysis of bubble formation via ImageJ image analysis software. The marked areas show the areas that could be analyzed. The FIB cut was performed to a transversal sample exposed to 10^5 0.5 ms laser pulses with a frequency of 10 Hz and an absorbed power density of 0.8 GWm^{-2}, at 900 °C base temperature, and a simultaneous steady-state D/He(6%) plasma flux of $6.0 \cdot 10^{21}$ $m^{-2}s^{-1}$.

In both these images, a bubble coverage of approximately 3% of the total area was obtained. This is not to be taken as a precise result, as the result might not be representative of the whole sample. The FIB cut was performed in one of the solidified droplets observed in the sample surface, and the amount of volume occupied by bubbles could be very different in areas of the sample where no melting occurred, or even those shadowed by the topography of the sample from a direct exposure to the laser beam. What this analysis shows, however, is that bubbles can take up a significant amount of the volume in the near-surface area of the sample and exacerbate the swelling of the material.

Because of the already mentioned effects of these bubbles on the physical properties of tungsten, particularly on its thermal conductivity, further tests were performed to study this phenomenon. It is of particular interest to analyze the initial formation of these bubbles and which factors might affect their formation. Transversal and recrystallized samples were thus exposed to the same conditions but reducing the amount of laser pulses to 10^4 (Figure 5.36). This was only performed with a P_{abs} of 0.8 GWm^{-2}, as no large bubbles were observed in the samples exposed to lower power densities. It can be assumed that none will be observed with a lower pulse number.

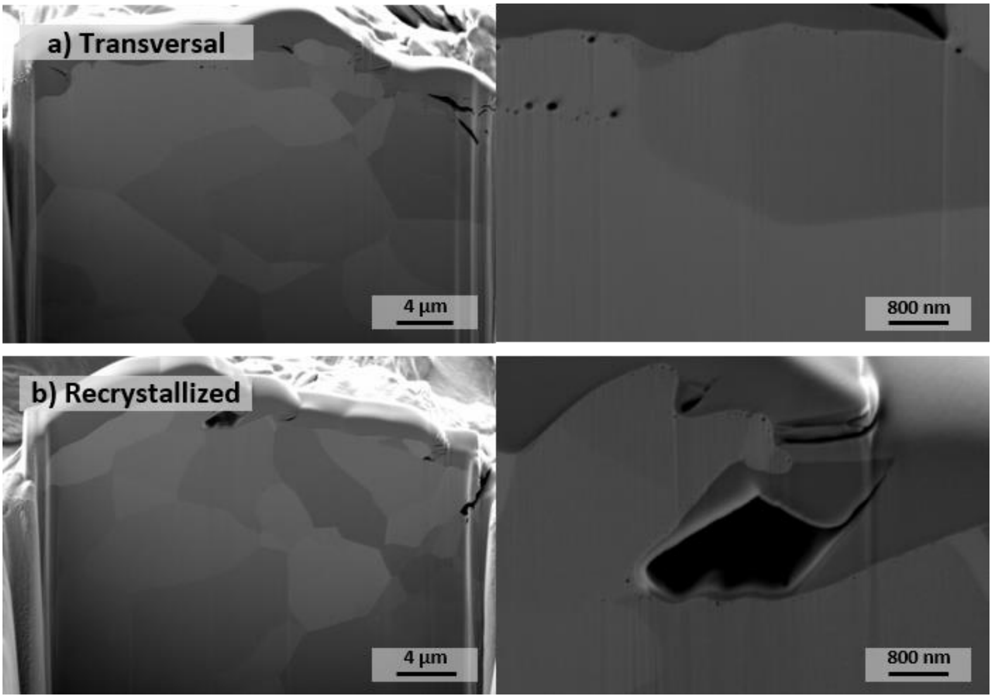

Figure 5.36. FIB cuts of transversal and recrystallized samples after 10^4 0.5 ms laser pulses with a frequency of 10 Hz and an absorbed power density of 0.8 GWm^{-2}, at 800 °C base temperature, and a simultaneous steady-state D/He(6%) plasma flux of 5.2-5.6 $\cdot 10^{21}$ $m^{-2}s^{-1}$.

From these tests, it can be concluded that bubble formation can be expected already in the early stages of the lifetime of a reactor. They start forming in the area near the surface, in the first tens of nanometers, where most of the bubbles are observed in these samples, as well as in previously shown results with lower power densities. Therefore, it can be concluded that helium plasma particles initially only penetrate the material shallowly and do not travel deep into the bulk. In order for this to happen, diffusion must take place. This is a process which is rapidly accelerated by an increase in temperature. As also mentioned in the previous sections, the trapping of helium occurs faster in defects such as vacancies, and these defects are more prevalent in transversal samples than in recrystallized ones and the consequence of this can be clearly observed in the FIB cuts. Small helium bubbles can be seen in both samples near the surface. The transversal sample, however, formed several larger bubbles in this area. Additionally, the transversal sample also formed a bubble cluster deeper into the surface, at a depth of approximately 1 µm (Figure 5.36, top right). As these clusters continue forming and the bubbles diffuse, larger bubbles will form, eventually producing a microstructure such as the one observed in Figure 5.33d. The differences in bubble formation between both kinds of samples might disappear once recrystallization and grain nucleation take place due to the high temperature in the surface of the samples. The microstructure in both samples shown seems similar, which means that the surface of the transversal sample has already undergone a recrystallization process, and both have been plastically deformed. A higher defect density in the transversal sample can still be present if the recrystallization process has not yet been completed.

5.4. Residual stresses after exposure

Residual stresses should be expected in most fabrication processes for metals and any thermomechanical treatment of a material. They can either improve or degrade the physical properties of the materials, depending on the material and the magnitude, direction and position of the residual stresses in question. This can influence such factors as the structural integrity, corrosion resistance, resistance to cracking, fatigue life and hardness of materials [133,134]. This means that knowing the residual stresses that will be present in the ITER divertor after its fabrication process is of critical importance to understand its behavior under fusion conditions. And since residual stresses can form or relax with thermal treatments, fatigue, microstructural changes, surface roughening and cracking, understanding how these stresses change as fusion relevant loads are applied to ITER grade tungsten will help shed light on the expected evolution of the material once the fusion reactor start operating.

In order to achieve this, the transversal and recrystallized tungsten samples exposed to D/He(6%) and to 10^4 and 10^5 ELM-like thermal shock events were analyzed utilizing the $\sin^2\Psi$ (see section 2.8) to determine the residual stresses in the sample surface. An example of the sample preparation is shown in Figure 5.37. The samples were covered by a copper foil except in the areas where it was desired to analyze the residual stresses. This was necessary particularly in the laser spots, as the area of measurement of the XRD device is larger than the laser spot, and the copper foil prevents the X-rays from interacting with the surrounding area of the sample, which would otherwise result in incorrect signals being taken into account. The peaks caused by the copper foil can then be omitted.

The results of the determination of residual stresses in the surface of the samples can be observed in Figure 5.38 for the samples exposed to 10^4 laser pulses and in Figure 5.39 for the samples exposed to 10^5 laser pulses. The exact values and standard deviations can be found in the appendix. The rough surface in many of the samples, however, introduces various uncertainties into the measurements, particularly in the most damaged samples. Nevertheless, the method does show a trend in the residual stresses of the samples after the different treatments, and this is what will be discussed below.

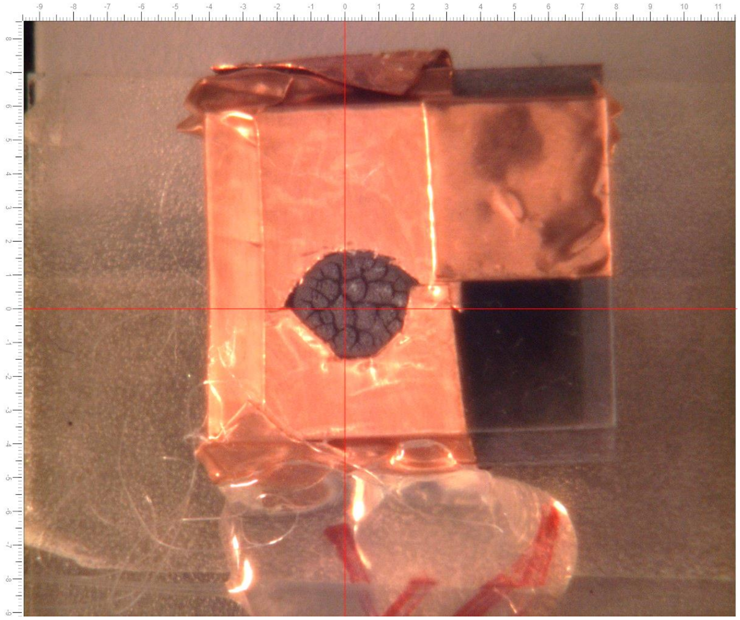

Figure 5.37. Image of a tungsten sample prepared for the XRD measurement of residual stresses. The cracked surface is the laser spot, and the blackened area was exposed to plasma loads only. The copper foil is used to isolate the desired area from its surroundings.

First, an as-received transversal sample was analyzed to determine the stresses introduced by the cutting, grinding and polishing of the samples. This is an expected effect of mechanical treatments on a material [135]. Lower, but still significant, compressive stresses are also observed in transversal samples in the sample regions affected only by plasma (steady-state D/He(6%) plasma flux of $3.3 \cdot 10^{21}$ m^{-2}s^{-1} and a total plasma fluence of $4 \cdot 10^{24}$ m^{-2}, shown in the graphs as samples exposed to 0 GWm^{-2}). It is possible that the plasma irradiation has an effect on the relaxation of the residual stresses, although it is more probable that the heating of the samples partially anneals the samples, and the stresses are relaxed. This could not be measured in the case of the recrystallized samples. The measurement of the diffraction peaks via XRD for polycrystalline samples requires a high enough number of the grains to have the required orientation to satisfy Bragg's equation and diffract the incident beam. Due to the larger size of the recrystallized grains, this condition could not always be met satisfactorily, resulting in a large spread in diffraction peak intensities and positions. This made it impossible to obtain meaningful measurements on these samples until thermal loading was applied. Nevertheless, it can be safely assumed that no significant residual stresses were present in recrystallized samples before their loading in PSI-2, as the recrystallization process entails a relaxation of any residual stresses previously present in the material. It would also not be expected that any large residual stresses would be included by the plasma loading, as it only has an effect on the surface at a very small scale. Neither is it expected for those previously existing residual stresses to have been relaxed in any significant amount by the relatively low base temperature of 700 °C, which is several hundreds of degrees lower than the recrystallization temperature of tungsten.

The recrystallized samples exposed to 10^4 laser pulses presented a considerable tensile residual stress on their surface. Since the recrystallization process relaxes any residual stresses previously present in the material, it can be assumed that these tensile stresses were generated when plasma and laser loading was applied. The fact that after exposure to 0.4 GWm^{-2} the residual stresses in the transversal sample changed from compressive to tensile means that under such conditions tensile stresses are indeed generated in the sample. 0.2 GWm^{-2} might not be enough to overcome the initial compressive stresses present in the transversal sample, but enough to generate tensile stresses in a relatively stress-free surface. Once the power density is increased, the tensile stresses caused by the localized heating of the material and subsequent fast cooling by heat conduction to the colder surroundings could overcome the compressive stresses originally present [41]. Once P_{abs} is increased to its maximum value, the residual stresses can be seen to slightly decrease. This is in part due to the cracking, which allows the material to expand and contract more freely, and due to the higher temperature obtained in the surface during the laser shots, which leads to the surface recrystallization discussed in previous sections. The formation of tensile residual stresses contradicts the findings in previous studies, which found that irradiated tungsten formed compressive and not tensile stresses, as well as recognizing the formation of a second tungsten phase (β-W). These studies were, however, done with only up to 10 plasma pulses of 3 μs, and might not represent the behavior after a longer exposure [59].

The presence of compressive residual stresses in the transversal samples can explain the larger cracking threshold of transversal samples when compared to recrystallized ones, as compressive residual stresses can hinder crack formation [133,135]. Tensile stresses, on the other hand, are undesirable in many cases including in the ITER divertor, as they facilitate cracking. The presence of these stresses might be one reason to opt for transversal samples, although, as seen in this and previous sections, in the sections of the ITER divertor exposed to the highest loads, recrystallization will quickly take place and the original stress condition of the material might not be relevant to the long-term performance of the PFCs.

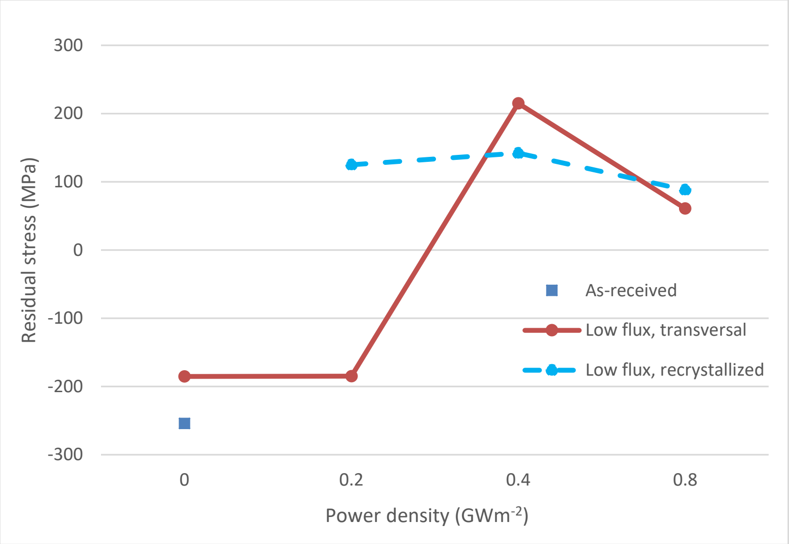

Figure 5.38. Measurement of superficial residual stresses in transversal and recrystallized tungsten samples exposed to 10^4 laser pulses with varying absorbed power densities and a steady-state plasma flux of $3.3 \cdot 10^{21}$ $m^{-2}s^{-1}$ at 700 °C base temperature. Due to the large grain size, it was not possible to measure the residual stresses in the recrystallized sample before loading.

The samples exposed to only plasma loading shown in Figure 5.39, similarly as in the ones exposed to a lower fluence in Figure 5.38, present compressive tensile stresses on their surface. The sample exposed to the lowest flux, $3.3 \cdot 10^{21}$ $m^{-2}s^{-1}$, showed no significant change compared to the previous sample exposed to the same conditions for a shorter period of time. After increasing the flux to $6.0 \cdot 10^{21}$ $m^{-2}s^{-1}$, the magnitude of the stress was reduced considerably. This points to a possible influence of the plasma itself on the surface stresses, perhaps the faster formation of nanobubbles and tungsten fuzz influences the superficial stresses, and the effect could not be observed at the lowest flux. Once thermal shocks are included, tensile stresses are once again formed. In this case, the transversal sample exposed to a low flux and low P_{abs} showed a tensile residual stress, meaning that even a low P_{abs} can have an effect on the formation of these stresses, but it requires a higher number of pulses to have an observable effect. This is why it could not be observed in the previous experiment with only 10^4 pulses.

For all the other samples, both transversal and recrystallized, exposed to 0.2 GWm^{-2} considerably lower, but still significant, compressive residual stresses were observed. This indicates that the higher plasma flux does partly aid in the relaxation of surface residual stresses. Their effect on the stress relaxation might be only indirect, in that plasma embrittles the material and this causes an increase in cracking, which in turn causes a reduction in residual stresses. This effect can be more clearly seen once the power density is increased to 0.4 Wm^{-2}. A general trend can be observed where the stresses decrease and, in most cases, it can be said that the surface is essentially stress-free.

At the maximum power density, some stresses seem to appear, both compressive and tensile, with no trend to be observed, as both compressive and tensile stresses seem to be present in different samples. This is most probably due to the highly damaged and uneven surface, which lowers the accuracy of this method. This might make it seem as if some stresses form due to the increased noise in the signal obtained in this method, even if the surfaces remain, presumably, nearly stress-free.

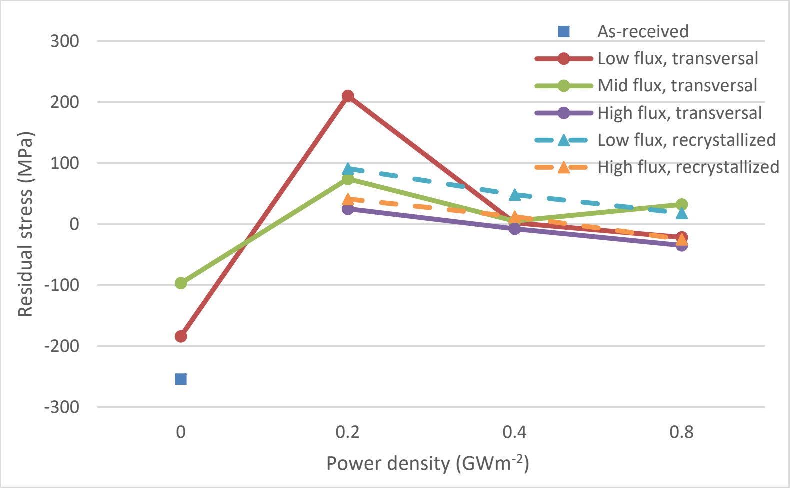

Figure 5.39. Measurement of superficial residual stresses in transversal and recrystallized tungsten samples exposed to 10^5 laser pulses and different fusion relevant conditions in PSI-2 at 700 °C base temperature.

5.5. Nanoindentation tests

In previous sections, an overview of the behavior of tungsten after exposure to fusion relevant conditions was given. This was done by analyzing the macro- and microscopic changes in the different samples after exposure to various conditions. As important as these tests are to predict the behavior and lifetime of PFCs in ITER and other fusion devices, a focus on more fundamental physical characteristics of the materials can shed some light on how the materials will behave once the reactors are working at full power. Hardness is one such physical property, which can be determined without requiring special sample geometries such as would occur in the case of other material properties, e.g.: tensile strength. Still, the cracking and formation of structures at different scales can affect the hardness measurement in a sample by methods such as indentation. To eliminate the influence of these other variables, a nanoindentation device can be utilized.

Nanoindentation is a versatile tool that can reveal how hydrogen and helium implantation and other effects of fusion relevant conditions can affect the hardness of tungsten and other PFMs. The recrystallized tungsten sample exposed to the highest power load (Figure 5.18f) was chosen for this analysis, as it was expected that it would showcase the best comparison between loaded and unloaded areas and the grains would be large enough to be discerned from each other.

The indentations were performed on the cross-section of the sample (Figure 5.20f). This was done, firstly, because nanoindentation tests require a smooth surface to be performed and the sample surface was too rough, as even a mechanically polished surface might be rough enough to cause a large scatter in the data points [136]. Mechanically polished surfaces and deformed surfaces in general also have an increased dislocation density, which has an impact on nanoindentation measurements. The cross-section was, therefore, mechanically polished and then chemically etched to obtain a surface as smooth as possible. And secondly, to analyze the hardness of the sample in relation to the depth of the indentations. This could be seen as an analysis of how deeply below the surface do the plasma loading and thermal shocks have an effect on the material properties. A view of the diamond Berkovich tip used by the device and some of the indentations performed can be seen in Figure 5.40. As it can be observed in the images, the position of each indentation can be precisely selected to be performed inside a single grain if so desired and if the force applied is low enough for indentations to fit inside the grains. For the experiments, a force of 10 mN was applied to ensure the indentations would fit inside even the smaller grains. In this way, different individual grains can be selected to determine the effect of grain orientation in the outcome of the tests. This can be done by the coupling of EBSD with the SEM, and then comparing the individual grains tested with their hardness and their grain orientation. It also allows the elimination of effects that would increase the scattering of measurement values, such as performing an indent on or near a grain boundary, or on top of a large pore. Grain boundaries in particular can have a large effect on the outcome of the tests, due to the lower atomic binding and the increased concentration of dislocations inside them [137]. Note that in Figure 5.40 some indents landed very near to each other, this is generally not desired. Performing an indentation test too closely to previous indentations will modify the results obtained due to the plastic deformation present in the surface after each test. In such cases, the result of the second test was not taken into account.

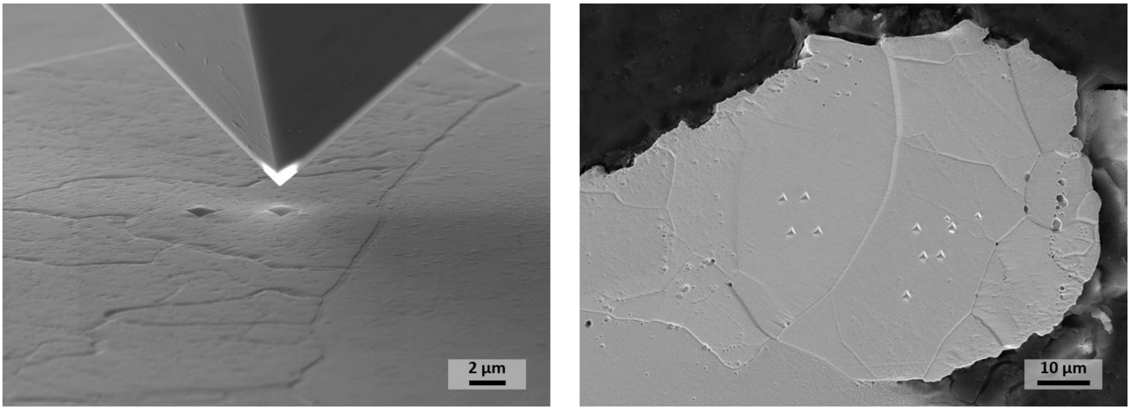

Figure 5.40. Example of the nanoindentation process of the recrystallized sample exposed to 10^5 0.5 ms laser pulses with a frequency of 10 Hz and an 0.8 GWm^{-2}, at 700 °C base temperature, and a simultaneous steady-state D/He(6%) plasma flux of $3.3 \cdot 10^{21}$ $m^{-2}s^{-1}$.

The first tests were performed on the more superficial parts of the sample, less than 50 µm from the surface (Figure 5.41, a). Some of the indents performed can be seen in Figure 5.40, right side, where signs of localized melting can be seen and there are larger, plastically deformed grains than in the loaded area deeper under the surface. This section of the sample had the highest hardness compared to other sections of the sample, 7.5 ± 0.4 GPa. In this case, an effect was observed where the first indent performed in each grain displayed the highest hardness, with a subsequent drop in hardness of up to 16% in all subsequent indents performed on the same grain. This effect was not observed in any of the other sections of the sample. This area of the sample is evidently highly plastically deformed by the large stresses it was subjected to during the exposure and part of the increase in hardness can be explained by strain hardening, which has been observed in tungsten heavy alloys used as penetrators against armor plates [138].

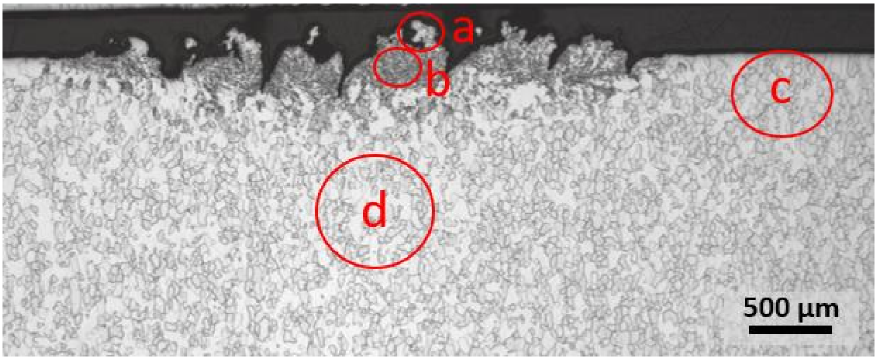

Figure 5.41. Different sections of the sample tested with the nanoindenter. a) Laser+plasma loaded (top, near the surface), b) laser+plasma loaded (middle, deeper into the surface), c) plasma-only loaded, d) not loaded (bulk).

The other sections analyzed were, firstly, the laser and plasma loaded area, deeper below the surface (Figure 5.41, b), where smaller grains product of grain nucleation can be observed. Secondly, farther below the loaded area, where no indication of microstructural change is observed and is assumed to have received no load of any kind. And, lastly, in the near-surface area outside the laser spot, thus having been affected by plasma particles but not the thermal shocks. The results of the indentations in these different sections can be observed in Figure 5.42.

As seen in the graph, the top of the loaded surface displayed an increase in hardness of about 40% compared to the unloaded parts of the sample. This result is comparable to previous similar tests performed with different techniques, which observed a 30% hardness increase after W and He ion bombardment of a tungsten sample [139]. The average hardness in the middle of the loaded area was only 7% higher than for the unloaded section. It must be mentioned, however, that the spread in this area of the sample is quite large, and the hardness had a significant, gradual decrease from the section closer to the top and the one closer to the bottom. In Table 5.3, the range of the measurements for each section, and the number of indents performed can be compared.

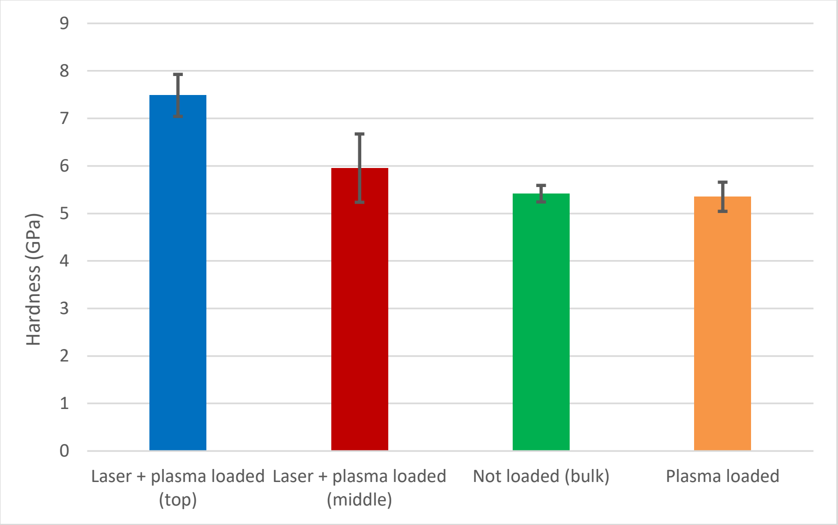

Figure 5.42. Comparison of the hardness measurements of the recrystallized sample exposed to 10^5 0.5 ms laser pulses with a frequency of 10 Hz and an 0.8 GWm^{-2}, at 700 °C base temperature, and a simultaneous steady-state D/He(6%) plasma flux of $3.3 \cdot 10^{21}$ $m^{-2}s^{-1}$. The measurements were performed with a diamond Berkovich tip and applying 10 mN of force.

Despite the lower number of tests in the areas of the sample without thermal shock loading, it can be seen that the scatter of the hardness values is very low. There is also no significant difference between the hardness in these two areas, even taking into account that one of them was exposed to plasma. This seems to indicate that plasma has no significant effect on the hardness of the material in these conditions on recrystallized tungsten. This agrees with what has been observed in previous experiments, where it was determined that hydrogen and helium irradiation increases hardness in as-received tungsten samples, but does not affect hardness in recrystallized tungsten (at comparable base temperatures to this work) [140], although these tests were performed with much higher helium ion energies (1 MeV). At lower energies of 50 keV, a significant difference in hardness could be observed also in transversal tungsten [141]. It would, therefore, be revealing to perform this test also in the transversal samples to corroborate these observations. The values obtained in this work for the grains unaffected by the laser are also very close to the values obtained for recrystallized tungsten from the same provider, without any kind of plasma or thermal load [142].

In contrast to this, in another previous work, an increase of only 5% in the hardness of tungsten was observed in samples exposed to helium plasma and helium plasma plus rhenium ion irradiation [143]. These differences are probably caused by the different conditions under which samples were exposed in these previous experiments. The hardening effect of helium plasma has been determined to be caused by the formation of nano-bubbles in the surface of the material, and the filling of already existing vacancies and of these newly-formed bubbles by helium [73]. A similar effect was also observed with pure deuterium irradiation, where the hardening effect was attributed to nanocavities formed by the plasma particles and were, presumably, filled with deuterium. This pins geometrically required dislocations caused by the formation of the cavities and hinders dislocation motion. The presence of deuterium was corroborated by NRA measurements, but whether deuterium fills these cavities or is located somewhere else is not yet proven. The lower mobility of dislocations has also been observed to be responsible for a higher hardness but also a higher yield stress on irradiated surfaces [74,144]. The hardening effect disappeared after desorption of the deuterium [74].

Table 5.3. Comparison of the hardness measurements of the recrystallized sample exposed to 10^5 0.5 ms laser pulses with a frequency of 10 Hz and an 0.8 GWm^{-2}, at 700 °C base temperature, and a simultaneous steady-state D/He(6%) plasma flux of $3.3 \cdot 10^{21}$ $m^{-2}s^{-1}$. The measurements were performed with a diamond Berkovich tip and applying 10 mN of force.

Section	Average hardness (GPa)	SD (GPa)	Min. Value (GPa)	Max. Value (GPa)	Number of indents
Loaded (top)	7.5	0.4	7.00	8.18	9
Loaded (middle)	6.0	0.7	4.95	7.79	36
Not loaded (below)	5.4	0.2	5.20	5.58	6
Not loaded (side)	5.4	0.3	5.01	5.66	4

As mentioned above, the crystal orientation of the individual grains can have an effect on the hardness measurements of polycrystalline samples [145]. The measurements performed can, therefore, be compared to an EBSD orientation map such as seen in Figure 5.43 to determine whether certain crystal orientations are affected more strongly by the synergistic loads studied in this work. As already discussed, there is no significant difference between the individual measurements in the areas unaffected by the laser pulses nor is there, in any case, a sufficient number of data points to make a meaningful analysis (see Table 5.3). These areas will therefore not be included in this discussion.

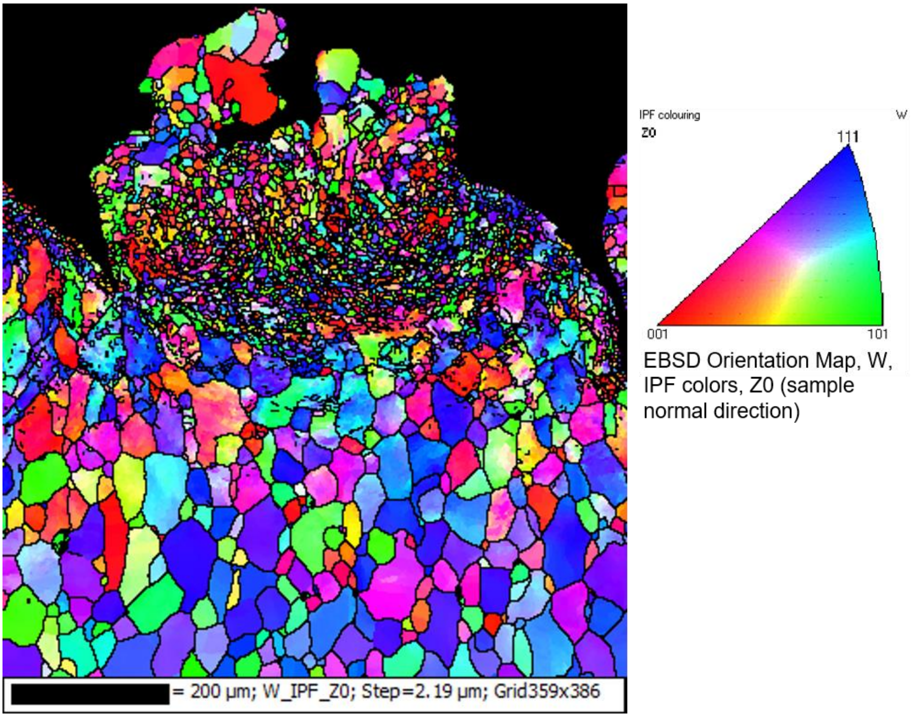

Figure 5.43. EBSD orientation map of the recrystallized tungsten sample exposed to 10^5 0.5 ms laser pulses with a frequency of 10 Hz and an 0.8 GWm^{-2}, at 700 °C base temperature, and a simultaneous steady-state D/He(6%) plasma flux of $3.3 \cdot 10^{21}$ $m^{-2}s^{-1}$.

At the top of the loaded area, two different grains with different crystal orientations (a and b in Figure 5.44) were analyzed. No significant difference was observed in these cases. For the smaller grains, a larger number of grains with different crystal orientations were then tested as indicated in Figure 5.44. No measurable relationship between crystal orientation and hardness values was observed here either. It should be added that not all measurements could be matched to a certain grain, this was only possible for 28 of the indents.

Past experiments performed on helium irradiated tungsten observed a higher hardness increase on (001) crystals than for other crystal orientations [145]. These experiments were performed on the irradiated surface of the sample directly, as the sample surface remained smooth enough after irradiation. In another experiment using Fe^{3+} ions to irradiate a tungsten sample, it was observed that (001) surfaces are damaged and hardened deeper into the grains [146]. In the current experiment, as explained before, it was not possible to perform nanoindentation measurements directly on the surface because of its high roughness. Measuring hardness in the cross-section of the samples adds different variables to the measurements which might not allow to observe a dependence of crystal orientation on hardness even if it were there.

Firstly, the process of cutting, grinding, polishing and chemical etching can all modify the superficial microstructure of the material, adding or eliminating defects. Since nanoindentation tests the material at such a shallow depth, surface effects have a big impact on the outcome of the measurements. Secondly, plasma particles have a greater effect on the surface of the sample, and the deeper into the sample, the smaller the influence it will have on the material properties. Thermal shocks and the temperature increase caused by them, also have a larger impact on the surface than deeper into the bulk, although their influence penetrates deeper into the sample. In the EBSD it can be seen how the grain structure gradually changes until in the lower part of the image the microstructure is seemingly unaffected by the loading. This has been discussed in previous chapters.

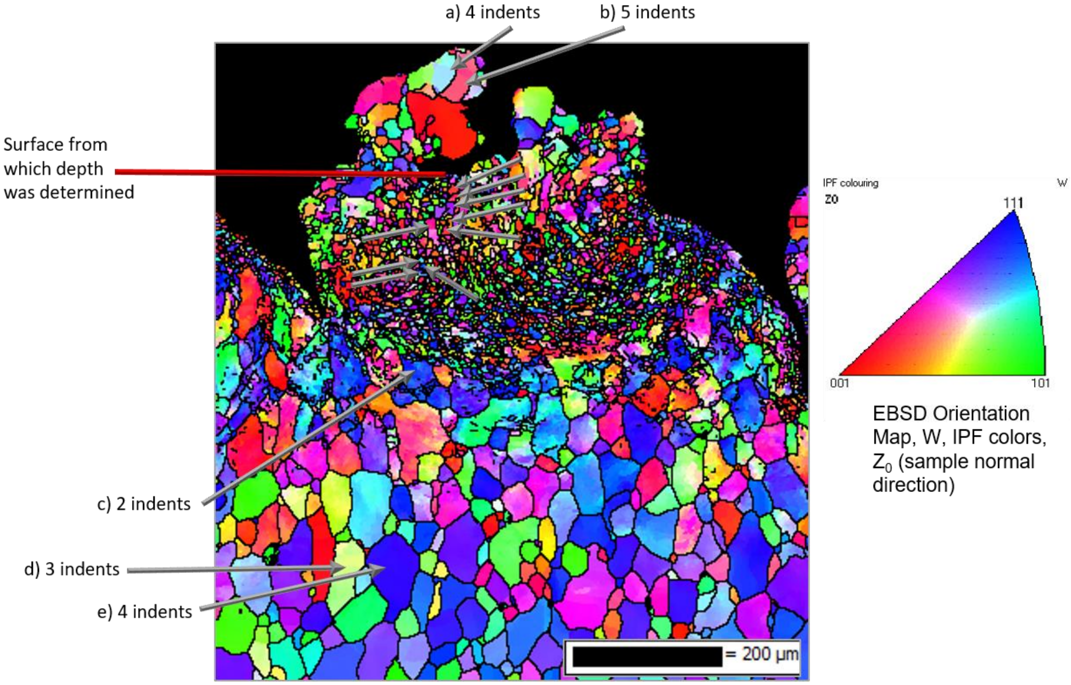

Figure 5.44. Detailed EBSD orientation map of the identifiable grains analyzed via nanoindentation.

Since depth might, then, have a much larger influence on how the hardness of the material changes, it is also of importance to more closely analyze this change. This could help evaluate how deep the PFMs in the ITER divertor will be affected by the different loads it has to withstand. The measured hardness of the grains in relation to the depth of the grain can be seen in Figure 5.45. In approximately the first 150 µm, there is a large spread in the hardness values measured. This might be due to the different grain sizes, shapes, crystal orientations, presence of pores and defects, etc. that can influence the hardness of the grain. In this area of the sample, due to the high loads applied, all these factors can vary greatly. Even after 500 µm, where grains are not so evidently affected by the thermal shocks and grain nucleation, hardness is slightly higher than in the unexposed areas of the sample. This allows the prediction of an increased hardness in all the tungsten surfaces in the ITER divertor that will be continuously exposed to ELMs.

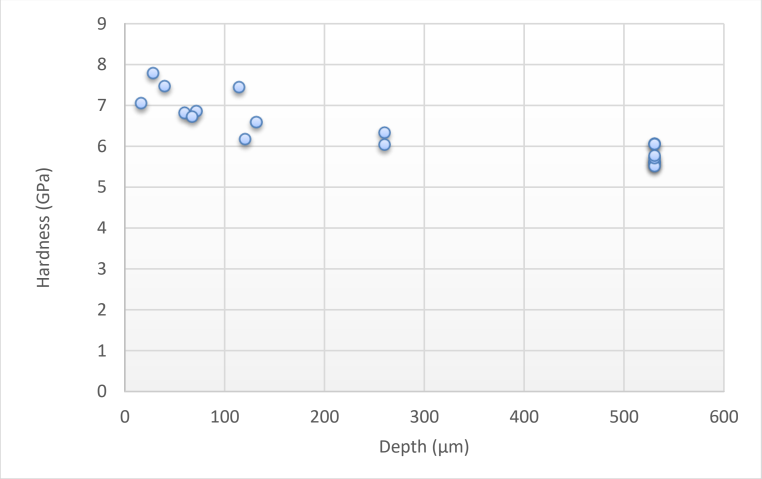

Figure 5.45. Hardness of grains in relation to their depth below the surface in the recrystallized tungsten sample exposed to 10^5 0.5 ms laser pulses with a frequency of 10 Hz and an 0.8 GWm^{-2}, at 700 °C base temperature, and a simultaneous steady-state D/He(6%) plasma flux of $3.3 \cdot 10^{21}$ $m^{-2}s^{-1}$.

5.6. Summary and conclusions

In order to test the effects ELMs will have on tungsten components in ITER, ITER-grade tungsten samples were tested in the linear plasma device PSI-2. Two kinds of samples were utilized, one with needle-like grains transversal to the sample surface, which is the preferred microstructure for the ITER divertor, the other with larger, isotropic grains obtained after recrystallization of transversal samples at 1600 °C for 1 h. Additionally, samples were first exposed to each kind of load separately to study the effects independently of each other. Samples were then exposed to both loads simultaneously to analyze the possible synergistic effects of such loads. In order to facilitate having a complete overview of the results presented in this work, a summary of the effects of ELM-like loads observed in transversal samples is presented in Figure 5.46.

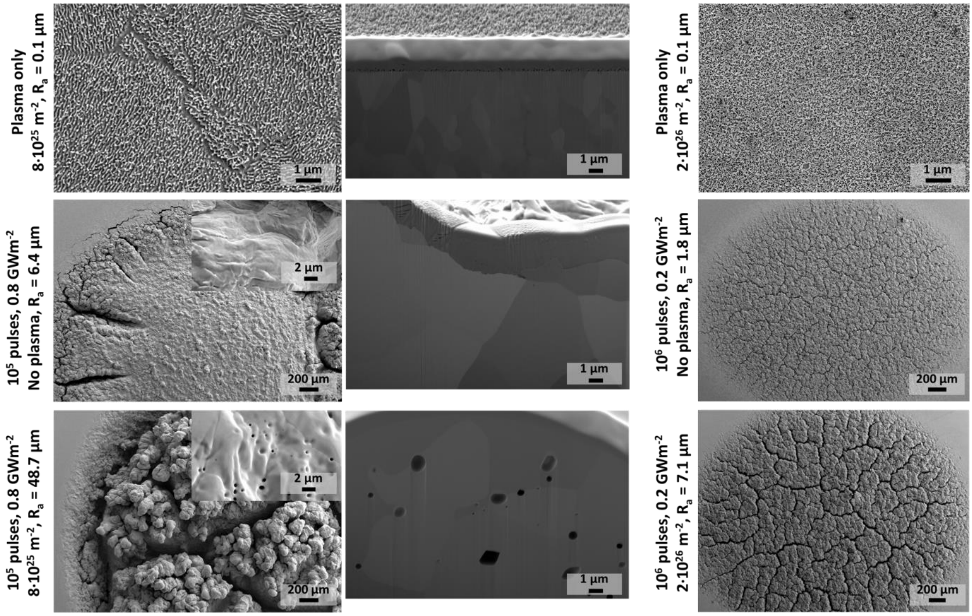

Figure 5.46. Summary of the effects of ELM-like loads observed on ITER-grade tungsten tested in the linear plasma device PSI-2 under separate and simultaneous transient thermal and stationary plasma loads. A D/He(6%) plasma mixture was used and samples were kept at a 700-900 °C base temperature.

By exposing the samples to low energy plasma particles (35-40 eV) at a 700 °C base temperature, the formation of nanotendrils, known as tungsten fuzz, on the surface was observed, without any indication of further surface modification or damage. This corroborates similar observations from previous works. No significant difference was observed between recrystallized and transversal samples in this case.

The influence of only the transient heat loads was then investigated. It was observed that the fatigue stress applied by the laser pulses has a larger effect on the damage observed than the plasma particles. 10^5 laser pulses of 0.2 $\mathrm{GWm^{-2}}$ caused no observable cracking in transversal samples, and very slight cracking in recrystallized ones. A crack network formed only after applying 10^6 pulses to the samples. With higher P_{abs}, of 0.4 and 0.8 $\mathrm{GWm^{-2}}$, a crack network already starts forming after exposure to 10^5 pulses.

Once the effects of the separate loads were determined, the influence of the simultaneous exposure to both loads was investigated. In all cases, the cracking observed was exacerbated by the synergy between both loads. Hydrogen embrittlement and the formation of helium bubbles deteriorate the material properties, which cause the increased cracking and plastic deformation of the material.

The formation of bubbles in the material can be of particular importance for the material behavior in PFMs. It was observed that applying pulses of 0.8 $\mathrm{GWm^{-2}}$ substantially accelerates the growth of helium bubbles near the surface of the material. A further increase in bubble size was observed by increasing the plasma fluence applied. Additionally, an increase in hardness was observed in the area of the material affected by both kinds of loads. This effect decreases with depth and is not observed in areas affected only by plasma.

Furthermore, by analyzing the residual stresses of the samples via the $\sin^2\Psi$ it was observed that as-received transversal samples have significant compressive stresses in the surface. This explains the higher damage threshold displayed by the transversal material compared to recrystallized samples. Residual stresses are relaxed after exposure to heat and plasma loads, although the measurement of the stresses is impaired by the cracking and surface roughness of samples exposed to the higher loads.

The higher cracking threshold for transversal samples is one of the reasons why it is the preferred microstructure for the ITER divertor PFMs. These tests have, however, revealed that this difference has no effect on the behavior of the material at higher loads. This is, partly, due to the fact that the surface temperature reaches the recrystallization temperature for tungsten and the elongated, transversal microstructure is eventually lost. This suggests that in areas of the ITER divertor where loads are lower, the transversal microstructure might be conserved and have superior performance to other microstructures. However, where the highest loads are expected, such as at the strike points, the initial microstructure might prove to be irrelevant, as widespread recrystallization is expected.

6. General conclusions and outlook

The main objective of this work was to study the effects of ITER-relevant ELM-like transient thermal and stationary plasma loads on ITER-grade tungsten. This objective stems from previous works where it was revealed that the behavior of PFMs when exposed to ELM-like loads should be studied further.

The results presented in this work have demonstrated how vital ELM mitigation and control is for the success of ITER. A much lower number of ELM-like events was tested than what is expected in the lifetime of ITER, and already widespread cracking was observed. Cracking is not, in and of itself an issue for the functioning of ITER, but it might lead to other problems, such as increased erosion of tungsten, which would, in turn, cause a cool down of the plasma. The likely formation of tungsten fuzz in different parts of the inner walls of the reactor could also increase the erosion of the material. Erosion in ITER-relevant conditions is being intensively studied, for example, in JET with its ITER-like wall (ILW) [147].

Aside from cracking and fuzz formation, the PFMs will be affected by different phenomena, which will all have an influence on their properties. Recrystallization will modify the initial microstructure of the material. Bubble formation will affect the swelling of the material, its heat dissipation capabilities and its mechanical characteristics. The formation and relaxation of residual stresses will also affect their behavior. Additionally, the surface of the PFMs will gradually become hardened and embrittled by the combination of heat and plasma loads.

Furthermore, this work did not take the effects of neutron irradiation into account. In ITER, apart from the plasma and heat loads, there will be neutrons bombarding the PFCs. This will modify the lattice structure of the materials, as well as causing the transmutation of tungsten into, mainly, rhenium and osmium. The effect that the combination of all these effects will have on the material has still not been properly studied, as the coupling of a neutron source would require the inclusion of the whole facility into a hot cell, and this presents serious challenges for the design and maintenance of the equipment. This will be the natural the next step in material testing, which is why testing facilities such as the Divertor Tokamak Test-Facility (DTT) in Italy and the JULE-PSI in Germany are being built.

For future fusion reactors such as DEMO, advanced materials and engineering solutions are being developed to improve the performance of PFCs. These include alloys, smart alloys, microstructured tungsten, functionally graded materials, fiber reinforced tungsten (W_f/W), layered tungsten and even liquid metals. An overview of the materials and designs being considered can be seen in [34,148–158] and references therein. Each of these PFMs and PFCs must be intensely tested if an option is to be chosen. However, independently of the design, no clear answer will be able to be obtained that fully reveals the behavior of ITER-grade tungsten or any other material until ITER itself performs full-power tests. What can be said from this work is that, as long as the expected ELM energies are not surpassed, tungsten PFMs will most probably be able to withstand the first stages of operation. What will happen once neutrons start having a substantial effect on the components remains to be seen.

7. Appendix

Table 7.1. Superficial residual stresses in transversal and recrystallized tungsten samples measured via XRD using the $\sin^2\Psi$ method.

	Power Dens. (GW m^{-2})		*No laser*	*0,2*	*0,4*	*0,8*
	Pulses	**Flux (*10^{21} m^{-2})**	**Residual stress (MPa)**			
T	0	0	-253,5 ± 46			
	10^5	6	-97 ± 18	74 ± 4	5 ± 3	32 ± 10
	10^4	3.3	-185 ± 63	-185 ± 11	215 ± 9	61 ± 6
	10^5	3.3	-184 ± 47	210 ± 7	2 ± 5	-22 ± 20
	10^5	7.4		25 ± 8	-8 ± 7	-35 ± 17
R	10^4	3.3		125 ± 26	142 ± 17	88 ± 10
	10^5	3.3		91 ± 15	48 ± 2	18 ± 13
	10^5	7.4		41 ± 14	12 ± 6	-25 ± 11

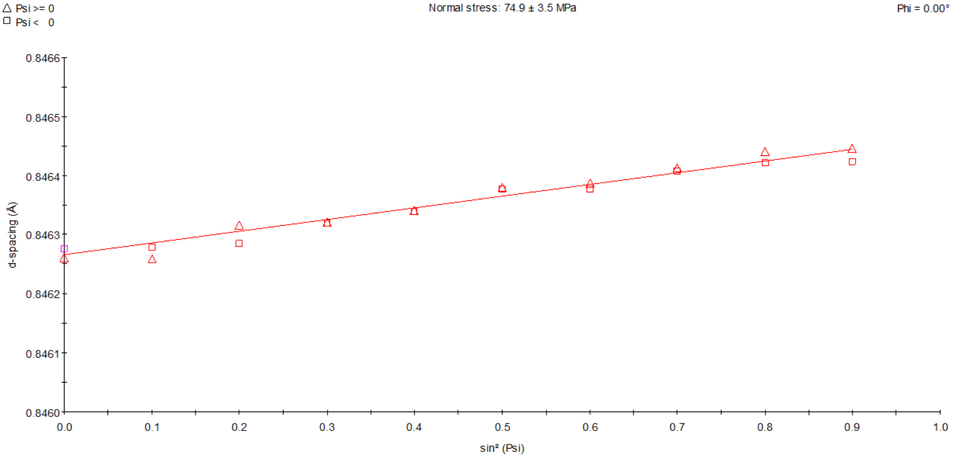

Figure 7.1. Example of a residual stress measurement using the $\sin^2\Psi$ method. The measurement was performed on a transversal sample exposed to 10^5 laser pulses of 0.2 GWm^{-2}, at 700 °C base temperature, and a simultaneous steady-state D/He(6%) plasma flux of 6.0 ·10^{21} m^{-2}s^{-1}.

References

[1] U.S. Energy Information Administration, International Energy Outlook 2017, 2017.

[2] ITER, ITER - the way to new energy, https://www.iter.org/, accessed 22 October 2018.

[3] G.M. McCracken, P. Stott, Fusion: The energy of the universe, Academic Press, Burlington, 2005.

[4] E. Morse, Nuclear Fusion, Springer International Publishing, Cham, 2018.

[5] K.R. Lang, Essential Astrophysics, Springer Berlin Heidelberg, Berlin, Heidelberg, 2013.

[6] Y. Wu, Fusion Neutronics, Springer Singapore, Singapore, 2017.

[7] C. Seife, Sun in a bottle: The strange history of fusion and the science of wishful thinking, Penguin Books, New York, New York, 2008.

[8] EuroFusion, EUROfusion, https://www.euro-fusion.org/, accessed 1 July 2020.

[9] V. Lukash, R.R. Khayrutdinov (Eds.), Model of real time ITER plasma position, shape and current control on base of DINA code, 2007.

[10] Y. Xu, A general comparison between tokamak and stellarator plasmas, Matter and Radiation at Extremes 1 (2016) 192–200. https://doi.org/10.1016/j.mre.2016.07.001.

[11] M. Nagel, C.P. Dhard, H. Bau, H.-S. Bosch, U. Meyer, S. Raatz, K. Risse, T. Rummel, Cryogenic commissioning, cool down and first magnet operation of Wendelstein 7-X, IOP Conf. Ser.: Mater. Sci. Eng. 171 (2017) 12050. https://doi.org/10.1088/1757-899X/171/1/012050.

[12] M. Keilhacker, A. Gibson, C. Gormezano, P. Rebut, The scientific success of JET, Nucl. Fusion 41 (2001) 1925–1966. https://doi.org/10.1088/0029-5515/41/12/217.

[13] M. Claessens, ITER: The Giant Fusion Reactor: Bringing a Sun to Earth, 1st ed., 2020.

[14] A roadmap to the realisation of fusion energy.

[15] Forschungszentrum Jülich, Plasma-Wall Interaction: A Key Issue in Progress Towards Fusion Power Plants, https://www.fz-juelich.de/iek/iek-4/EN/Research/01_Plasma-Wall_Interaction/artikel_2014.html?nn=1500636, accessed 2 July 2020.

[16] T. Hirai, F. Escourbiac, S. Carpentier-Chouchana, A. Fedosov, L. Ferrand, T. Jokinen, V. Komarov, A. Kukushkin, M. Merola, R. Mitteau, R.A. Pitts, W. Shu, M. Sugihara, B. Riccardi, S. Suzuki, R. Villari, ITER tungsten divertor design development and qualification program, Fusion Engineering and Design 88 (2013) 1798–1801. https://doi.org/10.1016/j.fusengdes.2013.05.010.

[17] R.A. Pitts, S. Bardin, B. Bazylev, M.A. van den Berg, P. Bunting, S. Carpentier-Chouchana, J.W. Coenen, Y. Corre, R. Dejarnac, F. Escourbiac, J. Gaspar, J.P. Gunn, T. Hirai, S.-H. Hong, J. Horacek, D. Iglesias, M. Komm, K. Krieger, C. Lasnier, G.F. Matthews, T.W. Morgan, S. Panayotis, S. Pestchanyi, A. Podolnik, R.E. Nygren, D.L. Rudakov, G. de Temmerman, P. Vondracek, J.G. Watkins, Physics conclusions in support of ITER W divertor monoblock shaping, Nuclear Materials and Energy. https://doi.org/10.1016/j.nme.2017.03.005.

[18] R.A. Pitts, S. Carpentier, F. Escourbiac, T. Hirai, V. Komarov, A.S. Kukushkin, S. Lisgo, A. Loarte, M. Merola, R. Mitteau, A.R. Raffray, M. Shimada, P.C. Stangeby, Physics basis and design of the ITER plasma-facing components, Journal of Nuclear Materials 415 (2011) S957-S964. https://doi.org/10.1016/j.jnucmat.2011.01.114.

[19] T. Hirai, S. Panayotis, V. Barabash, C. Amzallag, F. Escourbiac, A. Durocher, M. Merola, J. Linke, T. Loewenhoff, G. Pintsuk, M. Wirtz, I. Uytdenhouwen, Use of tungsten material for the ITER divertor, Nuclear Materials and Energy 9 (2016) 616–622. https://doi.org/10.1016/j.nme.2016.07.003.

[20] V. Barabash, A. Peacock, S. Fabritsiev, G. Kalinin, S. Zinkle, A. Rowcliffe, J.-W. Rensman, A.A. Tavassoli, P. Marmy, P.J. Karditsas, F. Gillemot, M. Akiba, Materials challenges for ITER – Current status and future activities, Journal of Nuclear Materials 367-370 (2007) 21–32. https://doi.org/10.1016/j.jnucmat.2007.03.017.

[21] V. Barabash, G. Federici, R. Matera, A.R. Raffray, I. Home Teams, Armour Materials for the ITER Plasma Facing Components, Phys. Scr. T81 (1999) 74. https://doi.org/10.1238/Physica.Topical.081a00074.

[22] M. Merola, D. Loesser, A. Martin, P. Chappuis, R. Mitteau, V. Komarov, R.A. Pitts, S. Gicquel, V. Barabash, L. Giancarli, J. Palmer, M. Nakahira, A. Loarte, D. Campbell, R. Eaton, A. Kukushkin, M. Sugihara, F. Zhang, C.S. Kim, R. Raffray, L. Ferrand, D. Yao, S. Sadakov, A. Furmanek, V. Rozov, T. Hirai, F. Escourbiac, T. Jokinen, B. Calcagno, S. Mori, ITER plasma-facing components, Fusion Engineering and Design 85 (2010) 2312–2322. https://doi.org/10.1016/j.fusengdes.2010.09.013.

[23] H. Bolt, V. Barabash, G. Federici, J. Linke, A. Loarte, J. Roth, K. Sato, Plasma facing and high heat flux materials – needs for ITER and beyond, Journal of Nuclear Materials 307-311 (2002) 43–52. https://doi.org/10.1016/S0022-3115(02)01175-3.

[24] R. Neu, K. Asmussen, S. Deschka, A. Thoma, M. Bessenrodt-Weberpals, R. Dux, W. Engelhardt, J.C. Fuchs, J. Gaffert, C. García-Rosales, A. Herrmann, K. Krieger, F. Mast, J. Roth, V. Rohde, M. Weinlich, U. Wenzel, The tungsten experiment in ASDEX Upgrade, Journal of Nuclear Materials 241-243 (1997) 678–683. https://doi.org/10.1016/S0022-3115(97)80121-3.

[25] Y. Ueda, K. Schmid, M. Balden, J.W. Coenen, T. Loewenhoff, A. Ito, A. Hasegawa, C. Hardie, M. Porton, M. Gilbert, Baseline high heat flux and plasma facing materials for fusion, Nucl. Fusion 57 (2017) 92006. https://doi.org/10.1088/1741-4326/aa6b60.

[26] F. Andritsos, M. Zucchetti, Afterheat transient in ITER after a total loss of coolant accident, Fusion Engineering and Design 15 (1991) 113–119. https://doi.org/10.1016/0920-3796(91)90219-G.

[27] T. Loarer, C. Brosset, J. Bucalossi, P. Coad, G. Esser, J. Hogan, J. Likonen, M. Mayer, P. Morgan, V. Philipps, V. Rohde, J. Roth, M. Rubel, E. Tsitrone, A. Widdowson, Gas balance and fuel retention in fusion devices, Nucl. Fusion 47 (2007) 1112–1120. https://doi.org/10.1088/0029-5515/47/9/007.

[28] M.R. Gilbert, J.-C. Sublet, Neutron-induced transmutation effects in W and W-alloys in a fusion environment, Nucl. Fusion 51 (2011) 43005. https://doi.org/10.1088/0029-5515/51/4/043005.

[29] S. Brezinsek, T. Loarer, V. Philipps, H.G. Esser, S. Grünhagen, R. Smith, R. Felton, J. Banks, P. Belo, A. Boboc, J. Bucalossi, M. Clever, J.W. Coenen, I. Coffey, S. Devaux, D. Douai, M. Freisinger, D. Frigione, M. Groth, A. Huber, J. Hobirk, S. Jachmich, S. Knipe, K. Krieger, U. Kruezi, S. Marsen, G.F. Matthews, A.G. Meigs, F. Nave, I. Nunes, R. Neu, J. Roth, M.F. Stamp, S. Vartanian, U. Samm, Fuel retention studies with the ITER-Like Wall in JET, Nucl. Fusion 53 (2013) 83023. https://doi.org/10.1088/0029-5515/53/8/083023.

[30] T. Kuroda, G. Vieider, M. Akiba, ITER Plasma Facing Components, 1991.

[31] V. Philipps, T. Loarer, H.G. Esser, S. Vartanian, U. Kruezi, S. Brezinsek, G. Matthews, Dynamic fuel retention and release under ITER like wall conditions in JET, Journal of Nuclear Materials 438 (2013) S1067-S1071. https://doi.org/10.1016/j.jnucmat.2013.01.234.

[32] H. Bolt, V. Barabash, W. Krauss, J. Linke, R. Neu, S. Suzuki, N. Yoshida, A.U. Team, Materials for the plasma-facing components of fusion reactors, Journal of Nuclear Materials 329-333 (2004) 66–73. https://doi.org/10.1016/j.jnucmat.2004.04.005.

[33] A. Litnovsky, T. Wegener, F. Klein, C. Linsmeier, M. Rasinski, A. Kreter, B. Unterberg, J.W. Coenen, H. Du, J. Mayer, C. Garcia-Rosales, A. Calvo, N. Ordas, Smart tungsten alloys as a material for the first wall of a future fusion power plant, Nucl. Fusion 57 (2017) 66020. https://doi.org/10.1088/1741-4326/aa6816.

[34] J.W. Coenen, S. Antusch, M. Aumann, W. Biel, J. Du, J. Engels, S. Heuer, A. Houben, T. Hoeschen, B. Jasper, F. Koch, J. Linke, A. Litnovsky, Y. Mao, R. Neu, G. Pintsuk, J. Riesch, M. Rasinski, J. Reiser, M. Rieth, A. Terra, B. Unterberg, T. Weber, T. Wegener, J.-H. You, C. Linsmeier, Materials for DEMO and reactor applications—boundary conditions and new concepts, Phys. Scr. (2016).

[35] G. Pintsuk, Tungsten as a Plasma-Facing Material, in: Comprehensive Nuclear Materials, Elsevier, 2012, pp. 551–581.

[36] J. Davis, V. Barabash, A. Makhankov, L. Plöchl, K. Slattery, Assessment of tungsten for use in the ITER plasma facing components, Journal of Nuclear Materials 258-263 (1998) 308–312. https://doi.org/10.1016/S0022-3115(98)00285-2.

[37] M. Shimada, R. Pitts, A. Loarte, D.J. Campbell, M. Sugihara, V. Mukhovatov, A. Kukushkin, V. Chuyanov, ITER research plan of plasma–wall interaction, Journal of Nuclear Materials 390-391 (2009) 282–285. https://doi.org/10.1016/j.jnucmat.2009.01.113.

[38] V. Philipps, Tungsten as material for plasma-facing components in fusion devices, Journal of Nuclear Materials 415 (2011) S2-S9. https://doi.org/10.1016/j.jnucmat.2011.01.110.

[39] R.A. Pitts, A. Kukushkin, A. Loarte, A. Martin, M. Merola, C.E. Kessel, V. Komarov, M. Shimada, Status and physics basis of the ITER divertor, Phys. Scr. T138 (2009) 14001. https://doi.org/10.1088/0031-8949/2009/T138/014001.

[40] Comparison of Fuel Retention in JET between Carbon and the ITER-Like Wall.

[41] J. Linke, J. Du, T. Loewenhoff, G. Pintsuk, B. Spilker, I. Steudel, M. Wirtz, Challenges for plasma-facing components in nuclear fusion, Matter and Radiation at Extremes 4 (2019) 56201. https://doi.org/10.1063/1.5090100.

[42] S. Panayotis, T. Hirai, V. Barabash, A. Durocher, F. Escourbiac, J. Linke, T. Loewenhoff, M. Merola, G. Pintsuk, I. Uytdenhouwen, M. Wirtz, Self-castellation of tungsten monoblock under high heat flux loading and impact of material properties, Nuclear Materials and Energy. https://doi.org/10.1016/j.nme.2016.10.025.

[43] X.-X. Zhang, Q.-Z. Yan, C.-T. Yang, T.-N. Wang, M. Xia, C.-C. Ge, Recrystallization temperature of tungsten with different deformation degrees, Rare Met. 35 (2016) 566–570. https://doi.org/10.1007/s12598-014-0315-2.

[44] M. Richou, A. Durif, M. Lenci, M. Mondon, M. Minissale, L. Gallais, G. Kermouche, G. de Temmerman, Recrystallization at high temperature of two tungsten materials complying with the ITER specifications, Journal of Nuclear Materials 542 (2020) 152418. https://doi.org/10.1016/j.jnucmat.2020.152418.

[45] J.P. Gunn, S. Carpentier-Chouchana, F. Escourbiac, T. Hirai, S. Panayotis, R.A. Pitts, Y. Corre, R. Dejarnac, M. Firdaouss, M. Kočan, M. Komm, A. Kukushkin, P. Languille, M. Missirlian, W. Zhao, G. Zhong, Surface heat loads on the ITER divertor vertical targets, Nucl. Fusion 57 (2017) 46025. https://doi.org/10.1088/1741-4326/aa5e2a.

[46] T. Eich, B. Sieglin, A.J. Thornton, M. Faitsch, A. Kirk, A. Herrmann, W. Suttrop, ELM divertor peak energy fluence scaling to ITER with data from JET, MAST and ASDEX upgrade, Nuclear Materials and Energy 12 (2017) 84–90. https://doi.org/10.1016/j.nme.2017.04.014.

[47] F. Wagner, G. Becker, K. Behringer, D. Campbell, A. Eberhagen, W. Engelhardt, G. Fussmann, O. Gehre, J. Gernhardt, G.v. Gierke, G. Haas, M. Huang, F. Karger, M. Keilhacker, O. Klüber, M. Kornherr, K. Lackner, G. Lisitano, G.G. Lister, H.M. Mayer, D. Meisel, E.R. Müller, H. Murmann, H. Niedermeyer, W. Poschenrieder, H. Rapp, H. Röhr, F. Schneider, G. Siller, E. Speth, A. Stäbler, K.H. Steuer, G. Venus, O. Vollmer, Z. Yü, Regime of Improved Confinement and High Beta in Neutral-Beam-Heated Divertor Discharges of the ASDEX Tokamak, Phys. Rev. Lett. 49 (1982) 1408–1412. https://doi.org/10.1103/PhysRevLett.49.1408.

[48] H. Zohm, Edge localized modes (ELMs), Plasma Phys. Control. Fusion 38 (1996) 105–128. https://doi.org/10.1088/0741-3335/38/2/001.

[49] T. Eich, A. Herrmann, G. Pautasso, P. Andrew, N. Asakura, J.A. Boedo, Y. Corre, M.E. Fenstermacher, J.C. Fuchs, W. Fundamenski, G. Federici, E. Gauthier, B. Goncalves, O. Gruber, A. Kirk, A.W. Leonard, A. Loarte, G.F. Matthews, J. Neuhauser, R.A. Pitts, V. Riccardo, C. Silva, Power deposition onto plasma facing components in poloidal divertor tokamaks during type-I ELMs and disruptions, Journal of Nuclear Materials 337-339 (2005) 669–676. https://doi.org/10.1016/j.jnucmat.2004.09.051.

[50] J. Linke, T. Loewenhoff, V. Massaut, G. Pintsuk, G. Ritz, M. Rödig, A. Schmidt, C. Thomser, I. Uytdenhouwen, V. Vasechko, M. Wirtz, Performance of different tungsten grades under transient thermal loads, Nucl. Fusion 51 (2011) 73017. https://doi.org/10.1088/0029-5515/51/7/073017.

[51] R.A. Pitts, X. Bonnin, F. Escourbiac, H. Frerichs, J.P. Gunn, T. Hirai, A.S. Kukushkin, E. Kaveeva, M.A. Miller, D. Moulton, V. Rozhansky, I. Senichenkov, E. Sytova, O. Schmitz, P.C. Stangeby, G. de Temmerman, I. Veselova, S. Wiesen, Physics basis for the first ITER tungsten divertor, Nuclear Materials and Energy 20 (2019) 100696. https://doi.org/10.1016/j.nme.2019.100696.

[52] R.A. Pitts, S. Carpentier, F. Escourbiac, T. Hirai, V. Komarov, S. Lisgo, A.S. Kukushkin, A. Loarte, M. Merola, A. Sashala Naik, R. Mitteau, M. Sugihara, B. Bazylev, P.C. Stangeby, A full tungsten divertor for ITER, Journal of Nuclear Materials 438 (2013) S48-S56. https://doi.org/10.1016/j.jnucmat.2013.01.008.

[53] T. Loewenhoff, J. Linke, G. Pintsuk, C. Thomser, Tungsten and CFC degradation under combined high cycle transient and steady state heat loads, Fusion Engineering and Design 87 (2012) 1201–1205. https://doi.org/10.1016/j.fusengdes.2012.02.106.

[54] T. Hirai, G. Pintsuk, J. Linke, M. Batilliot, Cracking failure study of ITER-reference tungsten grade under single pulse thermal shock loads at elevated temperatures, Journal of Nuclear Materials 390-391 (2009) 751–754. https://doi.org/10.1016/j.jnucmat.2009.01.313.

[55] R. Dux, A. Loarte, C. Angioni, D. Coster, E. Fable, A. Kallenbach, The interplay of controlling the power exhaust and the tungsten content in ITER, Nuclear Materials and Energy 12 (2017) 28–35. https://doi.org/10.1016/j.nme.2016.10.013.

[56] M. Dürrschnabel, M. Klimenkov, U. Jäntsch, M. Rieth, H.C. Schneider, D. Terentyev, New insights into microstructure of neutron-irradiated tungsten, Scientific reports 11 (2021) 7572. https://doi.org/10.1038/s41598-021-86746-6.

[57] T. Noda, M. Fujita, M. Okada, Transmutation and induced radioactivity of W in the armor and first wall of fusion reactors, Journal of Nuclear Materials 258-263 (1998) 934–939. https://doi.org/10.1016/S0022-3115(98)00088-9.

[58] R. Villari, V. Barabash, F. Escourbiac, L. Ferrand, T. Hirai, V. Komarov, M. Loughlin, M. Merola, F. Moro, L. Petrizzi, S. Podda, E. Polunovsky, G. Brolatti, Nuclear analysis of the ITER full-tungsten divertor, Fusion Engineering and Design 88 (2013) 2006–2010. https://doi.org/10.1016/j.fusengdes.2013.02.156.

[59] S. Javadi, B. Ouyang, Z. Zhang, M. Ghoranneviss, A. Salar Elahi, R.S. Rawat, Effects of fusion relevant transient energetic radiation, plasma and thermal load on PLANSEE double forged tungsten samples in a low-energy plasma focus device, Applied Surface Science 443 (2018) 311–320. https://doi.org/10.1016/j.apsusc.2018.03.039.

[60] D. Papadakis, S. Dellis, K. Mergia, D. Terentyev, G. Bonny, A. Dubinko, W. van Renterghem, M. Konstantinovic, S. Messoloras, The competing effects of temperature and neutron irradiation on the mechanical properties and microstructure of forged tungsten bar.

[61] E. Gaganidze, A. Chauhan, H.-C. Schneider, D. Terentyev, G. Borghmans, J. Aktaa, Fracture-mechanical properties of neutron irradiated ITER specification tungsten.

[62] P.D. Edmondson, A. London, A. Xu, D. Armstrong, S.G. Roberts, Small-scale characterisation of irradiated nuclear materials: Part I – Microstructure, Journal of Nuclear Materials 462 (2015) 369–373. https://doi.org/10.1016/j.jnucmat.2014.11.067.

[63] S. Das, D. Armstrong, Y. Zayachuk, W. Liu, R. Xu, F. Hofmann, The effect of helium implantation on the deformation behaviour of tungsten: X-ray micro-diffraction and nanoindentation, Scripta Materialia 146 (2018) 335–339. https://doi.org/10.1016/j.scriptamat.2017.12.014.

[64] G. de Temmerman, T. Hirai, R.A. Pitts, The influence of plasma-surface interaction on the performance of tungsten at the ITER divertor vertical targets, Plasma Phys. Control. Fusion 60 (2018) 44018. https://doi.org/10.1088/1361-6587/aaaf62.

[65] J. Roth, E. Tsitrone, A. Loarte, T. Loarer, G. Counsell, R. Neu, V. Philipps, S. Brezinsek, M. Lehnen, P. Coad, C. Grisolia, K. Schmid, K. Krieger, A. Kallenbach, B. Lipschultz, R. Doerner, R. Causey, V. Alimov, W. Shu, O. Ogorodnikova, A. Kirschner, G. Federici, A. Kukushkin, Recent analysis of key plasma wall interactions issues for ITER, Journal of Nuclear Materials 390-391 (2009) 1–9. https://doi.org/10.1016/j.jnucmat.2009.01.037.

[66] M.J. Baldwin, R.P. Doerner, Formation of helium induced nanostructure ‘fuzz’ on various tungsten grades, Journal of Nuclear Materials 404 (2010) 165–173. https://doi.org/10.1016/j.jnucmat.2010.06.034.

[67] S. Nagata, B. Tsuchiya, T. Sugawara, N. Ohtsu, T. Shikama, Helium and hydrogen trapping in W and Mo single-crystals irradiated by He ions, Journal of Nuclear Materials 307-311 (2002) 1513–1516. https://doi.org/10.1016/S0022-3115(02)01269-2.

[68] C.N. Taylor, M. Shimada, B.J. Merrill, Deuterium retention and blistering in tungsten foils, Nuclear Materials and Energy 12 (2017) 689–693. https://doi.org/10.1016/j.nme.2016.12.004.

[69] M. Thompson, Helium Nano-bubble Formation in Tungsten: Measurement with Grazing-Incidence Small Angle X-ray Scattering, Canberra, 2018.

[70] M. Thompson, A. Deslandes, T.W. Morgan, R.G. Elliman, G. de Temmerman, P. Kluth, D. Riley, C.S. Corr, Observation of a helium ion energy threshold for retention in tungsten exposed to hydrogen/helium mixture plasma, Nucl. Fusion 56 (2016) 104002. https://doi.org/10.1088/0029-5515/56/10/104002.

[71] M. Thompson, D. Drummond, J. Sullivan, R. Elliman, P. Kluth, N. Kirby, D. Riley, C.S. Corr, Effect of W self-implantation and He plasma exposure on early-stage defect and bubble formation in tungsten, Nucl. Fusion 58 (2018) 66010. https://doi.org/10.1088/1741-4326/aab96c.

[72] W. Wang, J. Roth, S. Lindig, C. Wu, Blister formation of tungsten due to ion bombardment, Journal of Nuclear Materials 299 (2001) 124–131. https://doi.org/10.1016/S0022-3115(01)00679-1.

[73] P.E. Lhuillier, T. Belhabib, P. Desgardin, B. Courtois, T. Sauvage, M.F. Barthe, A.L. Thomann, P. Brault, Y. Tessier, Trapping and release of helium in tungsten, Journal of Nuclear Materials 416 (2011) 13–17. https://doi.org/10.1016/j.jnucmat.2010.12.042.

[74] X. Fang, A. Kreter, M. Rasinski, C. Kirchlechner, S. Brinckmann, C. Linsmeier, G. Dehm, Hydrogen embrittlement of tungsten induced by deuterium plasma: Insights from nanoindentation tests, J. Mater. Res. 33 (2018) 3530–3536. https://doi.org/10.1557/jmr.2018.305.

[75] S. Takamura, N. Ohno, D. Nishijima, S. Kajita, Formation of Nanostructured Tungsten with Arborescent Shape due to Helium Plasma Irradiation, Plasma and Fusion Research 1 (2006) 51. https://doi.org/10.1585/pfr.1.051.

[76] S. Kajita, W. Sakaguchi, N. Ohno, N. Yoshida, T. Saeki, Formation process of tungsten nanostructure by the exposure to helium plasma under fusion relevant plasma conditions, Nucl. Fusion 49 (2009) 95005. https://doi.org/10.1088/0029-5515/49/9/095005.

[77] S. Kajita, N. Yoshida, N. Ohno, Y. Tsuji, Growth of multifractal tungsten nanostructure by He bubble induced directional swelling, New J. Phys. 17 (2015) 43038. https://doi.org/10.1088/1367-2630/17/4/043038.

[78] Y. Ueda, H.Y. Peng, H.T. Lee, N. Ohno, S. Kajita, N. Yoshida, R. Doerner, G. de Temmerman, V. Alimov, G. Wright, Helium effects on tungsten surface morphology and deuterium retention, Journal of Nuclear Materials 442 (2013) S267-S272. https://doi.org/10.1016/j.jnucmat.2012.10.023.

[79] S.I. Krasheninnikov, Viscoelastic model of tungsten ‘fuzz’ growth, Phys. Scr. T145 (2011) 14040. https://doi.org/10.1088/0031-8949/2011/T145/014040.

[80] M. Wirtz, J. Linke, G. Pintsuk, J. Rapp, G.M. Wright, Influence of high flux hydrogen-plasma exposure on the thermal shock induced crack formation in tungsten, Journal of Nuclear Materials 420 (2012) 218–221. https://doi.org/10.1016/j.jnucmat.2011.09.035.

[81] I. Steudel, A. Huber, A. Kreter, J. Linke, G. Sergienko, B. Unterberg, M. Wirtz, Influence of the base temperature on the performance of tungsten under thermal and particle exposure, Nuclear Materials and Energy 12 (2017) 1348–1351. https://doi.org/10.1016/j.nme.2017.03.016.

[82] I. Steudel, A. Huber, A. Kreter, J. Linke, G. Sergienko, B. Unterberg, M. Wirtz, Sequential and simultaneous thermal and particle exposure of tungsten, Phys. Scr. T167 (2016) 14053. https://doi.org/10.1088/0031-8949/T167/1/014053.

[83] S. Brezinsek, J.W. Coenen, T. Schwarz-Selinger, K. Schmid, A. Kirschner, A. Hakola, F.L. Tabares, H.J. van der Meiden, M.-L. Mayoral, M. Reinhart, E. Tsitrone, T. Ahlgren, M. Aints, M. Airila, S. Almaviva, E. Alves, T. Angot, V. Anita, R. Arredondo Parra, F. Aumayr, M. Balden, J. Bauer, M. Ben Yaala, B.M. Berger, R. Bisson, C. Björkas, I. Bogdanovic Radovic, D. Borodin, J. Bucalossi, J. Butikova, B. Butoi, I. Čadež, R. Caniello, L. Caneve, G. Cartry, N. Catarino, M. Čekada, G. Ciraolo, L. Ciupinski, F. Colao, Y. Corre, C. Costin, T. Craciunescu, A. Cremona, M. de Angeli, A. de Castro, R. Dejarnac, D. Dellasega, P. Dinca, T. Dittmar, C. Dobrea, P. Hansen, A. Drenik, T. Eich, S. Elgeti, D. Falie, N. Fedorczak, Y. Ferro, T. Fornal, E. Fortuna-Zalesna, L. Gao, P. Gasior, M. Gherendi, F. Ghezzi, Ž. Gosar, H. Greuner, E. Grigore, C. Grisolia, M. Groth, M. Gruca, J. Grzonka, J.P. Gunn, K. Hassouni, K. Heinola, T. Höschen, S. Huber, W. Jacob, I. Jepu, X. Jiang, I. Jogi, A. Kaiser, J. Karhunen, M. Kelemen, M. Köppen, H.R. Koslowski, A. Kreter, M. Kubkowska, M. Laan, L. Laguardia, A. Lahtinen, A. Lasa, V. Lazic, N. Lemahieu, J. Likonen, J. Linke, A. Litnovsky, C. Linsmeier, T. Loewenhoff, C. Lungu, M. Lungu, G. Maddaluno, H. Maier, T. Makkonen, A. Manhard, Y. Marandet, S. Markelj, L. Marot, C. Martin, A.B. Martin-Rojo, Y. Martynova, R. Mateus, D. Matveev, M. Mayer, G. Meisl, N. Mellet, A. Michau, J. Miettunen, S. Möller, T.W. Morgan, J. Mougenot, M. Mozetič, V. Nemanič, R. Neu, K. Nordlund, M. Oberkofler, E. Oyarzabal, M. Panjan, C. Pardanaud, P. Paris, M. Passoni, B. Pegourie, P. Pelicon, P. Petersson, K. Piip, G. Pintsuk, G.O. Pompilian, G. Popa, C. Porosnicu, G. Primc, M. Probst, J. Räisänen, M. Rasinski, S. Ratynskaia, D. Reiser, D. Ricci, M. Richou, J. Riesch, G. Riva, M. Rosinski, P. Roubin, M. Rubel, C. Ruset, E. Safi, G. Sergienko, Z. Siketic, A. Sima, B. Spilker, R. Stadlmayr, I. Steudel, P. Ström, T. Tadic, D. Tafalla, I. Tale, D. Terentyev, A. Terra, V. Tiron, I. Tiseanu, P. Tolias, D. Tskhakaya, A. Uccello, B. Unterberg, I. Uytdenhoven, E. Vassallo, P. Vavpetič, P. Veis, I.L. Velicu, J. Vernimmen, A. Voitkans, U. von Toussaint, A. Weckmann, M. Wirtz, A. Založnik, R. Zaplotnik, Plasma–wall interaction studies within the EUROfusion consortium, Nucl. Fusion 57 (2017) 116041. https://doi.org/10.1088/1741-4326/aa796e.

[84] T.W. Morgan, G.G. van Eden, T.M. de Kruif, M.A. van den Berg, J. Matejicek, T. Chraska, G. de Temmerman, ELM-induced melting, Phys. Scr. T159 (2014) 14022. https://doi.org/10.1088/0031-8949/2014/T159/014022.

[85] T. Loewenhoff, S. Bardin, H. Greuner, J. Linke, H. Maier, T.W. Morgan, G. Pintsuk, R.A. Pitts, B. Riccardi, G. de Temmerman, Impact of combined transient plasma/heat loads on tungsten performance below and above recrystallization temperature, Nucl. Fusion 55 (2015) 123004. https://doi.org/10.1088/0029-5515/55/12/123004.

[86] A. Kreter, C. Brandt, A. Huber, S. Kraus, S. Möller, M. Reinhart, B. Schweer, G. Sergienko, B. Unterberg, Linear Plasma Device PSI-2 for Plasma-Material Interaction Studies, Fusion Science and Technology 68 (2015) 8–14. https://doi.org/10.13182/FST14-906.

[87] Forschungszentrum Jülich, Plasma-Wall Interaction in Linear Plasma Devices: New challenges, http://www.fz-juelich.de/iek/iek-4/EN/Research/02_Linear_plasma_devices/_node.html, accessed 20 April 2018.

[88] A. Huber, G. Sergienko, M. Wirtz, I. Steudel, A. Arakcheev, S. Brezinsek, A. Burdakov, T. Dittmar, H.G. Esser, M. Freisinger, A. Kreter, J. Linke, C. Linsmeier, P. Mertens, S. Möller, M. Reinhart, A. Terra, B. Unterberg, Deuterium retention in tungsten under combined high cycle ELM-like heat loads and steady-state plasma exposure, Nuclear Materials and Energy 9 (2016) 157–164. https://doi.org/10.1016/j.nme.2016.04.007.

[89] L. Conde, An introduction to Langmuir probe diagnostics of plasmas, 2011, http://plasmalab.aero.upm.es/~lcl/PlasmaProbes/Probes-2010-2.pdf.

[90] J.I. Goldstein, D.E. Newbury, J.R. Michael, N.W. Ritchie, J.H.J. Scott, D.C. Joy, Scanning Electron Microscopy and X-Ray Microanalysis, Springer New York, New York, NY, 2018.

[91] A.J. Schwartz, M. Kumar, B.L. Adams, D.P. Field, Electron Backscatter Diffraction in Materials Science, Springer US, Boston, MA, 2009.

[92] F.L. Frederick, W.O. Winer, A.E. Bergles, G.A. Klutke, K.K. Wang, I. Finnie, J.R. Welty, M.D. Bryant, H.T. Yang, V.C. Mow, F.A. Leckie, D. Gross, A.C. Fischer-Cripps, Nanoindentation, Springer New York, New York, NY, 2011.

[93] Bruker, Quasi-Static Nanoindentation, https://www.bruker.com/de/products-and-solutions/test-and-measurement/nanomechanical-test-systems/nanoindentation.html.

[94] G.S. Schajer (Ed.), Practical residual stress measurement methods, Wiley, Chichester West Sussex United Kingdom, 2013.

[95] M. Shimada, R.A. Pitts, S. Ciattaglia, S. Carpentier, C.H. Choi, G. Dell Orco, T. Hirai, A. Kukushkin, S. Lisgo, J. Palmer, W. Shu, E. Veshchev, In-vessel dust and tritium control strategy in ITER, Journal of Nuclear Materials 438 (2013) S996-S1000. https://doi.org/10.1016/j.jnucmat.2013.01.217.

[96] Plansee, Tungsten, https://www.plansee.com/en/materials/tungsten.html, accessed 18 July 2020.

[97] J. Paju, B. Väli, T. Laas, V. Shirokova, K. Laas, M. Paduch, V.A. Gribkov, E.V. Demina, M.D. Prusakova, V.N. Pimenov, V.A. Makhlaj, M. Antonov, Generation and development of damages in double forged tungsten in different combined regimes of irradiation with extreme heat loads, Journal of Nuclear Materials 495 (2017) 91–102. https://doi.org/10.1016/j.jnucmat.2017.07.042.

[98] G. Pintsuk, T. Loewenhoff, Impact of microstructure on the plasma performance of industrial and high-end tungsten grades, Journal of Nuclear Materials 438 (2013) S945-S948. https://doi.org/10.1016/j.jnucmat.2013.01.205.

[99] N. Hansen, Hall–Petch relation and boundary strengthening, Scripta Materialia 51 (2004) 801–806. https://doi.org/10.1016/j.scriptamat.2004.06.002.

[100] M. Wirtz, S. Bardin, A. Huber, A. Kreter, J. Linke, T.W. Morgan, G. Pintsuk, M. Reinhart, G. Sergienko, I. Steudel, G. de Temmerman, B. Unterberg, Impact of combined hydrogen plasma and transient heat loads on the performance of tungsten as plasma facing material, Nucl. Fusion 55 (2015) 123017. https://doi.org/10.1088/0029-5515/55/12/123017.

[101] M. Wirtz, A. Kreter, J. Linke, T. Loewenhoff, G. Pintsuk, G. Sergienko, I. Steudel, B. Unterberg, E. Wessel, High pulse number thermal shock tests on tungsten with steady state particle background, Phys. Scr. T170 (2017) 14066. https://doi.org/10.1088/1402-4896/aa909e.

[102] M. Wirtz, M. Gago, T. Loewenhoff, G. Pintsuk, Laser and Electron Beam Experiments to Qualify the Thermal Shock Behavior of Tungsten, 2019.

[103] A. Huber, A. Arakcheev, G. Sergienko, I. Steudel, M. Wirtz, A.V. Burdakov, J.W. Coenen, A. Kreter, J. Linke, P. Mertens, V. Philipps, G. Pintsuk, M. Reinhart, U. Samm, A. Shoshin, B. Schweer, B. Unterberg, M. Zlobinski, Investigation of the impact of transient heat loads applied by laser irradiation on ITER-grade tungsten, Phys. Scr. T159 (2014) 14005. https://doi.org/10.1088/0031-8949/2014/T159/014005.

[104] M. Wirtz, I. Uytdenhouwen, V. Barabash, F. Escourbiac, T. Hirai, J. Linke, T. Loewenhoff, S. Panayotis, G. Pintsuk, Material properties and their influence on the behaviour of tungsten as plasma facing material, Nucl. Fusion 57 (2017) 66018. https://doi.org/10.1088/1741-4326/aa6938.

[105] I. Steudel, Verhalten von Wandmaterialien unter thermischer und Plasmabelastung, 2017.

[106] M. Wirtz, J. Linke, T. Loewenhoff, G. Pintsuk, I. Uytdenhouwen, Thermal shock tests to qualify different tungsten grades as plasma facing material, Phys. Scr. T167 (2016) 14015. https://doi.org/10.1088/0031-8949/T167/1/014015.

[107] J.W. Coenen, G. Arnoux, B. Bazylev, G.F. Matthews, A. Autricque, I. Balboa, M. Clever, R. Dejarnac, I. Coffey, Y. Corre, S. Devaux, L. Frassinetti, E. Gauthier, J. Horacek, S. Jachmich, M. Komm, M. Knaup, K. Krieger, S. Marsen, A. Meigs, P. Mertens, R.A. Pitts, T. Puetterich, M. Rack, M. Stamp, G. Sergienko, P. Tamain, V. Thompson, ELM-induced transient tungsten melting in the JET divertor, Nucl. Fusion 55 (2015) 23010. https://doi.org/10.1088/0029-5515/55/2/023010.

[108] T.W. Loewenhoff, Combined steady state and high cycle transient heat load simulation with the electron beam facility JUDITH 2. Zugl.: Aachen, Techn. Hochsch., Diss., 2012, Forschungszentrum, Jülich, 2013.

[109] T.E. Evans, ELM mitigation techniques, Journal of Nuclear Materials 438 (2013) S11-S18. https://doi.org/10.1016/j.jnucmat.2013.01.283.

[110] L.R. Baylor, P.T. Lang, S.L. Allen, S.K. Combs, N. Commaux, T.E. Evans, M.E. Fenstermacher, G. Huijsmans, T.C. Jernigan, C.J. Lasnier, A.W. Leonard, A. Loarte, R. Maingi, S. Maruyama, S.J. Meitner, R.A. Moyer, T.H. Osborne, ELM mitigation with pellet ELM triggering and implications for PFCs and plasma performance in ITER, Journal of Nuclear Materials 463 (2015) 104–108. https://doi.org/10.1016/j.jnucmat.2014.09.070.

[111] P. Lang, G. Conway, T. Eich, L. Fattorini, O. Gruber, S. Günter, L. Horton, S. Kalvin, A. Kallenbach, M. Kaufmann, G. Kocsis, A. Lorenz, M. Manso, M. Maraschek, V. Mertens, J. Neuhauser, I. Nunes, W. Schneider, W. Suttrop, H. Urano, t.A.U. Team, ELM pace making and mitigation by pellet injection in ASDEX Upgrade, Nucl. Fusion 44 (2004) 665–677. https://doi.org/10.1088/0029-5515/44/5/010.

[112] L.R. Baylor, S.K. Combs, C.R. Foust, T.C. Jernigan, S.J. Meitner, P.B. Parks, J.B. Caughman, D.T. Fehling, S. Maruyama, A.L. Qualls, D.A. Rasmussen, C.E. Thomas, Pellet fuelling, ELM pacing and disruption mitigation technology development for ITER, Nucl. Fusion 49 (2009) 85013. https://doi.org/10.1088/0029-5515/49/8/085013.

[113] T. Abrams, E.A. Unterberg, D.L. Rudakov, A.W. Leonard, O. Schmitz, D. Shiraki, L.R. Baylor, P.C. Stangeby, D.M. Thomas, H.Q. Wang, Impact of ELM control techniques on tungsten sputtering in the DIII-D divertor and extrapolations to ITER, Physics of Plasmas 26 (2019) 62504. https://doi.org/10.1063/1.5089895.

[114] S.V. Malykhin, I.E. Garkusha, V.A. Makhlai, S.V. Surovitskiy, S.S. Herashchenko, O.I. Girka, Mechanisms of crack generation in high-pure tungsten exposed to high power density plasma, Nuclear Instruments and Methods in Physics Research Section B: Beam Interactions with Materials and Atoms 481 (2020) 6–11. https://doi.org/10.1016/j.nimb.2020.08.013.

[115] X. Zhang, Q. Yan, S. Lang, M. Xia, C. Ge, Texture evolution and basic thermal–mechanical properties of pure tungsten under various rolling reductions, Journal of Nuclear Materials 468 (2016) 339–347. https://doi.org/10.1016/j.jnucmat.2015.04.001.

[116] T. Loewenhoff, S. Antusch, G. Pintsuk, M. Rieth, M. Wirtz, High pulse number thermal shock testing of tungsten alloys produced by powder injection molding, Nuclear Materials and Energy 20 (2019) 100680. https://doi.org/10.1016/j.nme.2019.100680.

[117] T.W. Morgan, M. Balden, T. Schwarz-Selinger, Y. Li, T.H. Loewenhoff, M. Wirtz, S. Brezinsek, G. de Temmerman, ITER monoblock performance under lifetime loading conditions in Magnum-PSI, Phys. Scr. T171 (2020) 14065. https://doi.org/10.1088/1402-4896/ab66df.

[118] R.N. Stuart, M.W. Guinan, R.J. Borg, A computer simulation of the effect of temperature on the threshold atomic displacement energy in tungsten metal, Radiation Effects 30 (1976) 129–133. https://doi.org/10.1080/00337577608233054.

[119] J.H. Yu, M.J. Baldwin, R.P. Doerner, T. Dittmar, A. Hakola, T. Höschen, J. Likonen, D. Nishijima, H.H. Toudeshki, Transient heating effects on tungsten, Journal of Nuclear Materials 463 (2015) 299–302. https://doi.org/10.1016/j.jnucmat.2014.10.035.

[120] S. Kajita, N. Yoshida, R. Yoshihara, N. Ohno, M. Yamagiwa, TEM observation of the growth process of helium nanobubbles on tungsten, Journal of Nuclear Materials 418 (2011) 152–158. https://doi.org/10.1016/j.jnucmat.2011.06.026.

[121] V.K. Alimov, W.M. Shu, J. Roth, K. Sugiyama, S. Lindig, M. Balden, K. Isobe, T. Yamanishi, Surface morphology and deuterium retention in tungsten exposed to low-energy, high flux pure and helium-seeded deuterium plasmas, Phys. Scr. T138 (2009) 14048. https://doi.org/10.1088/0031-8949/2009/T138/014048.

[122] R.P. Doerner, M.J. Baldwin, T.C. Lynch, J.H. Yu, Retention in tungsten resulting from extremely high fluence plasma exposure, Nuclear Materials and Energy 9 (2016) 89–92. https://doi.org/10.1016/j.nme.2016.04.008.

[123] E.J. Mittemeijer, Fundamentals of Materials Science: The Microstructure-Property Relationship Using Metals as Model Systems, Springer-Verlag Berlin Heidelberg, Berlin, Heidelberg, 2011.

[124] M. Wirtz, J. Linke, G. Pintsuk, J. Rapp, G.M. Wright, Influence of high flux hydrogen-plasma exposure on the thermal shock induced crack formation in tungsten, Journal of Nuclear Materials 420 (2012) 218–221. https://doi.org/10.1016/j.jnucmat.2011.09.035.

[125] G.-H. Lu, H.-B. Zhou, C.S. Becquart, A review of modelling and simulation of hydrogen behaviour in tungsten at different scales, Nucl. Fusion 54 (2014) 86001. https://doi.org/10.1088/0029-5515/54/8/086001.

[126] Berger, Matthias Jörg, Untersuchung heliuminduzierter Nanostrukturen in Wolfram unter transient thermischen Belastungen.

[127] A. Eksaeva, D. Borodin, J. Romazanov, A. Kirschner, A. Kreter, M. Eichler, M. Rasinski, A. Pospieszczyk, B. Unterberg, S. Brezinsek, C. Linsmeier, D. Tskhakaya, I. Borodkina, M. Komm, Surface roughness effect on Mo physical sputtering and re-deposition in the linear plasma device PSI-2 predicted by ERO2.0, Nuclear Materials and Energy 19 (2019) 13–18. https://doi.org/10.1016/j.nme.2019.02.006.

[128] A. Eksaeva, D. Borodin, J. Romazanov, A. Kreter, A. Pospieszczyk, S. Dickheuer, S. Möller, B. Göths, M. Rasinski, U. Knoche, A. Terra, A. Kirschner, I. Borodkina, M. Eichler, B. Unterberg, S. Brezinsek, C. Linsmeier, E. Vassallo, M. Pedroni, M. Passoni, D. Dellasega, M. Sala, F. Romeo, S. Henderson, M. O'Mullane, H. Summers, D. Tskhakaya, K. Schmid, ERO2.0 modelling of the effects of surface roughness on molybdenum erosion and redeposition in the PSI-2 linear plasma device, Phys. Scr. T171 (2020) 14057. https://doi.org/10.1088/1402-4896/ab5810.

[129] T.J. Petty, M.J. Baldwin, M.I. Hasan, R.P. Doerner, J.W. Bradley, Tungsten 'fuzz' growth re-examined: the dependence on ion fluence in non-erosive and erosive helium plasma, Nucl. Fusion 55 (2015) 93033. https://doi.org/10.1088/0029-5515/55/9/093033.

[130] S. Kajita, S. Kawaguchi, N. Ohno, N. Yoshida, Enhanced growth of large-scale nanostructures with metallic ion precipitation in helium plasmas, Scientific reports 8 (2018) 56. https://doi.org/10.1038/s41598-017-18476-7.

[131] D. Nishijima, Y. Kikuchi, M. Nakatsuka, M.J. Baldwin, R.P. Doerner, M. Nagata, Y. Ueda, Effects of Steady-State Plasma Exposure on Tungsten Surface Cracking due to Elm-Like Pulsed Plasma Bombardment, Fusion Science and Technology 60 (2011) 1447–1450. https://doi.org/10.13182/FST11-A12703.

[132] T. Loewenhoff, J. Linke, G. Pintsuk, R.A. Pitts, B. Riccardi, ITER-W monoblocks under high pulse number transient heat loads at high temperature, Journal of Nuclear Materials 463 (2015) 202–205. https://doi.org/10.1016/j.jnucmat.2014.11.002.

[133] M. Farahani, I. Sattari-Far, Effects of residual stresses on crack-tip constraints, Scientia Iranica 18 (2011) 1267–1276. https://doi.org/10.1016/j.scient.2011.11.024.

[134] N.S. Rossini, M. Dassisti, K.Y. Benyounis, A.G. Olabi, Methods of measuring residual stresses in components, Materials & Design 35 (2012) 572–588. https://doi.org/10.1016/j.matdes.2011.08.022.

[135] G.E. Totten, M.A.H. Howes, T. Inoue, Handbook of residual stress and deformation of steel, ASM International, Materials Park, OH, 2002.

[136] S. Pathak, D. Stojakovic, R. Doherty, S.R. Kalidindi, Importance of surface preparation on the nano-indentation stress-strain curves measured in metals, J. Mater. Res. 24 (2009) 1142–1155. https://doi.org/10.1557/jmr.2009.0137.

[137] W. Jiang, X. Cheng, H. Cai, T. Ali, J. Zhang, The response of yttrium aluminum garnet (YAG) grains and grain boundaries to nanoindentation, J Mater Sci 53 (2018) 16198–16206. https://doi.org/10.1007/s10853-018-2782-6.

[138] D.-K. Kim, S. Lee, W. Hyung Baek, Microstructural study of adiabatic shear bands formed by high-speed impact in a tungsten heavy alloy penetrator, Materials Science and Engineering: A 249 (1998) 197–205. https://doi.org/10.1016/S0921-5093(98)00565-6.

[139] J. Gibson, D. Armstrong, S. Roberts, The micro-mechanical properties of ion irradiated tungsten, Phys. Scr. T159 (2014) 14056. https://doi.org/10.1088/0031-8949/2014/T159/014056.

[140] Z. Zhang, E. Hasenhuetl, K. Yabuuchi, A. Kimura, Evaluation of helium effect on ion-irradiation hardening in pure tungsten by nano-indentation method, Nuclear Materials and Energy 9 (2016) 539–546. https://doi.org/10.1016/j.nme.2016.06.010.

[141] F. Kong, M. Qu, S. Yan, A. Zhang, S. Peng, J. Xue, Y. Wang, Helium-induced hardening effect in polycrystalline tungsten, Nuclear Instruments and Methods in Physics Research Section B: Beam Interactions with Materials and Atoms 406 (2017) 643–647. https://doi.org/10.1016/j.nimb.2017.02.029.

[142] L. Tanure, A. Bakaeva, A. Dubinko, D. Terentyev, K. Verbeken, Effect of annealing on microstructure, texture and hardness of ITER-specification tungsten analyzed by EBSD, vickers micro-hardness and nano-indentation techniques, Journal of Nuclear Materials 524 (2019) 191–199. https://doi.org/10.1016/j.jnucmat.2019.07.005.

[143] C.S. Corr, S. O'Ryan, C. Tanner, M. Thompson, J.E. Bradby, G. de Temmerman, R.G. Elliman, P. Kluth, D. Riley, Mechanical properties of tungsten following rhenium ion and helium plasma exposure, Nuclear Materials and Energy 12 (2017) 1336–1341. https://doi.org/10.1016/j.nme.2017.04.012.

[144] W.Q. Chen, X.Y. Wang, X.Z. Xiao, S.L. Qu, Y.Z. Jia, W. Cui, X.Z. Cao, B. Xu, W. Liu, Characterization of dose dependent mechanical properties in helium implanted tungsten, Journal of Nuclear Materials 509 (2018) 260–266. https://doi.org/10.1016/j.jnucmat.2018.07.004.

[145] S. Huang, G. Ran, P. Lei, N. Chen, S. Wu, N. Li, Q. Shen, Effect of crystal orientation on hardness of He + ion irradiated tungsten, Nuclear Instruments and Methods in Physics Research Section B: Beam Interactions with Materials and Atoms 406 (2017) 585–590. https://doi.org/10.1016/j.nimb.2017.04.063.

[146] E. Hasenhuetl, Z. Zhang, K. Yabuuchi, P. Song, A. Kimura, Crystal orientation dependence of ion-irradiation hardening in pure tungsten, Nuclear Instruments and Methods in Physics Research Section B: Beam Interactions with Materials and Atoms 397 (2017) 11–14. https://doi.org/10.1016/j.nimb.2017.02.030.

[147] S. Krat, M. Mayer, A. Baron-Wiechec, S. Brezinsek, P. Coad, Y. Gasparyan, K. Heinola, I. Jepu, J. Likonen, P. Petersson, C. Ruset, G. de Saint-Aubin, A. Widdowson, J.E. contributors, Comparison of erosion and deposition in JET divertor during the first three ITER-like wall campaigns, Phys. Scr. T171 (2020) 14059. https://doi.org/10.1088/1402-4896/ab5c11.

[148] J.W. Coenen, Y. Mao, J. Almanstötter, A. Calvo, S. Sistla, H. Gietl, B. Jasper, J. Riesch, M. Rieth, G. Pintsuk, F. Klein, A. Litnovsky, A.V. Mueller, T. Wegener, J.-H. You, C. Broeckmann, C. Garcia-Rosales, R. Neu, C. Linsmeier, Advanced materials for a damage resilient divertor concept for DEMO, Fusion Engineering and Design. https://doi.org/10.1016/j.fusengdes.2016.12.006.

[149] J.W. Coenen, Fusion Materials Development at Forschungszentrum Jülich, Adv. Eng. Mater. https://doi.org/10.1002/adem.201901376.

[150] F. Klein, T. Wegener, A. Litnovsky, M. Rasinski, X.Y. Tan, J. Gonzalez-Julian, J. Schmitz, M. Bram, J.W. Coenen, C. Linsmeier, Oxidation resistance of bulk plasma-facing tungsten alloys, Nuclear Materials and Energy 15 (2018) 226–231. https://doi.org/10.1016/j.nme.2018.05.003.

[151] A. Litnovsky, T. Wegener, F. Klein, C. Linsmeier, M. Rasinski, A. Kreter, X. Tan, J. Schmitz, Y. Mao, J.W. Coenen, M. Bram, J. Gonzalez-Julian, Advanced smart tungsten alloys for a future fusion power plant, Plasma Phys. Control. Fusion 59 (2017) 64003. https://doi.org/10.1088/1361-6587/aa6948.

[152] T.W. Morgan, P. Rindt, G.G. van Eden, V. Kvon, M.A. Jaworksi, N.J.L. Cardozo, Liquid metals as a divertor plasma-facing material explored using the Pilot-PSI and Magnum-PSI linear devices, Plasma Phys. Control. Fusion 60 (2018) 14025. https://doi.org/10.1088/1361-6587/aa86cd.

[153] R. Neu, H. Maier, M. Balden, S. Elgeti, H. Gietl, H. Greuner, A. Herrmann, A. Houben, V. Rohde, B. Sieglin, I. Zammuto, Investigations on tungsten heavy alloys for use as plasma facing material, Fusion Engineering and Design. https://doi.org/10.1016/j.fusengdes.2017.01.043.

[154] R.E. Nygren, F.L. Tabarés, Liquid surfaces for fusion plasma facing components—A critical review. Part I, Nuclear Materials and Energy 9 (2016) 6–21. https://doi.org/10.1016/j.nme.2016.08.008.

[155] J.H. You, E. Visca, C. Bachmann, T. Barrett, F. Crescenzi, M. Fursdon, H. Greuner, D. Guilhem, P. Languille, M. Li, S. McIntosh, A.V. Müller, J. Reiser, M. Richou, M. Rieth, European DEMO divertor target, Nuclear Materials and Energy 9 (2016) 171–176. https://doi.org/10.1016/j.nme.2016.02.005.

[156] J. Reiser, L. Garrison, H. Greuner, J. Hoffmann, T. Weingärtner, U. Jäntsch, M. Klimenkov, P. Franke, S. Bonk, C. Bonnekoh, S. Sickinger, S. Baumgärtner, D. Bolich, M. Hoffmann, R. Ziegler, J. Konrad, J. Hohe, A. Hoffmann, T. Mrotzek, M. Seiss, M. Rieth, A. Möslang, Ductilisation of tungsten (W), International Journal of Refractory Metals and Hard Materials 69 (2017) 66–109. https://doi.org/10.1016/j.ijrmhm.2017.07.013.

[157] J. Reiser, M. Rieth, A. Möslang, B. Dafferner, A. Hoffmann, X. Yi, D. Armstrong, Tungsten foil laminate for structural divertor applications – Tensile test properties of tungsten foil, Journal of Nuclear Materials 434 (2013) 357–366. https://doi.org/10.1016/j.jnucmat.2012.12.003.

[158] C. Linsmeier, M. Rieth, J. Aktaa, T. Chikada, A. Hoffmann, J. Hoffmann, A. Houben, H. Kurishita, X. Jin, M. Li, A. Litnovsky, S. Matsuo, A. von Müller, V. Nikolic, T. Palacios, R. Pippan, D. Qu, J. Reiser, J. Riesch, T. Shikama, R. Stieglitz, T. Weber, S. Wurster, J.-H. You, Z. Zhou, Development of advanced high heat flux and plasma-facing materials, Nucl. Fusion 57 (2017) 92007. https://doi.org/10.1088/1741-4326/aa6f71.

Acknowledgements

I would like to express my sincere gratitude to my doctoral supervisor Prof. Dr. Manja Krüger for giving me the opportunity of completing my doctoral thesis at the Institut für Energie und Klimaforschung (IEK-2 and IEK-4) of the Forschungszentrum Jülich.

Furthermore, I would like to express my thanks to Prof. Dr. Bernhard Unterberg for his willingness to take over the responsibility as co-referee and for the friendly conversations and advice.

I would also like to give many thanks to my scientific supervisor Dr. Marius Wirtz for his guidance, encouragement and patience throughout the process of my doctoral studies. His support was vital for the fulfillment of my work and his humor, particular taste in music and the plenty friendly conversations made this journey even more interesting.

My special thanks go to Dr. Thorsten Loewenhoff and Daniel Dorow-Gerspach for their advice and support as well as the many stimulating discussions. I thank also Dr. Benjamin Spilker, Dr. Juan Du and (soon Dr.) Litong Yang for their friendship and all the delightful and thought-provoking conversations we had during all these years.

Huge thanks go to the PSI-2 crew, Dr. Arkadi Kreter, Michael Vogel and Sebastian Kraus. My work would have proven impossible without their support.

For their immense help with the metallography and post-mortem analysis of my samples I would like to thank the team at IEK-2, Dr. E. Wessel, V. Gutzeit, J. Bartsch, D. Grüner, D. Esser and M. Ziegner.

I also thank everyone at IEK-2 and IEK-4 for the friendly atmosphere that made my days at the FZJ so pleasant. I thank in particular everyone in the FC MIEKRO 02 for all the good moments we had and for our second place trophy, and Dr. Timur Galiullin for all the Döner we ate together after work.

Special thanks go to Daniela, without whom I would not have been able to achieve half of what I have achieved. I also want to thank all the friends that have cheered, supported and accompanied me through this journey, in particular Sam, Armaghan, Philipp, Irene, Pascha and Helena, the friendship we share will never be forgotten. I thank Los Ilegales, Xavier, Dina, Benedikt and Lukas. A huge thanks goes to Lisa, who always knows how to brighten my days and has shown me to always look on the bright side of life. And last, but not least, I give my immense gratitude to my family, my parents, my brothers, aunts, cousins and of course my grandparents, Tito, Tita, Abo y Aba. This work is dedicated to Dr. Elías Jiménez Fonseca, Abo, who inspired me to pursue science and knowledge. I miss you dearly.

Band / Volume 599
IEK-14 Report 2022
Research contributions for the energy transition and structural change in the Rhineland
B. Emonts (Ed.) (2022), 83 pp
ISBN: 978-3-95806-676-2

Band / Volume 600
Development of Glass-based Sealants for the Joining of Oxygen Transport Membranes
X. Li (2022), IV, 159 pp
ISBN: 978-3-95806-677-9

Band / Volume 601
High-resolution imaging of transport processes
with GPR full-waveform inversion
P. Haruzi (2022), iv, 173 pp
ISBN: 978-3-95806-678-6

Band / Volume 602
Synthesis of optimized cathode materials
for all-solid-state lithium batteries
C. Roitzheim (2022), xv, 221 pp
ISBN: 978-3-95806-679-3

Band / Volume 603
Development of components based on Ti_2AlC/fiber composites
for aggressive environmental conditions
S. Badie (2023), x, 161 pp
ISBN: 978-3-95806-680-9

Band / Volume 604
Multiregionales Energiesystemmodell mit Fokus auf Infrastrukturen
T. M. Groß (2023), xx, 235 pp
ISBN: 978-3-95806-681-6

Band / Volume 605
Temporal Aggregation Methods for Energy System Modeling
M. A. C. Hoffmann (2023), XXVI, 341 pp
ISBN: 978-3-95806-683-0

Band / Volume 606
Examining transport in the Upper Troposphere –
Lower Stratosphere with the infrared limb imager GLORIA
L. Krasauskas (2023), v, 107 pp
ISBN: 978-3-95806-691-5

Band / Volume 607
Sustainable Fabrication of Ceramic Solid Electrolytes for Solid-State Lithium Batteries
R. Ye (2023), vi, 119 pp
ISBN: 978-3-95806-694-6

Band / Volume 608
Improving Nitrogen Retention in Soils Treated with Pig and Cattle Slurry Through the Use of Organic Soil Amendments
X. Cao (2023), XVI, 119 pp
ISBN: 978-3-95806-696-0

Band / Volume 609
Mechanisches Verhalten von Polymer-Elektrolyt-Membran-Elektrolysezellen und -Stacks
S. Holtwerth (2023), x, 251 pp
ISBN: 978-3-95806-697-7

Band / Volume 610
Membrane Reactor Concepts for Power-to-Fuel Processes
H. Huang (2023), VI, 197 pp
ISBN: 978-3-95806-703-5

Band / Volume 611
Deployment of Fuel Cell Vehicles in Road Transport and the Expansion of the Hydrogen Refueling Station Network: 2023 Update
R. C. Samsun, M. Rex (2023), i, 39 pp
ISBN: 978-3-95806-704-2

Band / Volume 612
Behavior/performance of tungsten as a wall material for fusion reactors
M. Gago (2023), X, 120 pp
ISBN: 978-3-95806-707-3

Weitere ***Schriften des Verlags im Forschungszentrum Jülich*** unter
http://wwwzb1.fz-juelich.de/verlagextern1/index.asp

Energie & Umwelt / Energy & Environment
Band / Volume 612
ISBN 978-3-95806-707-3

Mitglied der Helmholtz-Gemeinschaft

JÜLICH
Forschungszentrum